$\mathbf{k} \cdot \mathbf{p}$ theory for wurtzite InGaN quantum dot arrays with application to ratchet band solar cells

Luc-Eugène Robichaud

Thesis submitted to the University of Ottawa
in partial fulfillment of the requirements for the
degree of Doctor of Philosophy in Physics

Department of Physics
Faculty of Science
University of Ottawa

Abstract

This thesis presents advancements on the modeling of quantum dots using Fourier-space $\mathbf{k} \cdot \mathbf{p}$ theory and on the use of InGaN quantum dots for ratchet band solar cells. Fourier-space based methods have generally assumed sharp material interfaces for electronic structure, strain and piezoelectric potential calculations in quantum dot systems. Additionally, standard Fourier-space methods have often assumed uniform elastic and dielectric constants for the strain and piezoelectric potential calculations. We present generalized methods to include smoothly varying alloy profiles for the quantum dots, including spatially varying elastic and dielectric constants for the strain and piezoelectric potential calculations. For the case of InGaN/GaN quantum dots, we show that the elastic and dielectric constants corrections are important for accurate strain, piezoelectric potentials, and electronic structure. The smooth alloy profiles are constructed by convolving sharp alloy profiles with a Gaussian, and we show that the electronic structure strongly depends on the smoothing kernel, indicating the need for precise alloy profiles for accurate electronic structures. We also present a new method that facilitates the coupling of strain into the $\mathbf{k} \cdot \mathbf{p}$ Hamiltonian when considering isolated dots, greatly reducing the computational costs of calculating the Hamiltonian matrix elements. Using the methods, we investigate the use of InGaN/GaN quantum dot superlattices as ratchet band solar cells, where we propose to use the piezoelectric potential to generate a ratchet. The piezoelectric potential can spatially separate confined electron and hole states, creating a spatial ratchet in order to reduce recombination. From our quantum dot $\mathbf{k} \cdot \mathbf{p}$ model, we calculate optical light absorption cross sections and present an improved method to calculate bound-to-continuum absorption, where electrons are excited out of the dots. In this method, we approximate the continuum states as bulk $\mathbf{k} \cdot \mathbf{p}$ states for GaN. By coupling our $\mathbf{k} \cdot \mathbf{p}$ model absorptions into a detailed balance model, we predict power conversion efficiencies. We find that a large number of QD layers is necessary to achieve sufficiently strong absorption as to reach high efficiencies, highlighting one of the key issues of QD-based solar cells. We consider systems which consists of up to 131000 layers of quantum dots and an ideal Lambertian back reflector with two different QD geometries. The first geometry possesses a strong spatial ratchet and can reach a maximum efficiency of 36% under a 1-sun 6000 K black-body spectrum. We verify the existence of the spatial ratchet through the optical properties of the system, showing that it truly has the potential to block recombination. We also present an efficiency optimized system that reaches a 42% detailed balance efficiency but does not have a spatial ratchet.

Acknowledgments

First and foremost, I thank my advisor Jacob J. Krich for his guidance throughout this endeavor. You have been the most incredible and helpful advisor any student could have hoped for. Second, I thank my partner, Victoria Hatfield, and both our families for their support and love throughout the years. Thanks also go to my colleagues and friends, with special thanks to Eduard Dumitrescu, Peter Rose, Daisy Xia, Kyle Robertson and Ludmila Szulakowska.

Dedication

To my parents, I will never forget the love and support you have given me throughout all these years.

Publications

1. L. Robichaud and J.J. Krich, "*InGaN Quantum Dots for Intermediate Band Solar Cells*", 2019 IEEE 46th Photovoltaic Specialists Conference (PVSC), 2019, pp. 2138-2142

2. L. Robichaud and J.J. Krich, "*Wurtzite InGaN/GaN Quantum Dots for Intermediate Band Solar Cells*", 2019 International Conference on Numerical Simulation of Optoelectronic Devices (NUSOD), 2019, pp. 57-58

3. Cheriton, R., Sadaf, S.M., Robichaud, L., Krich, J.J., Mi, Z., Hinzer, K., "*Two-photon photocurrent in InGaN/GaN nanowire intermediate band solar cells*", Commun Mater 1, 63 (2020).

4. L. Robichaud and J.J. Krich , "*Efficient Fourier space quantum dot* $\mathbf{k}\cdot\mathbf{p}$ *for wurtzite systems including smooth alloy profile and spatially varying elastic and dielectric constants*", Journal of Applied Physics 129, 224301 (2021)

5. L. Robichaud and J.J. Krich, "*InGaN quantum dot superlattices as ratchet band solar cells*", 2021 IEEE 48th Photovoltaic Specialists Conference (PVSC), 2021, pp. 1626-1630

6. L. Robichaud and J.J. Krich , "*InGaN quantum dot superlattices as ratchet band solar cells*", IEEE Journal of Photovoltaics 12, 474, (2022)

Statement of Original Contributions

In the thesis, Chapters 1, 2, 3 and 4 present standard and well known theories that form the base for the author's contributions, which are contained in Chapters 6 and 7.

Chapter 6 was published in the Journal of Applied Physics with authors Luc Robichaud and Jacob J. Krich. The project was begun in collaboration with Jacob J. Krich and I performed all analytical and numerical calculations. This work presents new Fourier-space based methods of calculating strain, piezoelectric potential and single-particle electronic structures of quantum dots with spatially varying compositions. A novel method of generating a smooth alloy profile is presented and we show that elastic and dielectric constants that vary according to the profile are important for accurate modeling. Additionally, we also present a new approach of efficiently including strain within Fourier-space based $\mathbf{k} \cdot \mathbf{p}$ models, which can be numerically challenging. Jacob J. Krich provided guidance and edited the manuscript.

Chapter 7 is now published in the Journal of Photovoltaics with authors Luc Robichaud and Jacob J. Krich. The project was begun in collaboration with Jacob J. Krich and I performed all analytical and numerical calculations. In this work, we provide improved methods of calculating bound-to-free absorption in quantum dots by approximating the conduction-band continuum states of the quantum dot as bulk GaN states. Using my QD model, which is presented in Chapter 6, we show that InGaN quantum dots can possess a spatial ratchet that is produced by the piezoelectric potential. We show that by operating as a ratchet band solar cell, this system can reach efficiencies well above the Shockley-Queisser limit and we provide the necessary quantum dot parameters such as size and composition to achieve this. Jacob J. Krich provided guidance and edited the manuscript.

Not contained in this thesis is a paper published in Communications Materials with authors Ross Cheriton, Sharif M. Sadaf, Luc Robichaud, Jacob J. Krich, Zetian Mi and Karin Hinzer [1]. My contributions consisted of the quantum dot modeling found in the simulations section of the supplementary.

Contents

Chapter 1

Introduction: Intermediate and ratchet band solar cells

1.1 The Shockley-Queisser limit

Solar cells are typically semiconductor-based photovoltaic devices that are designed to absorb sunlight to produce electricity as efficiently as possible. There exist many solar cell architectures, with the simplest, oldest, and most common being the single junction solar cell (SJSC). The SJSC consists of a pn-junction, which is a semiconductor that is n-type doped on one side and p-type on the other, with metallic contacts at each end to complete the circuit. As shown in Fig. 1.1, the band structure of an ideal semiconductor consists of a valence band (VB), a conduction band (CB) and a bandgap E_{CV} separating the two bands. The general goal is to now expose the solar cell to light in order to excite electrons from the VB to CB. By applying a voltage at the contacts, we can extract the electrons in the CB to produce current, which in turn produces power. For terrestrial applications, the incident light spectrum is emitted by the sun and filtered by the earth's atmosphere. The standard spectrum used to characterize solar cell performance on earth is called the Air Mass 1.5 spectrum or simply AM1.5 [2]. However, it is sometimes practical to approximate the incoming spectrum as a simple black-body spectrum, which can be easily described analytically. In either case, the incoming spectrum is broadband.

Prior to shining light or applying an external bias, the system is at equilibrium such that the electron populations in the VB and CB can be described by Fermi-Dirac statistics, along with a single Fermi level μ. Once we add light or a bias, that is no longer the case, as the VB and CB electron populations will be displaced from their equilibrium. However, given a sufficiently long time after turning on the light or bias, the system can reach a steady state. If the light is sufficiently intense such that the electrons are excited and recombine faster than the electron population can establish an equilibrium by electron-electron interactions, then we can no longer use Fermi-Dirac distributions

to describe these populations. However, for the case of solar applications, the incident light and applied bias are sufficiently weak that each electron population can reach a quasi-equilibrium, meaning the populations can be described with Fermi-Dirac distributions, but with each population having its own quasi-Fermi level. We denote the quasi-Fermi level for the CB as μ_{c} and μ_{v} for the VB, as shown in Fig. 1.1.

As mentioned, to operate as a solar cell, the general goal is to excite electrons into the CB by absorbing light and then extract them at the contacts to produce current I. The power produced is then simply $P = IV$, where P is the power and V the voltage between the contacts. Current generation is directly related to the number of photons being absorbed, since each absorbed photon produces at least a single electron and hole pair that can be extracted as current. Voltage, on the other hand, is related to the quasi-Fermi level splitting μ_{CV}, which is shown in Fig. 1.1, as it represents the useful amount of energy we can extract from an electron by closing the circuit. An ideal semiconductor can only absorb photons whose energy is above or equal the threshold energy E_{CV}, where energies larger than E_{CV} leave the electron in an excited CB state. However, this excited electron quickly gives off its excess energy to the lattice, thermalizing down to the CB band edge. This mechanism is known as thermalization losses and essentially heats up the solar cell. Once relaxed to the CB band edge, electrons can recombine either radiatively or nonradiatively. There are two key nonradiative processes, with the first being Shockley-Read-Hall recombination, which is trap assisted recombination, with trap states being due to impurities or defects. This type of recombination can be suppressed in high quality materials, where the density of trap states is low. The second type is Auger recombination, where the electron in the CB recombines with a hole by giving its energy to either an electron already in the CB or a hole in the VB. Auger recombination therefore relies on electron-electron interactions and so depends on the electron density. Radiative recombination can generally not be suppressed, since a good absorber is also a good emitter by reciprocity. Although, radiative recombination leaves the chance for a possible re-absorption, which is known as photon recycling.

We may be interested to find the ideal SJSC material. By making a set of ideal assumptions, which are carefully specified in Section 2.1, we can find what bandgap produces the highest efficiency. In the case of a small bandgap, the SJSC absorbs a lot of light, which increases current production, but also suffers from large thermalization losses, reducing the voltage. By the same mechanisms, a larger bandgap allows for larger voltage, but reduces current. In an ideal system, the optimal bandgap therefore balances out these two effects, along with radiative recombination. Shockley and Queisser showed that this idealized SJSC has a maximum attainable efficiency of 31% under a 1-sun black-body spectrum. This 31%, which no real SJSC can surpass, is known as the Shockley-Queisser limit (SQL). Experimental work on the SJSC has led to amazing progress with the current record efficiency for a crystalline silicon SJSC being 26.7% under a 1-sun AM1.5G spectrum [3]. Knowing we can only expect to squeeze out a few additional percentage points of efficiency motivates us to look at entirely different architectures whose maximum efficiency is higher than the SQL.

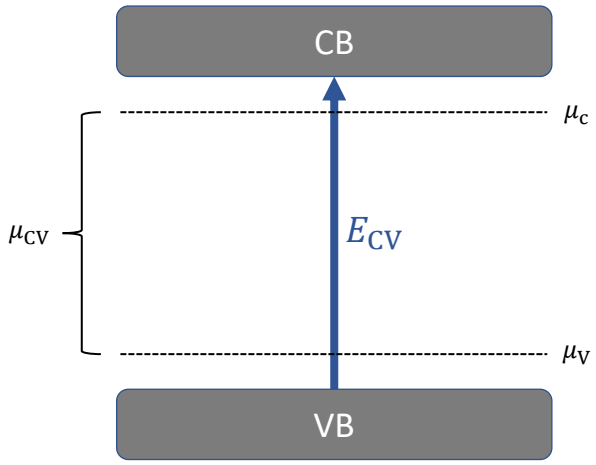

Figure 1.1: Energy diagram for a single junction device, which is characterized by a single gap. Arrow indicates full gap transition with energy threshold E_{cv}. Black dashed lines are the quasi-Fermi levels for each respective electron population and μ_{CV} the quasi-Fermi level splitting.

1.2 Intermediate band solar cell

Multiple architectures, which introduce new mechanisms to increase either current or voltage, have been proposed in order to surpass the SQL. Among them is the multijunction (or tandem) solar cell, which consists of multiple series-connected junctions, with each having a different bandgap. By ordering the junctions such that the largest bandgaps absorb first and the smallest last, we can greatly reduce thermalization losses. This architecture has had great success, with efficiencies currently reaching up to 47.1% under a AM1.5D spectrum with a concentration factor of 143 suns [4]. Another example is the intermediate band solar cell (IBSC), which seeks to increase the efficiency by introducing an intermediate band (IB) inside the bandgap, as shown in Fig. 1.2. This IB introduces a second pathway for current generation by allowing the electrons to reach the CB via a two-step absorption process. The first step is an excitation from the VB to the IB and the second step from the IB to the CB, where it can be extracted as current. This IB pathway therefore requires two photons to produce a single electron and hole pair, while the CV process only requires a single photon. Similar to the CV process, the IV absorption process has the threshold energy E_{IV} and E_{CI} for the CI. Compared to the SJSC, IBSCs can have a large bandgap, allowing for a large voltage, while being able to maintain a high current by absorbing a portion of the photons with $E < E_{CV}$, which is not possible for the SJSC. Reference [5] was the first to show, under the same ideal conditions as for the SQL, that the IBSCs' limiting efficiency is 63% under a fully concentrated black-body spectrum. For comparison, the SJCSs' limiting efficiency is 41% under a fully concentrated black-body spectrum, indicating that IBSCs truly have the potential to surpass the SJSC. However, IBSCs have not achieved this yet due to poor light absorption, recombination, or both.

An important material candidate for IBSCs has been semiconductor quantum dots (QDs), which are small amounts of crystalline material contained in a larger host crystalline material, where the dot and host typically

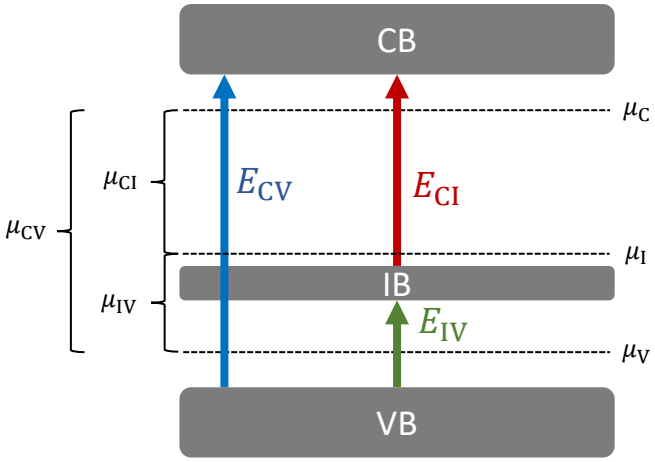

Figure 1.2: Energy diagram for the intermediate band solar cell. Colored arrows show the three key processes for absorption and emission. Black dashed lines are the quasi-Fermi levels for each respective electron population. μ_{ij} are the quasi-Fermi level splittings for each pair of bands.

have the same crystal structure. In this thesis, we focus on wurtzite $In_xGa_{1-x}N$ QDs contained inside of bulk wurtzite GaN. For shortness, we will simply write InGaN from now on, while understanding that there is an implied indium fraction x. Since the dot and host materials differ, so do their band structure, leading to misaligned band edges at the material interfaces. Depending on dot and host material combinations, these band offsets can be found in different configurations, as shown in Fig. 1.3. Panel (a) uses the case of InGaN/GaN as an example of a type-I QD, where the dot material has the smaller bandgap and is entirely contained inside the bandgap of the host. The z axis is a spatial sweep through the system with the solid black lines being the bulk CB and VB edge energies. In the QD region, the bandgap is smaller, leading to a confinement potential inside of which one finds discrete electronic states, shown as blue dashed lines. The geometry of the confining potential is determined by the dot geometry, while its depth is determined by the alloying fraction. This dependence then implies that the density of states, and the electronic gap between the lowest QD confined electron and hole states, is also determined by the dot size and composition. Panel (b) uses GaSb/GaAs QDs as an example of type-II QDs, where the bulk band edges are both shifted up in energy with respect to the host. Similar to the type-I case, the VB offset in type-II QDs also contains discrete states, whose properties can be tuned by changing the dot size and composition. Absorption for the IV process is generally weaker in type-II systems since initial and final wavefunctions only overlap near the dot boundary, as shown by the green arrow in Fig. 1.3(b). Both type-I [6, 7] and type-II [8, 9] QDs have been investigated as candidates for IBSCs, but we will focus on InGaN/GaN QDs, which are type-I.

For solar applications, the idea is to use the QD bound states to absorb low energy photons that are not absorbed by the host material. If the electrons in the QD CB states are able to achieve their own quasi-equilibrium, meaning that they are decoupled from electron populations in the VB and CB, then we describe them by Fermi-Dirac statistics and their own quasi-Fermi level. Assuming this quasi-equilibrium to be the case, then we can label the QD bound states in the CB act as an IB, as highlighted by the gray rectangle in Fig. 1.3(a). For the VB offset,

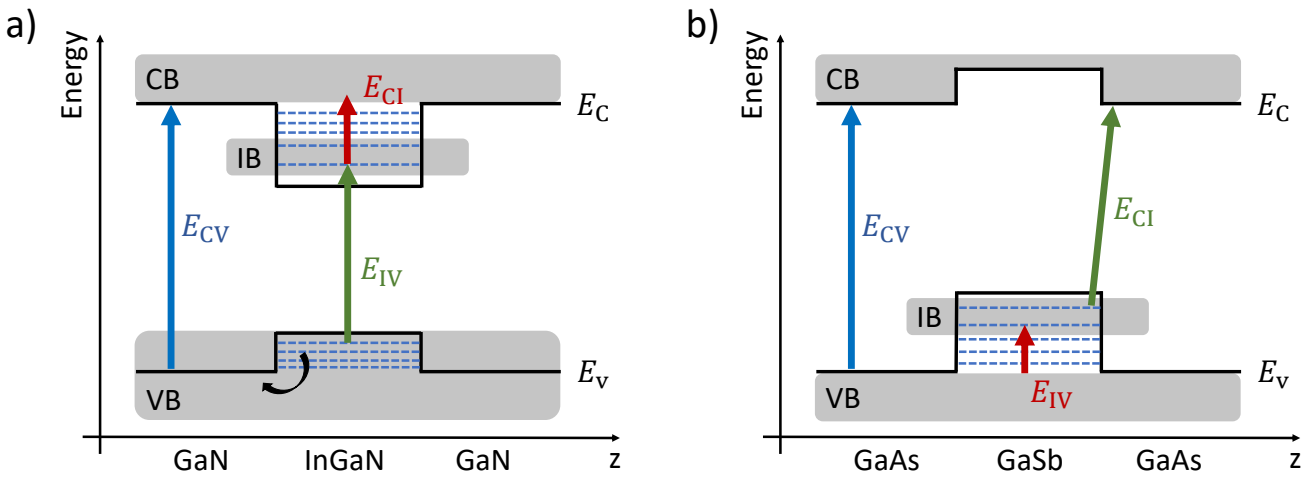

Figure 1.3: Electronic structure diagrams for a (a) Type-I and (b) type-II QD system along a spatial axis for the case without strain or piezoelectric potential. Black lines are E_c and E_v, the bulk VB and CB edges, and dashed blues lines the energy levels of QD confined states. Grey rectangles highlight the three key bands, where the QD states are considered to act as an IB. Colored arrows show the three key processes for absorption and emission, which are taken equivalent to those in Fig. 1.2. Black curved arrow in panel (a) represents hole escape via either thermal energy or low energy photons. The two subgap transition energy thresholds do not generally add up to the full gap, whereas they do so for the IBSC.

it is assumed that holes can escape thermally or via lower energy photons, which is represented by a black arrow in the same figure. Having the holes thermally escape implies that the electron population in the VB QD confined states must share a quasi-Fermi level with those of the host material's VB. Analogous to the IBSC, we can now identify three bands in the QD system and two current producing pathways. The first pathway is the CV process where an electron is excited from the VB to the CB inside the host material. The second pathway is a two-step absorption process inside the QD, with the first step being the IV absorption process and CI the second, which gets the electron into the CB of the host material, from where it can be extracted as current. Similar to the IBSC, the three absorption processes are characterized by their respective threshold energy, however the QD system is such that $E_{IV} + E_{CI} < E_{CV}$, while the IBSC is constrained to $E_{IV} + E_{CI} = E_{CV}$.

Although the two-step process has been demonstrated to work in principle [1, 10, 11], devices remain poorly efficient. A first issue is that QDs have a small absorption cross section, requiring many QDs and/or light trapping to be optically thick. Experimentally, having too many layers of QDs inside a device can lead to complications such as strain-induced defects, which is discussed further below. The other causes for low efficiencies are IV recombination and CI trapping. If carriers in the QD CB states have a short lifetime compared to the rate of the CI absorption process, then electrons will significantly recombine from the QD CB states to the QD VB states. Electron trapping is when electrons from the host material's CB relaxes into the bound states of the QD. For light emitting applications such as light emitting diodes, electron trapping is a good thing since the goal is to have injected current populate the QD CB states, leading to radiative recombination. In the case of IBSCs, a high trapping rate means that the electron population from CB and IB (QD CB states) are not decoupled and so must share a quasi-Fermi level. This

shared quasi-Fermi level leads to a lower μ_c and so a decreased μ_{CV}, hurting the voltage. Additionally, trapping reduces the number of electrons collected at the contacts, reducing the current. The trapping problem can be solved by surrounding the dot with an additional semiconductor, called a shell, whose band structure is such that a potential barrier forms to prevent electrons from falling into the potential well [12]. However, having a shell does not solve the internal recombination problem for the IV process.

1.3 Ratchet band solar cell overview

The ratchet band solar cell (RBSC), which is shown in Fig. 1.4(a), was originally proposed in [13] with the goal of solving the internal recombination problem. The RBSC takes the IBSC and introduces an additional band inside the gap, which is called the ratchet band (RB). The RB is such that it is thermally connected to the IB, meaning that its electron population shares a quasi-Fermi level with the electrons occupying the IB. Additionally, electrons occupying the RB are forbidden to transition to the VB, thus blocking recombination. We assume that the IB to RB relaxation is sufficiently fast as to empty the IB and allow us to ignore any transition between the IB and CB, i.e., there is no CI process. Similar to the IBSC, we therefore identify three absorption processes, which are the CV, IV, and CR, which are characterized by absorption threshold energies E_{CV}, E_{IV}, and E_{CR}, respectively. We also identify two current generating pathways for the electrons, with the first being the standard CV process which appears in the SJSC and IBSC. The second pathway starts with an excitation from the VB to the IB, where the electron then quickly relaxes into the RB. Once in the ratchet band, recombination to the VB is blocked, giving the electron an extended lifetime. From the RB, the electron can absorb a photon to complete the CR process and be extracted as current.

The decoupling of the RB and VB is key for blocking recombination, and there have been multiple candidates for RBSCs such as quantum-cascade-style AlGaAs/GaAs quantum well superlattice [14], InAs QDs contained in AlGaAs/GaAs heterojunctions [15] and erbium-doped GaAs [16]. However, none of these systems are able to function at room temperature with the required broadband absorptions that are necessary for solar applications. InGaN QDs have already been found in many applications such as light emitting diodes [17], single-photon emitters [18], water splitting [19] and solar cells [1, 7]. In Chapter 7, we investigate the use of wurtzite InGaN/GaN QD superlattices for RBSCs. In the original proposal from [13], the threshold energies for the three absorption processes are such that $E_{IV}+E_{CR} \geq E_{CV}$, whereas a QD system generally has $E_{IV}+E_{CR} < E_{CV}$, as also seen in Fig. 1.3. Figure 1.4(b) shows a QD-adapted RBSC system which includes a band offset, allowing for $E_{IV} + E_{CR} < E_{CV}$. Wurtzite systems have non-centrosymmetric interfaces that causes formation of permanent dipoles when under strain, leading to the formation of a piezoelectric field. We propose using electron and hole states, which are spatially separated by the piezoelectric field, as a spatial ratchet.

Let us now talk about how QD systems are generally made, experimentally. Molecular beam epitaxy (MBE),

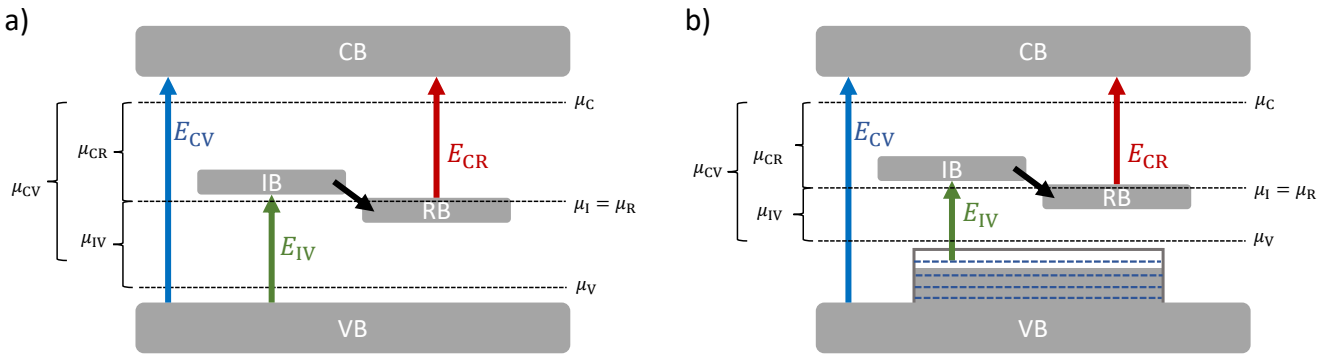

Figure 1.4: Energy diagram for (a) the originally proposed RBSC and (b) a QD-based RBSC. Colored arrows show the three key transitions for absorption and emission. Black arrow represents non-radiative recombination from the IB to the RB. Blue dashed lines represent QD states. IB and RB are also made from QD states. Black dashed lines are the quasi-Fermi levels for each respective band.

chemical vapor deposition (CVD) and metalorganic chemical vapor deposition (MOCVD) are all standard approaches used for making semiconductor quantum dots. In these methods, a substrate is placed inside a vacuum chamber and various gasses are introduced. The nature of the gas depends on which technique is used (MBE, CVD or MOCVD) and which materials are to be grown. By controlling pressure, temperature, and gas flow rates, one can grow semiconductors epitaxially on the substrate. QD systems can have different architectures, but a first example is QDs which are contained inside of layers, which are typically made using the Stranski-Krastanov growth mode. In this growth mode, one first starts with initial layer of host material (e.g. GaN) on a substrate and then slowly grows a thin layer, called a wetting layer, of what is to be the dot material (e.g. InGaN). Due to lattice mismatch between the two materials, strain builds up in the wetting layer as it gets thicker. Eventually, due to strain, it is energetically favorable for islands to form, leading to the formation of QDs. However, the QD nucleation process is random, leading to an ensemble of randomly positioned dots. Once the quantum dots are formed, more GaN is grown on top of the dots act as a barrier layer, isolating the QDs from subsequent QD layers [7, 20–22]. The process can be repeated to obtain multiple layers of QDs, but strain can build up in the system with each layer, which can lead to defects in the device. However, it is possible to periodically grow a layer of some material whose lattice constants is such that it counteracts the strain build up. This is called a strain compensating layer and allows for the growth of a larger number of QD layers. Our second QD architecture example consists of QDs contained in nanowires, which can be grown with [23, 24] or without a catalyst [17, 19]. Using a catalyst means depositing metallic nanoparticles on the substrate to seed the growth of nanowires. During the nanowire growth, the gas being introduced into the growth chamber can be exchanged with other gas, allowing for the formation of QDs along the length of the nanowires. The process can be repeated, allowing for the growth of multiple quantum dots along the nanowire. Given the nanowire is not radially constrained by any material, strain can naturally relax at the surface in these systems. In general, regardless of the method or architecture, QDs do not have sharp alloying profiles, but are rather smoothly varying. Given that QDs are so sensitive to their size and composition, it is important to

properly capture these smooth alloy profiles in their modeling.

The properties of QDs can vary greatly based on their size and composition. Electronic structure modeling can therefore be a useful tool to guide the optimization of QDs for target applications. However, one needs to include all important physics if one is to have an accurate model. Lattice-mismatch driven or external strain leads to a deformed lattice, which can significantly impact the electronic structure. Additionally, materials such as III-nitrides are also piezoelectric, meaning that these lattice deformations lead to internal polarizations, also affecting the electronic structure. Quite often, models used to calculate strain, piezoelectric fields and electronic structure assume sharp material interfaces, neglecting the smooth alloy profiles of actual QDs.

In this thesis, we present standard Fourier-space based techniques used to model strain, piezoelectric potentials, and electronic structure of wurtzite QDs. These methods originally assumed sharp material interfaces, uniform elastic constants for strain and uniform dielectric constants for piezoelectric potential calculations. We present methods to include spatially varying alloy profiles with elastic, and dielectric constants that vary accordingly, and show that these effects are important for accurate modeling of wurtzite InGaN QDs. We then use our model to explore the use of wurtzite InGaN/GaN QD superlattices as RBSCs. We show that the piezoelectric potential in InGaN QDs could be used as a spatial ratchet, blocking internal recombination. By coupling our electronic structure model with detailed balance calculations, we predict limiting efficiencies of 36% for an example system, which has a spatial ratchet, and 42% for an optimized system without the ratchet.

1.4 Thesis outline

In this thesis, chapters 2, 3, 4 and 5 are reviews of well established theories for detailed balance, electronic structure, strain and piezoelectric potential calculations. Chapters 6 and 7 contain the original contributions of the author to these fields.

In Chapter 2, we use detailed balance calculations to calculate maximum attainable efficiencies of SJSCs, IBSCs and RBSCs. These calculations motivate the exploration of the RBSC system and the use of InGaN QDs as a candidate for making RBSCs.

Chapter 3 presents the $\mathbf{k}\cdot\mathbf{p}$ method, which is used to calculate band structure, for bulk wurtzite materials. More precisely, we present the construction of a time-reversal invariant 8-band $\mathbf{k}\cdot\mathbf{p}$ model. Chapter 4 uses the theory of slowly varying envelope functions to write a $\mathbf{k}\cdot\mathbf{p}$ model for quantum dots superlattices. Following the electronic structure calculation, we present a method for modeling absorption within the QD superlattices by using Fermi's golden rule. Chapter 5 focuses on methods to calculate strain and piezoelectric potential for a QD superlattice, while assuming sharp material interfaces, and uniform elastic and dielectric constants.

Chapter 6 begins the author's contributions to the field and generalizes the methods of Chapters 4, and 5 for $\mathbf{k}\cdot\mathbf{p}$ electronic structure, strain, and piezoelectric potential calculations to include smooth alloy profiles along with

spatially varying elastic and dielectric constants. We also present a new approach of efficiently coupling strain into the $\mathbf{k} \cdot \mathbf{p}$ Hamiltonian. Chapter 7 uses the methodology of Chapter 6 to investigate the use of InGaN/GaN QD superlattices as RBSCs. Using absorptances calculated from the $\mathbf{k} \cdot \mathbf{p}$ model and detailed balance calculations, we study the potential efficiencies attainable in such a system. We show that the spatially separated states due to the piezoelectric potential in InGaN quantum dots could be used as a spatial ratchet to reduce internal recombination.

Chapter 2

Detailed balance calculations

The ultimate goal of solar cells is to convert sunlight into useful electrical power as efficiently as possible. Taking the incoming solar radiation from a $T_{\mathsf{s}} = 6000$ K black-body and with an ambient temperature $T_{\mathsf{a}} = 300$ K , the Carnot efficiency limit is $\left(T_{\mathsf{s}} + T_{\mathsf{a}}\right)/T_{\mathsf{s}} = 95\%$. However, even in idealized photovoltaics, there are many loss mechanisms, such as radiative recombination, that contribute to reducing the maximum attainable efficiency of a particular photovoltaic architecture below this 95%. Solar cells come in many different architectures (e.g. SJSC and IBSC) and it is useful to know an architecture's maximum attainable efficiency. In the case of mature technologies, it can indicate how much additional efficiency you could possibly gain by further optimizations. For newer technologies, it can indicate if a system is worth investing work in by comparing its limiting efficiencies to those of existing technologies.

The goal is to make a simple description of a system (SJSC, IBSC and RBSC) and see what thermodynamics say about the attainable efficiency from such a system. Let us start by considering the ideal SJSC such that

1. Absorption is perfect, meaning that $a\left(E\right) = 1$ for $E > E_{\mathsf{CV}}$, where $a\left(E\right)$ is the absorptance,
2. Each absorbed photon produces a single electron and hole pair,
3. There is only radiative recombination, which is called the radiative limit,
4. Materials have perfect conductance, i.e. infinite carrier mobilities,
5. Contacts are selective, meaning only electrons are extracted on one side and only holes on the other,
6. Contacts are ohmic, meaning there is no loss of energy at the contacts,
7. All excited electrons are thermalized instantaneously.

Under these assumptions, Shockley and Queisser showed that the maximum attainable efficiency is 31% under a 1-sun black-body spectrum [25], which is far below the Carnot limit. Real semiconductor photovoltaics with only

one bandgap cannot surpass this 31%, but are approaching it. The same methods have also been applied to IBSCs and RBSCs to determine their limiting efficiencies [5, 13, 15, 26]. In this chapter, we establish detailed balance calculations under assumptions (1-7) and calculate the maximum efficiencies of the SJSC, IBSC and RBSC. In Chapter 7, we investigate InGaN QDs superlattices as ratchet band solar cells and extend the detailed balance theory presented here to include realistic absorptances, which are obtained from electronic structure calculations.

2.1 Single junction solar cell

We start by studying the case of a single junction solar cell (SJSC), as shown in Fig. 1.1. Here, the goal is to calculate the maximum attainable efficiency under the ideal assumptions (1-7). The solar cell absorbs light from both the sun and the ambient, but also emits its own light as well. By ambient, we mean other sources of light that are simply part of the environment and simply not from the sun. The sun and ambient are considered at equilibrium ($\Delta\mu$=0) and can naturally be treated as black bodies that emit according to Planck's law. The solar cell, on the other hand, is not at equilibrium, but emits light based on its electron and hole populations, which depends on their respective quasi-Fermi levels. The solar cell's emitted photon flux can be described using a modified Planck spectrum [27]

$$\phi(\mu,T)=\frac{2\pi}{h^3c^2}\int_0^\infty \frac{a\left(E\right)E^2\mathsf{d}E}{\mathsf{e}^{(E-\mu)/kT}-1}, \qquad \left[m^{-2}s^{-1}\right] \tag{2.1}$$

where E is energy, $a\left(E\right)$ the absorptance, μ is the quasi-Fermi level splitting between the two carrier populations taking part in the emission, k the Boltzmann's constant, h the Planck constant, C the speed of light and T temperature of the emitting or absorbing body. As discussed in Chap. 1, the SJSC is characterized as having a single bandgap E_{CV}, only absorbing or emitting photons at energies larger or equal to E_{CV}. Given assumption (1), which is absorption of a photon is guaranteed if its energy is greater than the bandgap, Eq. 2.1 can be written

$$\phi(\mu,T)=\frac{2\pi}{h^3c^2}\int_{E_{\mathsf{CV}}}^\infty \frac{E^2\mathsf{d}E}{\mathsf{e}^{(E-\mu)/kT}-1}. \tag{2.2}$$

If there was no recombination whatsoever, then all photons from the sun and ambient, with $E > E_{\mathsf{CV}}$, would be absorbed. In this case, there would be no carrier loss mechanisms and the extracted current could be directly obtained from the absorbed photon fluxes. However, the cell must also emit photons, reducing the number of extracted electrons by exactly the number of emitted photons, giving the relation

$$\frac{J}{q}=\phi_{\mathsf{abs}}-\phi_{\mathsf{emit}}, \tag{2.3}$$

where J is the current density, q the charge, ϕ_{abs} the photon flux absorbed from the sun and ambient, and ϕ_{emit} the photon flux emitted by the cell. If there was also nonradiative recombination, which does not produce photons,

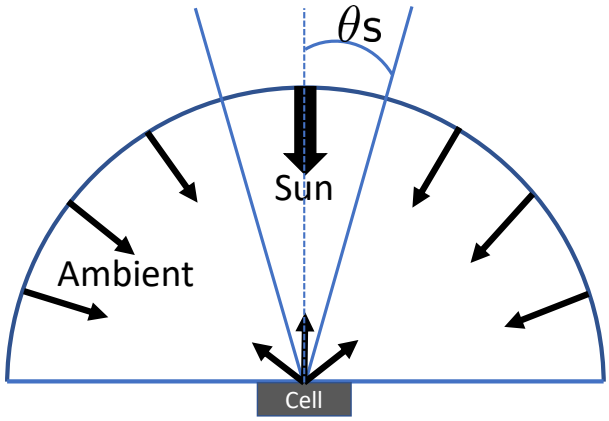

Figure 2.1: Partitioning of the hemisphere in terms of light emitted by the sun and the ambient. Light is absorbed from the sun within the angle θ_s and ambient within the rest of the hemisphere. The solar cell emits in all directions of the hemisphere. Figure adapted from [2].

then the number of extracted electrons could not be directly deduced from photon flux being absorbed and emitted. It is therefore through assumption (3) that we can calculate the current through the simple photon bookkeeping of Eq. 2.3. Using Eq. 2.2, we can write Eq. 2.3 as [2]

$$J = q\left[Cf_s\phi(0,T_s) + (1-Cf_s)\,\phi(0,T_a) - \phi(\mu_{CV},T_a)\right]. \tag{2.4}$$

Here, C is the concentration factor such that $C = 1$ corresponds to 1 sun and $C = 1/f_s$ to full concentration, where $f_s = \sin^2\theta_s = 2.16\times10^{-5}$ and θ_s is the half-angle occupied by the sun, as seen from the solar cell, as shown in Fig. 2.1[2]. In writing Eq. 2.4, we have assumed light from the sun is contained within the angle θ_s and contributions from the ambient from the rest of the hemisphere. The first and second terms on the right-hand side of Eq. 2.4 are the photons fluxes emitted from the sun and ambient, respectively. The last term is the flux emitted from the cell. Assumption (4) is perfect conductance, which means the quasi-Fermi levels are uniform throughout the device. By assumption (5) and (6), the contacts at each end of the device are also considered ideal, meaning there is no voltage drop or barrier at the interfaces. Under these assumptions, the useful energy obtained from extracting an electron-hole pair by closing the circuit is the energy separation between the quasi-Fermi levels, implying $\mu_{CV} = qV$, where V is the voltage between the contacts. For a given V and J, the power density produced by the cell is

$$P = VJ \tag{2.5}$$

The system's power conversion efficiency is defined as

$$\eta = \frac{\mathcal{P}_{out}\left(V_{mpp}\right)}{\mathcal{P}_{in}} \tag{2.6}$$

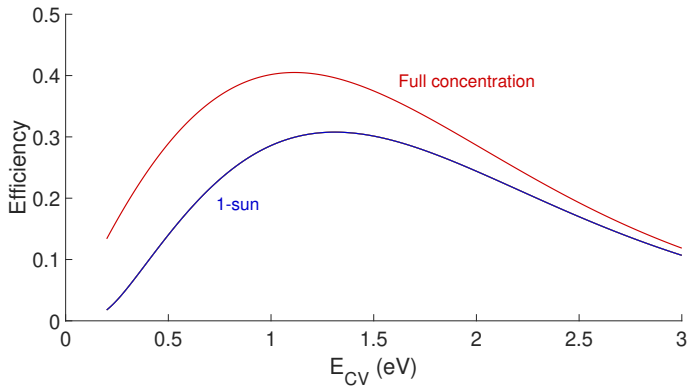

Figure 2.2: Single junction voltage-optimized efficiency for varying bandgaps under a 1-sun and fully concentrated 6000 K black-body spectrum.

where $\mathcal{P}_{\text{in}}$ is the total power incident on the cell and $\mathcal{P}_{\text{out}}$ is the total electrical power produced by the cell. V_{mpp} is the voltage at the maximum power point (MPP), which is defined as

$$\left.\frac{d\mathcal{P}_{\text{out}}}{dV}\right|_{V=V_{\text{mpp}}} = 0. \tag{2.7}$$

For a given solar cell with surface area A, the efficiency can be written

$$\begin{aligned}\eta &= \frac{\mathcal{P}_{\text{out}}\left(V_{\text{mpp}}\right)}{\mathcal{P}_{\text{in}}} \\ &= \frac{P\left(V_{\text{mpp}}\right)A}{P_{\text{in}}A} \\ &= \frac{V_{\text{mpp}}J}{P_{\text{in}}}\end{aligned} \tag{2.8}$$

The denominator in Eq. 2.8 can be calculated using the Stefan Boltzmann law to obtain [2, 5]

$$\eta = \frac{V_{\text{mpp}}J}{Cf_{\text{s}}\sigma T_{\text{s}}^4}, \tag{2.9}$$

where σ is the Stefan-Boltzmann constant.

In terms of efficiency, there is a current and voltage trade-off when varying the bandgap. Reducing the bandgap allows for the absorption of more photons, increasing J, but reduces V_{mpp}, which can't surpass the bandgap. Increasing the bandgap allows higher V_{mpp}, but reduces the number of photons that can be absorbed by the gap, which is known as transparency losses, resulting in a reduced J. Figure 2.2 shows the efficiency versus the bandgap, where we find a maximal efficiency of 31% at $E_{\text{CV}} = 1.3$ eV for a 1-sun concentration and 41% at $E_{\text{CV}} = 1.1$ eV for full concentration. These maximum efficiencies are known as Shockley-Queisser limits (SQLs) and often serve as benchmarks to estimate another system's potential.

2.2 Intermediate band solar cell

We are now interested in systems whose efficiency can surpass the SQL. To do so, at least the current or voltage must be increased over the single-junction optima, which is possible with the IBSC, as discussed in Chapter 1. Let us then consider the IBSC, as shown in Fig. 1.2, with the assumptions (1-7). Additionally, we assume that no current is extracted from the IB, which would couple the quasi-Fermi levels of the three bands. Coupling the quasi-Fermi levels would reduce μ_{CV} and so reduce the voltage between the contacts.

Let's now proceed in a similar fashion as was done for the SJSC and calculate the efficiency of an ideal IBSC. Unlike for the SJSC, the IBSC has three absorption processes (CV, IV and CI) that can compete for photons. Overlapping absorptions by considering a finite thickness has been investigated by [2] and [28], but we only consider perfect non-overlapping absorptions of the form

$$a\left(E, E_{\mathsf{min}}, E_{\mathsf{max}}\right) = \begin{cases} 1 & \text{if } E_{\mathsf{min}} < E < E_{\mathsf{max}} \\ 0 & \text{otherwise} \end{cases}, \tag{2.10}$$

which simplifies calculations. Absorption of the solar spectrum is then partitioned into each of the three absorption processes, as shown in Fig. 2.3, where we have assumed $E_{\mathsf{IV}} < E_{\mathsf{CI}}$. This partitioning scheme minimizes thermalization losses by giving each photon to the process that maximizes use of the photon's energy. From Eq. 2.1, the absorbed or emitted photon fluxes for a process can then be written

$$\phi(E_{\mathsf{min}}, E_{\mathsf{max}}, \mu, T) = \frac{2\pi}{h^3c^2} \int_{E_{\mathsf{min}}}^{E_{\mathsf{max}}} \frac{E^2 \mathsf{d}E}{\mathsf{e}^{(E-\mu)/kT} - 1}. \tag{2.11}$$

In the IBSC, both the CV and CI processes contribute to producing electrons in the CB, meaning there are two terms to the current generation. Through the same photon bookkeeping used for the SJSC, the extracted current density is [5]

$$J = q\left[\dot{N}_{\mathsf{CV}} + \dot{N}_{\mathsf{CI}}\right], \tag{2.12}$$

where

$$\begin{aligned} \dot{N}_{\mathsf{CV}} &= C f_{\mathsf{s}} \phi\left(E_{\mathsf{CV}}, \infty, T_{\mathsf{S}}, 0\right) + \left(1 - C f_{\mathsf{s}}\right) \phi\left(E_{\mathsf{CV}}, \infty, T_{\mathsf{a}}, 0\right) - \phi\left(E_{\mathsf{CV}}, \infty, T_{\mathsf{a}}, \mu_{\mathsf{CV}}\right) \\ \dot{N}_{\mathsf{CI}} &= C f_{\mathsf{s}} \phi\left(E_{\mathsf{CI}}, E_{\mathsf{CV}}, T_{\mathsf{S}}, 0\right) + \left(1 - C f_{\mathsf{s}}\right) \phi\left(E_{\mathsf{CI}}, E_{\mathsf{CV}}, T_{\mathsf{a}}, 0\right) - \phi\left(E_{\mathsf{CI}}, E_{\mathsf{CV}}, T_{\mathsf{a}}, \mu_{\mathsf{CI}}\right) \\ \dot{N}_{\mathsf{IV}} &= C f_{\mathsf{s}} \phi\left(E_{\mathsf{IV}}, E_{\mathsf{CI}}, T_{\mathsf{S}}, 0\right) + \left(1 - C f_{\mathsf{s}}\right) \phi\left(E_{\mathsf{IV}}, E_{\mathsf{CI}}, T_{\mathsf{a}}, 0\right) - \phi\left(E_{\mathsf{IV}}, E_{\mathsf{CI}}, T_{\mathsf{a}}, \mu_{\mathsf{IV}}\right). \end{aligned} \tag{2.13}$$

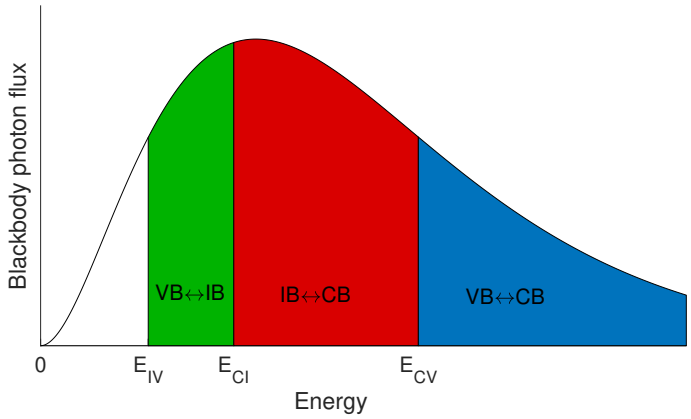

Figure 2.3: Partitioning of the solar spectrum for the three key IBSC processes under the non-overlapping absorption approximation.

Similarly to Eq. 2.12, the current extracted from the IB is

$$J_{\mathsf{IB}} = q\left[\dot{N}_{\mathsf{IV}} - \dot{N}_{\mathsf{CI}}\right]. \tag{2.14}$$

However, we assumed no current is extracted from the IB, leading to the condition

$$\dot{N}_{\mathsf{CI}} = \dot{N}_{\mathsf{IV}}. \tag{2.15}$$

Power and efficiency are calculated same as for the SJSC. A similar set of equations can be written for $E_{\mathsf{IV}} > E_{\mathsf{CI}}$, where E_{IV} and E_{CI} are exchanged.

Figure 2.4 shows efficiency for varying subgap threshold energies E_{CV}, and E_{IV} for a 1-sun and full concentration 6000 K black-body spectrum. Note that the IBSC is constrained to have $E_{\mathsf{IV}} + E_{\mathsf{CI}} = E_{\mathsf{CV}}$, removing the need for a third axis in the figure. For a fixed bandgap, the CI process is current limiting for small E_{IV} and the IV process for when E_{IV} is large. The highest efficiency is therefore found when the two subgap processes are current matched, which is near $E_{\mathsf{CV}}/3$ [5, 28]. As already shown in [5, 28], we find a maximum efficiency of 47% for 1-sun and 63% for full concentration, both well above their respective SQL. We refer to these numbers as the limiting efficiencies, but it is possible to surpass them at low light concentration by considering overlapping absorptions [28].

We are interested in using InGaN/GaN QDs as solar cells with the goal to surpass the SQL. Figure 2.5 shows the efficiency for $E_{\mathsf{CV}} = 3.51$ eV, which corresponds to the bandgap of GaN, where we find a limiting efficiency of 40% at 1 sun, which is well above the SQL. Since the bandgap of InGaN has a large range, from 0.78 eV to 3.51 eV, one should be able to tune the electronic gap of InGaN QDs to maximize efficiency. This flexibility in the system's electronic structure indicates that InGaN/GaN QDs are indeed a promising candidate for IBSC's. The loss in efficiency compared to the global maximum is due to the GaN bandgap being too wide, but could also be improved by choosing an InGaN host material.

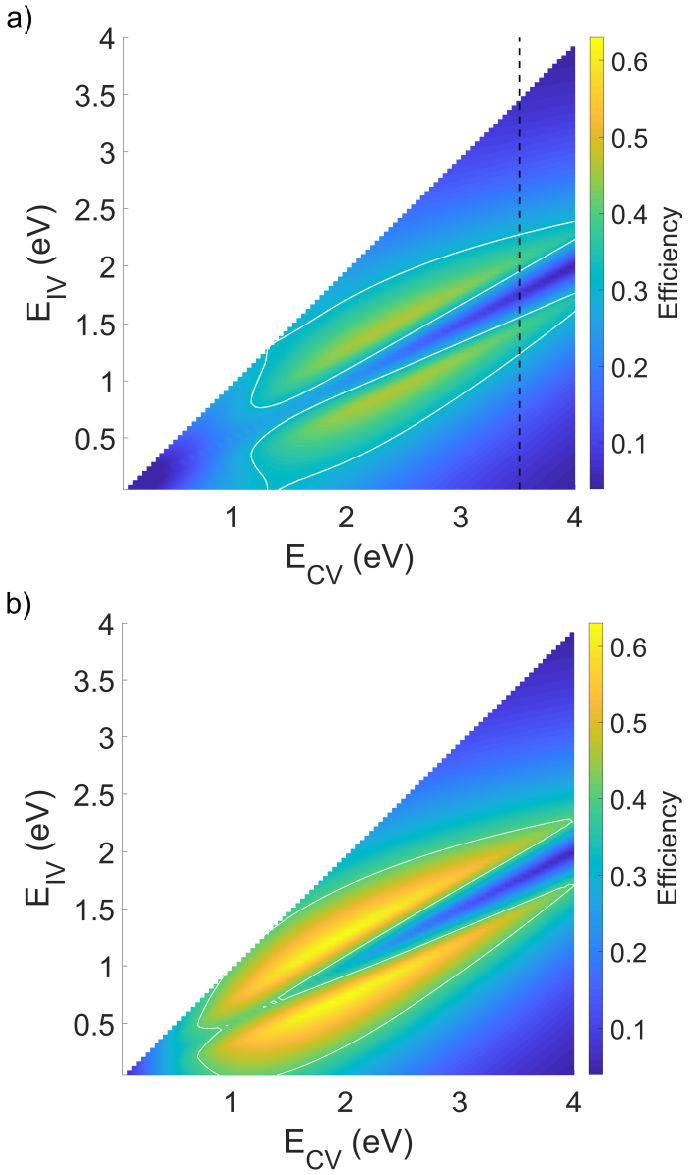

Figure 2.4: IBSC detailed-balance efficiency landscape for (a) 1-sun and (b) full concentration 6000 K black-body spectrum. White contours are the Shockley-Queisser limits for each respective concentration, 31% for 1 sun and 41% for full concentration. Black dashed line in panel (a) corresponds to the results shown in Fig. 2.5.

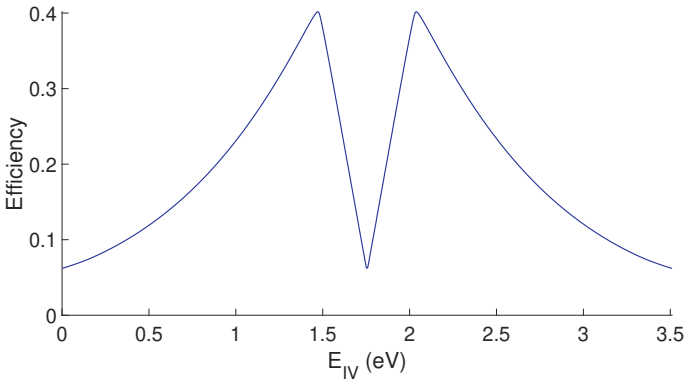

Figure 2.5: IBSC detailed-balance efficiency for $E_{CV} = 3.51$ eV, the case of a GaN host material, at 1-sun concentration. Sweep corresponds to the black dashed line in Fig. 2.4(a).

2.3 Ratchet band solar cell

Let us now turn to the RBSC, which seeks to solve the recombination problem present in IBSCs. Here, we will focus on the original proposal shown in Fig. 1.4(a), while the case of QDs is investigated in Chapter 7. To calculate efficiencies, we once again use the assumptions (1-7), that no current is extracted from the IB or RB, and that the subgap processes are characterized by perfect non-overlapping absorptions, as described in Eq. 2.10. Just as for the IBSC, the RBSC has two current producing pathways and we can once again use photon bookkeeping to obtain the current density, which is

$$J = q\left(\dot{N}_{\mathsf{CV}} + \dot{N}_{\mathsf{CR}}\right), \tag{2.16}$$

where

$$\begin{aligned}
\dot{N}_{\mathsf{CV}} &= Cf_{\mathsf{s}}\phi\left(E_{\mathsf{CV}}, \infty, T_{\mathsf{S}}, 0\right) + \left(1 - Cf_{\mathsf{s}}\right)\phi\left(E_{\mathsf{CV}}, \infty, T_{\mathsf{a}}, 0\right) - \phi\left(E_{\mathsf{CV}}, \infty, T_{\mathsf{a}}, \mu_{\mathsf{CV}}\right) \\
\dot{N}_{\mathsf{CR}} &= Cf_{\mathsf{s}}\phi\left(E_{\mathsf{CR}}, E_{\mathsf{g}}, T_{\mathsf{S}}, 0\right) + \left(1 - Cf_{\mathsf{s}}\right)\phi\left(E_{\mathsf{CR}}, E_{\mathsf{g}}, T_{\mathsf{a}}, 0\right) - \phi\left(E_{\mathsf{CR}}, E_{\mathsf{g}}, T_{\mathsf{a}}, \mu_{\mathsf{CI}}\right) \\
\dot{N}_{\mathsf{IV}} &= Cf_{\mathsf{s}}\phi\left(E_{\mathsf{IV}}, E_{\mathsf{CR}}, T_{\mathsf{S}}, 0\right) + \left(1 - Cf_{\mathsf{s}}\right)\phi\left(E_{\mathsf{IV}}, E_{\mathsf{CR}}, T_{\mathsf{a}}, 0\right) - \phi\left(E_{\mathsf{IV}}, E_{\mathsf{CR}}, T_{\mathsf{a}}, \mu_{\mathsf{IV}}\right).
\end{aligned} \tag{2.17}$$

Here, we have assumed $E_{\mathsf{IV}} < E_{\mathsf{CR}} < E_{\mathsf{CV}}$. Similar equations may also be written for $E_{\mathsf{CR}} < E_{\mathsf{IV}} < E_{\mathsf{CV}}$, in which case E_{IV} and E_{CR} are exchanged in Eq. 2.17. Similarly to the IBSC, the current produced by the IB and RB is

$$J_{\mathsf{IB/RB}} = q\left[\dot{N}_{\mathsf{IV}} - \dot{N}_{\mathsf{CR}}\right], \tag{2.18}$$

but we assumed no current is extracted from the IB or RB, leading to

$$\dot{N}_{\mathsf{IV}} = \dot{N}_{\mathsf{CR}}. \tag{2.19}$$

Contrary to the IBSC, the sum of the two subgap energy thresholds do not have to sum to the full gap,

$$E_{\mathsf{CV}} = E_{\mathsf{IV}} + E_{\mathsf{CI}} - \Delta E. \tag{2.20}$$

Here, ΔE is the energy separation between the IB and RB. This gives an additional degree of freedom, allowing to further optimize the subgap absorptions to better match the solar spectrum compared to the IBSC.

Figure 2.6 shows the efficiency for a fully optimized system (E_{CV}, E_{IV}, E_{CR} and V) with fixed ΔE for various sun concentrations. For the 1-sun concentration, we find a maximum efficiency of 49% and 63% for full concentration. In terms of detailed balance efficiency, introducing a RB is therefore beneficial at low concentrations, but not at full concentration where the IBSC is already optimal. The 1-sun result is interesting because we are able to surpass the IBSC even though we have introduced an energy loss mechanism in coupling the IB and RB. This energy loss is compensated by the additional degree of freedom (ΔE) in choosing the threshold energies compared to the IBSC,

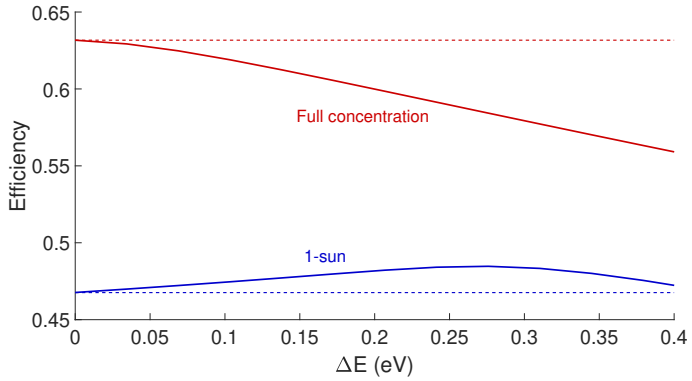

Figure 2.6: RBSC detailed-balance efficiency for varying ratchet energy ΔE, as defined in Eq. 2.20. Subgap energy thresholds have been optimized for each ΔE to obtain the maximal efficiencies.

allowing for more optimal energy thresholds. By better optimizing the energy thresholds, the efficiency is improved by reducing recombination rates and entropy at low light concentrations [13, 26, 29] . The special case of a RBSC with an InGaN host material is presented in Chap. VII.

Both the IBSC and RBSC presented here are idealized systems for theoretical analysis. From an experimental standpoint, it has been difficult to construct a device that can absorb subgap light with high power conversion efficiency. In our case, we are interested in using InGaN QDs for RBSCs. However, the properties of QDs can vary widely in geometry and composition. If a device is to approach these theoretical efficiencies, one must have an accurate model of the QDs' electronic and optical properties in order to optimize the system. In the following sections, we present the $\mathbf{k} \cdot \mathbf{p}$ method to predict electronic structure for bulk systems, which is then extended to QDs.

Chapter 3

$\mathbf{k} \cdot \mathbf{p}$ theory for bulk wurtzite materials

The optical properties of QDs can be tuned by changing their geometry or composition, making them quite attractive for light emitting or photovoltaic applications. The tunablility of a QD's optical properties is due to its electronic structure's sensitivity to the QD's dimensions and composition. Electronic structure modeling then becomes a crucial tool in understanding and tuning a QD so it can achieve high power-conversion efficiencies.

There are many standard methods used to calculate the electronic structure of semiconductor systems, such as tight-binding (TB), $\mathbf{k} \cdot \mathbf{p}$, density functional theory (DFT) and pseudo-potentials. Each of these methods has its advantages and disadvantages. Usually, methods such as DFT and pseudo-potentials are used to obtain the electronic structure in the complete first Brillouin zone, while $\mathbf{k} \cdot \mathbf{p}$ theory is mostly used to obtain the electronic structure in the vicinity of some high symmetry point in $\mathbf{k}$-space. While methods such as TB, DFT and pseudo-potentials are atomistic in nature, the $\mathbf{k} \cdot \mathbf{p}$ method is a macroscopic, continuous and semi-empirical theory. $\mathbf{k} \cdot \mathbf{p}$ theory contains knowledge of crystal structure, but requires input parameters that are typically obtained from fitting the $\mathbf{k} \cdot \mathbf{p}$ model to calculations such as DFT or pseudo-potentials. Our ultimate goal is to model relatively large InGaN QDs, making atomistic approaches considerably more computationally costly compared to $\mathbf{k} \cdot \mathbf{p}$ theory. For this reason, we chose $\mathbf{k} \cdot \mathbf{p}$ theory as our tool for modeling the electronic structure. This chapter covers $\mathbf{k} \cdot \mathbf{p}$ theory for bulk wurtzite systems and is extended to QDs in Chap. 4.

The main idea behind the $\mathbf{k} \cdot \mathbf{p}$ method is to use a finite number of Bloch functions from a high symmetry point in the first Brillouin zone as a basis to approximately construct the band structure in the vicinity of said symmetry point [30, 31]. This is usually done around the $\mathbf{k} = \mathbf{0}$ point in the first Brillouin zone, which is usually labeled the Γ-point and is often where the bandgap is located, as is the case for InGaN materials. For a given material, the number of bands, or Bloch functions, included in the model must be chosen based on the electronic structure at the symmetry point in question and range of desired accuracy within the first Brillouin zone. This implies that one needs knowledge of the electronic structure beforehand. One may then ask, why use $\mathbf{k} \cdot \mathbf{p}$ theory if full knowledge of the band structure is needed beforehand? The $\mathbf{k} \cdot \mathbf{p}$ method is computationally inexpensive and one can easily

model alloys by interpolating known parameters from binary compounds.

In terms of materials, early work was on silicon and germanium [32–34], but has since become a common method for other materials such InGaN [35–40]. 8-band models, which include the CB and three VBs, for spin up and down, are quite common [39–41]. It is also possible to neglect spin-orbit coupling and reduce the system to 4 coupled bands [42, 43]. In some cases, only the valence bands are of interest, leading to a 6-band Hamiltonian [35–38]. Given that the range of accuracy within the first Brillouin zone increases with the number of bands included in the model, 15-band [34], 20-band [44], 24-band [45] and 30-band [46] models have been developed that give accurate results over the full Brillouin zone. However, a larger number of bands also requires a larger number of input parameters. A 10-band model has also been used to describe band anti-crossing in dilute nitride materials [47].

Wurtzite materials are generally characterized as having bandgap at $\mathbf{k} = 0$, which is commonly labeled the Γ-point, within the first brillouin zone. Delimiting the bandgap is a CB and three valence bands, as shown in Fig. 3.1(a). Without the presence of an external magnetic field, these four bands are all doubly degenerate due to time reversal symmetry, which is also known as Kramers' denegeracy. The CB Γ-point Bloch function is s-like in symmetry, while the VB Bloch functions are p-like. By addition of angular momentum and spin, these VB Bloch functions form $J = 3/2$ and $J = 1/2$ states, which are degenerate when ignoring spin orbit coupling and crystal field splitting. Including the spin-orbit coupling splits the $J = 3/2$ and $J = 1/2$ states. Including then the crystal field splitting splits the $J = 3/2$ states, leading to nondegenerate bands, not counting the Kramer's degeneracy. The splitting of the VBs under these effects is shown in Fig. 3.1(b). We now turn to using $\mathbf{k}\cdot\mathbf{p}$ theory to describe the band structure shown in Fig. 3.1(a).

In this chapter, we show how to construct a time-reversal invariant 8-band $\mathbf{k}\cdot\mathbf{p}$ Hamiltonian, which includes crystal field, spin-orbit coupling, and strain, for wurtzite materials. In the first section, we construct a $\mathbf{k}\cdot\mathbf{p}$ model that is first-order in $\mathbf{k}$, while neglecting spin-orbit coupling and strain. We use this toy model in Sec. 3.2 to show that the naively constructed Hamiltonian is not invariant under time-reversal symmetry, while a system without external magnetic fields should be. We correct the Hamiltonian to be time reversal symmetric and show that the toy model does not produce accurate band structures for the valence bands. The proper treatment of time reversal symmetry within $\mathbf{k}\cdot\mathbf{p}$ is well known in literature, with a discussion of how to construct a time-reversal invariant $\mathbf{k}\cdot\mathbf{p}$ Hamiltonian given in [32]. However, we are unaware of any discussion on the reasons as to why a naive construction of the Hamiltonian does not lead to a time-reversal invariant system, which we give in Sect. 3.2.2. The accuracy of the model is then improved in Sec. 3.3 by including effects from additional bands, crystal field, spin-orbit coupling and strain.

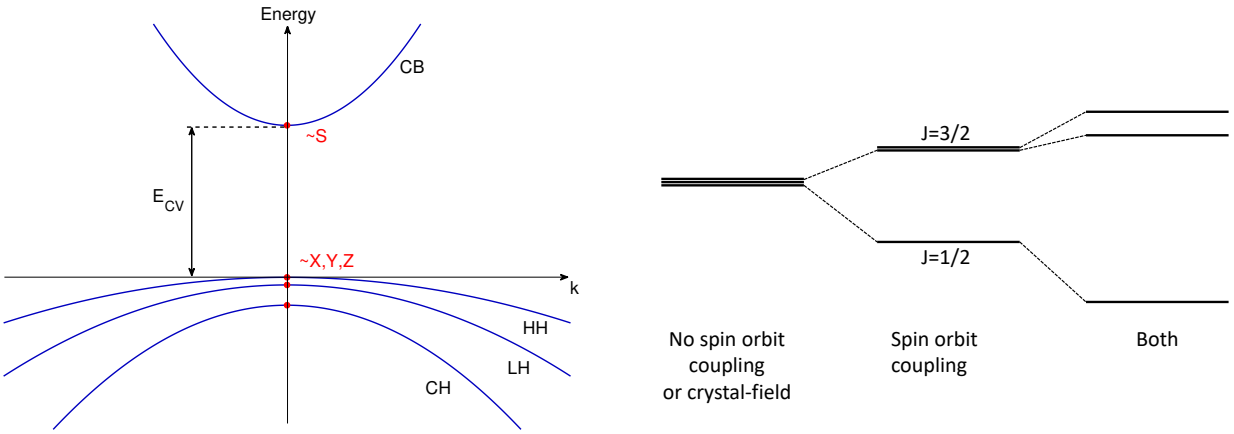

(a) (b)

Figure 3.1: (a) Band structure of wurtzite materials in the neighborhood of the Γ-point, where the bandgap is found. There are four important bands near the bandgap, which are the conduction band (CB), heavy hole (HH), light hole (LH) and crystal-field split-off (CH). Red markers are the Γ-point Bloch functions, which transform like s and p orbitals. VB states are split at the Γ-point by the spin orbit coupling and crystal field. (b) Splitting of the Γ-point VB degeneracies by spin orbit coupling and crystal-field.

3.1 Bulk $\mathbf{k} \cdot \mathbf{p}$ without spin-orbit coupling and strain

Let us start by deriving the $\mathbf{k} \cdot \mathbf{p}$ formulation. Consider a single electron in an infinite crystal lattice without spin-orbit coupling or strain. Schrödinger's time independent equation for the single electron is

$$\hat{H}_0 \left|\psi\right\rangle = E \left|\psi\right\rangle, \tag{3.1}$$

where

$$\hat{H}_0 = \frac{\hat{p}^2}{2m_0} + V\left(\mathbf{r}\right). \tag{3.2}$$

Here, $\hat{H}_0$ is the Hamiltonian, $\hat{\mathbf{p}}$ is the momentum operator, m_0 the electron mass, V potential energy due to the crystal lattice. Given the infinite lattice, the potential respects translation symmetry such that

$$V\left(\mathbf{r} + \mathbf{R}\right) = V\left(\mathbf{r}\right), \tag{3.3}$$

where $\mathbf{R}$ is any linear combination of the crystal lattice vectors. This periodicity allows us to write the eigenstates as Bloch waves [48]

$$\psi_{n,\mathbf{k}}\left(\mathbf{r}\right) = \mathrm{e}^{i\mathbf{k}\cdot\mathbf{r}} u_{n,\mathbf{k}}\left(\mathbf{r}\right), \tag{3.4}$$

where n is the band index and $\mathbf{k}$ a wave vector labeling the state within the first Brillouin zone of Fourier space. $u_{n,\mathbf{k}}$ are the Bloch functions, which have the same periodicity as the potential. Inserting Eq. 3.4 into Eq. 3.1 leads to

$$\hat{H}_{\mathbf{k}\cdot\mathbf{p}} \left|u_{n,\mathbf{k}}\right\rangle = E_{n,\mathbf{k}} \left|u_{n,\mathbf{k}}\right\rangle, \tag{3.5}$$

where

$$\hat{H}_{\mathbf{k}\cdot\mathbf{p}}(\mathbf{k}) = \hat{H}_0 + \frac{\hbar^2 k^2}{2m_0}\hat{I} + \frac{\hbar}{m_0}\mathbf{k}\cdot\hat{\mathbf{p}}. \tag{3.6}$$

Here, $\hat{H}_{\mathbf{k}\cdot\mathbf{p}}$ is referred to as the $\mathbf{k}\cdot\mathbf{p}$ Hamiltonian and acts on the functions $|u_{n,\mathbf{k}}\rangle$. We have therefore recast the original eigenvalue problem into a similar one for the Bloch functions. The goal is now to solve the eigenvalue problem to obtain $E_{n,\mathbf{k}}$ and $|u_{n,\mathbf{k}}\rangle$, giving us the band structure of the bulk crystal. The idea behind $\mathbf{k}\cdot\mathbf{p}$ theory is to calculate the band structure around some certain point $\mathbf{k}_0$ in k-space using the Bloch functions $u_{n,\mathbf{k}_0}$ as a basis. This is possible because the full set of Bloch functions $\{u_{n,k_0}|\forall n\}$ for a fixed wave vector $\mathbf{k}_0$ forms a complete and orthonormal set [30, 31, 33]. Consequently, we can expand $|u_{n,\mathbf{k}}\rangle$ using the $\mathbf{k_0}$ Bloch functions, leading to [33]

$$|u_{n,\mathbf{k}}\rangle = \sum_i A_i^n(\mathbf{k})\,|u_{i,\mathbf{k}_0}\rangle\,, \tag{3.7}$$

where $A_i^n(\mathbf{k})$ are the expansion coefficients. There are no known analytical solutions to such general eigenvalue problems, and it is numerically unfeasible to consider an infinite basis set, but one can use a subset of these Bloch functions to obtain an approximate solution. For solar applications, the states in the vicinity of the bandgap usually play the most important role as they are responsible for the absorption that leads to current production. In the case of wurtzite InGaN materials, the bandgap is located at the Γ-point ($\mathbf{k}=\mathbf{0}$), as sketched in Fig. 3.1. Closest in energy to the bandgap is the conduction band (CB), heavy hole band (HH), light hole band (LH) and crystal-field split-off band (CH). The Γ-point Bloch function of the CB transforms like an S orbital, while the three valence bands transform like P orbitals (X, Y and Z) [35, 39]. Choosing these Bloch functions with spin up and spin down gives us an 8-element basis we label as

$$\begin{aligned}
|u_1\rangle &= |S,\uparrow\rangle \quad & |u_5\rangle &= |S,\downarrow\rangle \\
|u_2\rangle &= |X,\uparrow\rangle \quad & |u_6\rangle &= |X,\downarrow\rangle \\
|u_3\rangle &= |Y,\uparrow\rangle \quad & |u_7\rangle &= |Y,\downarrow\rangle \\
|u_4\rangle &= |Z,\uparrow\rangle \quad & |u_8\rangle &= |Z,\downarrow\rangle\,.
\end{aligned} \tag{3.8}$$

With this finite basis, the eigenfunctions $|u_{n,\mathbf{k}}\rangle$ are then approximated as

$$|u_{n,\mathbf{k}}\rangle \approx \sum_{i=1}^{8} A_i^n(\mathbf{k})\,|u_i\rangle\,, \tag{3.9}$$

which becomes more accurate as more bands are included. The Hamiltonian in Eq. 3.6 can be written as an 8×8 matrix of the form

$$H_{\mathbf{k}\cdot\mathbf{p}}(\mathbf{k}) = \begin{bmatrix} \langle S\uparrow|\hat{H}_{\mathbf{k}\cdot\mathbf{p}}(\mathbf{k})|S\uparrow\rangle & \langle S\uparrow|\hat{H}_{\mathbf{k}\cdot\mathbf{p}}(\mathbf{k})|X\uparrow\rangle & \cdots & \langle S\uparrow|\hat{H}_{\mathbf{k}\cdot\mathbf{p}}(\mathbf{k})|Z\downarrow\rangle \\ \langle X\uparrow|\hat{H}_{\mathbf{k}\cdot\mathbf{p}}(\mathbf{k})|S\uparrow\rangle & \langle X\uparrow|\hat{H}_{\mathbf{k}\cdot\mathbf{p}}(\mathbf{k})|X\uparrow\rangle & \cdots & \vdots \\ \vdots & \vdots & \ddots & \vdots \\ \langle Z\downarrow|\hat{H}_{\mathbf{k}\cdot\mathbf{p}}(\mathbf{k})|S\uparrow\rangle & \cdots & \cdots & \langle Z\downarrow|\hat{H}_{\mathbf{k}\cdot\mathbf{p}}(\mathbf{k})|Z\downarrow\rangle \end{bmatrix}. \tag{3.10}$$

One now needs to calculate the matrix elements $\langle u_m|\hat{H}_{\mathbf{k}\cdot\mathbf{p}}(\mathbf{k})|u_n\rangle$, where $\hat{H}_{\mathbf{k}\cdot\mathbf{p}}$ is defined in Eq. 3.6.

In evaluating the matrix elements contained in 3.10, we encounter momentum matrix elements of the form $\langle u_m|\hat{p}_\alpha|u_n\rangle$, where $\hat{p}_\alpha$ is the α^{th} component of the momentum operator. Many of these matrix elements are zero and to eliminate them efficiently, we make use of some elements of group theory [49–52]. The rotational symmetry of the wurtzite crystal structure is described by the C_{6v} point group and each of the Γ-point Bloch functions transform according to an irreducible representation Γ_i of the point group[1]. Thus, the matrix element $\langle u_m|\hat{p}_\alpha|u_n\rangle$ can be written in terms of the irreducible representation that describe how each piece transforms

$$\langle\Gamma_i|\hat{p}_\alpha|\Gamma_k\rangle\,.$$

Here $|\Gamma_i\rangle$ is a Γ-point Bloch function which transforms according to the Γ_i irreducible representation. Similar to the Bloch functions, the momentum components $\hat{p}_\alpha$ also transform according to some Γ_j irreducible representation. In the case of wurtzite materials, X, Y, $\hat{p}_x$, and $\hat{p}_y$ belong to Γ_6, while S, Z and $\hat{p}_z$ belong to Γ_1 [30]. The matrix element can be represented as a direct product, which can then be decomposed into direct sums of the irreducible representation of the group,

$$\langle\Gamma_i|\hat{p}_\alpha|\Gamma_k\rangle : \Gamma_i\otimes\Gamma_j\otimes\Gamma_k = \Gamma_u\oplus\Gamma_v\oplus\cdots \tag{3.11}$$

Here, $\otimes$ indicates a direct product and $\oplus$ a direct sum. For the matrix element in Eq. 3.11 to be nonzero, the decomposition $\Gamma_u\oplus\Gamma_v\oplus\cdots$ must contain the Γ_1 irreducible representation since the matrix element is a scalar and must be invariant under all the C_{6v} operations. Stated otherwise, the direct product $\Gamma_j\otimes\Gamma_k$ must contain Γ_i. This gives the ability to efficiently eliminate a great number of matrix elements and only keep what is nonzero.

In the case of wurtzite materials, the nonzero matrix elements are [35]

$$\langle S|\hat{p}_z|Z\rangle \equiv i\frac{m_0}{\hbar}P_1 \tag{3.12}$$

$$\langle S|\hat{p}_x|Y\rangle = \langle S|\hat{p}_y|Y\rangle \equiv i\frac{m_0}{\hbar}P_2 \tag{3.13}$$

$$\langle S|\hat{H}_0|S\rangle = E_{\mathsf{C}} \tag{3.14}$$

[1] Do not mistake the irreducible representations Γ_i with the high symmetry point Γ as they are different concepts.

$$\langle X|\hat{H}_0|X\rangle = \langle Y|\hat{H}_0|Y\rangle = E_{\mathsf{V}} + \Delta_{\mathsf{cr}} \tag{3.15}$$

$$\langle Z|\hat{H}_0|Z\rangle = E_{\mathsf{V}} \tag{3.16}$$

Here, P_1 and P_2 are known as Kane parameters, E_c and E_v are the CB and VB bare band edge energies, and Δ_{cr} is the crystal field splitting. The crystal field splitting is caused by the Z functions experiencing a different potential energy than the X and Y functions due to the wurtzite crystal structure, which is hexagonal in symmetry. This difference in experienced potential results in a splitting of the CH band from the HH and LH bands, hence the name "crystal-field split-off". The spin-orbit coupling will be discussed later in Sec. 3.4. With these definitions, the $\mathbf{k}\cdot\mathbf{p}$ Hamiltonian from Eq. 3.10 can be written

$$H^1_{\mathbf{k}\cdot\mathbf{p}}(\mathbf{k}) = \frac{\hbar^2 k^2}{2m_0} I_{8\times 8} + H_1(\mathbf{k}), \tag{3.17}$$

where

$$H_1(\mathbf{k}) = \begin{bmatrix} G_1(\mathbf{k}) & 0 \\ 0 & G_1(\mathbf{k}) \end{bmatrix} \tag{3.18}$$

$$G_1(\mathbf{k}) = \begin{bmatrix} E_{\mathsf{C}} & iP_2k_x & iP_2k_y & iP_1k_z \\ -iP_2k_x & E_{\mathsf{V}}+\Delta_{\mathsf{cr}} & 0 & 0 \\ -iP_2k_y & 0 & E_{\mathsf{V}}+\Delta_{\mathsf{cr}} & 0 \\ -iP_1k_z & 0 & 0 & E_{\mathsf{V}} \end{bmatrix}. \tag{3.19}$$

We have neglected time-reversal symmetry in constructing this Hamiltonian, which leads to conjugation of the lower right block, as we show in Sec. 3.2. For this reason, the Hamiltonian in Eq. 3.17 is incorrect and differs from the Hamiltonians of Refs. [35] and [39], which do have the proper form. By taking small k and approximating the bands to be parabolic, we can express the Kane parameters in terms of effective masses [35, 39]

$$\begin{aligned} P_1^2 &= \frac{\hbar^2}{2m_0}\left(\frac{m_0}{m_{\mathsf{e}}^{\parallel}} - 1\right)(E_{\mathsf{CV}} + \Delta_{\mathsf{cr}}) \\ P_2^2 &= \frac{\hbar^2}{2m_0}\left(\frac{m_0}{m_{\mathsf{e}}^{\perp}} - 1\right)\frac{E_{\mathsf{CV}}^2 + \Delta_{\mathsf{cr}}}{E_{\mathsf{CV}} + \Delta_{\mathsf{cr}}}. \end{aligned} \tag{3.20}$$

Here, $m_{\mathsf{e}}^{\parallel}$ is the electron's effective mass along the z-direction and $m_{\mathsf{e}}^{\perp}$ in the xy-plane. These expressions will be rewritten in Sec. 3.4 to include spin-orbit coupling. The Hamiltonian in Eq. 3.17 is referred to as an 8-band $\mathbf{k}\cdot\mathbf{p}$ model that is first order in k, as indicated by the subscript and superscripts "1" . The Hamiltonian is block diagonal because there is no spin-orbit coupling included, reducing the problem to two uncoupled 4-band systems. We show, later in this chapter, that the Hamiltonian in Eq. 3.17 produces an inaccurate band structure in the vicinity of the Γ-point, which is due to the limited number of bands included in the model. In Sec. 3.3, we improve

the model by adding perturbative effects from previously neglected bands, spin-orbit coupling and strain. However, this Hamiltonian is not time reversal invariant, which must be fixed before adding those additional effects.

3.2 Time-reversal symmetry

Time-reversal symmetry has very important consequences for fermionic systems. In the case of a half-integer spin system that is invariant under time-reversal symmetry, the eigenstates are all at least doubly degenerate, which is known as Kramers' degeneracy. In this section, we start by showing basic properties of time reversal for a free electron [53] and then generalize for single electrons in a crystal. We show that the $\mathbf{k}\cdot\mathbf{p}$ Hamiltonian in Eq. 3.17 does not respect time reversal symmetry and present a method to construct one by explicitly using properties of the time reversal operator.

3.2.1 Time reversal for a free electron

Let us consider a single electron, which has spin 1/2. In the S_z eigenfunctions basis, $|+\rangle$ and $|-\rangle$, we can write a general spin state $|\alpha\rangle$ as

$$\begin{aligned} |\alpha\rangle &= \left(\sum_{s=+,-} |s\rangle\langle s|\right)|\alpha\rangle \\ &= \begin{bmatrix} \alpha^+ \\ \alpha^- \end{bmatrix} \end{aligned} \tag{3.21}$$

where $\alpha^{\pm} = \langle \pm|\alpha\rangle$. In the S_z basis, the time reversal operator can be written [53]

$$\hat{T} = -i\sigma_y \hat{C}, \tag{3.22}$$

where $\hat{C}$ is the complex conjugation operator and only acts on scalars and not on the $|\pm\rangle$ basis. σ_i are Pauli spin matrices such that

$$\begin{aligned} \sigma_x &= \begin{bmatrix} 0 & 1 \\ 1 & 0 \end{bmatrix} \\ \sigma_y &= \begin{bmatrix} 0 & -i \\ i & 0 \end{bmatrix} \\ \sigma_z &= \begin{bmatrix} 1 & 0 \\ 0 & -1 \end{bmatrix}. \end{aligned} \tag{3.23}$$

Note that Eq. 3.22 is written specifically for the S_z basis and that the form of time reversal operator is basis dependent. The representation of $\hat{T}$ in Eq. 3.22 is basis-dependent because it is an anti linear operator [53].

Let us now show some properties of $\hat{T}$. To begin, we apply $\hat{T}$ on the state $|\alpha\rangle$ to obtain

$$\hat{T}\,|\alpha\rangle = -i \begin{bmatrix} 0 & -i \\ i & 0 \end{bmatrix} \hat{C} \begin{bmatrix} \alpha^{+} \\ \alpha^{-} \end{bmatrix} = \begin{bmatrix} -\alpha^{-*} \\ \alpha^{+*} \end{bmatrix}, \tag{3.24}$$

which can be understood as a flipping of spins and change in phases. Applying $\hat{T}$ a second time leads to

$$\begin{aligned} \hat{T}^2\,|\alpha\rangle &= \hat{T}\left(\hat{T}\,|\alpha\rangle\right) \\ &= \hat{T} \begin{bmatrix} -\alpha^{-*} \\ \alpha^{+*} \end{bmatrix} \\ &= - \begin{bmatrix} \alpha^{+} \\ \alpha^{-} \end{bmatrix} \\ &= -\,|\alpha\rangle\,, \end{aligned}$$

from which we conclude that

$$\hat{T}^2 = -1. \tag{3.25}$$

Note that $\hat{T}$ is an anti-unitary operator and so satisfies the following properties:

$$\hat{T}\left(|\alpha\rangle + |\beta\rangle\right) = \hat{T}\,|\alpha\rangle + \hat{T}\,|\beta\rangle \tag{3.26}$$

$$\hat{T}a\,|\alpha\rangle = a^{*}\hat{T}\,|\alpha\rangle \tag{3.27}$$

$$\langle \hat{T}\alpha|\hat{T}\beta\rangle = \begin{bmatrix} -\alpha^{-} & \alpha^{+} \end{bmatrix} \begin{bmatrix} -\beta^{-*} \\ \beta^{+*} \end{bmatrix} = \langle\alpha|\beta\rangle^{*}\,, \tag{3.28}$$

where a is an arbitrary constant, $|\alpha\rangle$ and $|\beta\rangle$ are general spin states and $|\hat{T}\alpha\rangle \equiv \hat{T}\,|\alpha\rangle$. Equation 3.28 means that the time-reversal operator preserves the orthogonality between states, which will be important for us further below. Additionally, we also have

$$\langle \hat{T}\alpha|\alpha\rangle = \begin{bmatrix} -\alpha^{-} & \alpha^{+} \end{bmatrix} \begin{bmatrix} \alpha^{+} \\ \alpha^{-} \end{bmatrix} = 0, \tag{3.29}$$

which means that time reversed states are orthogonal to the original state.

If an operator $\hat{\Lambda}$ is invariant under time-reversal symmetry, then the two operators must commute:

$$\left[\hat{\Lambda}, \hat{T}\right] = \hat{\Lambda}\hat{T} - \hat{T}\hat{\Lambda} = 0. \tag{3.30}$$

In this case, we can use Eq. 3.28 to evaluate time-reversed matrix elements,

$$\begin{aligned}
\langle \hat{T}\alpha|\hat{\Lambda}|\hat{T}\beta\rangle &= \langle \hat{T}\alpha|\hat{\Lambda}\hat{T}\beta\rangle \\
&= \langle \hat{T}\alpha|\hat{T}\hat{\Lambda}\beta\rangle \\
&= \langle \alpha|\hat{\Lambda}\beta\rangle^* \\
&= \langle \alpha|\hat{\Lambda}|\beta\rangle^*
\end{aligned} \tag{3.31}$$

If a Hamiltonian, with eigenvalues E and eigenfunctions $|\psi\rangle$, is time-reversal invariant, then we can write

$$\begin{aligned}
\hat{T}\hat{H}\,|\psi\rangle &= \hat{T}\hat{H}\,|\psi\rangle \\
\hat{H}\hat{T}\,|\psi\rangle &= \hat{T}\hat{H}\,|\psi\rangle \\
\hat{H}\hat{T}\,|\psi\rangle &= \hat{T}E\,|\psi\rangle \\
\hat{H}\hat{T}\,|\psi\rangle &= E\hat{T}\,|\psi\rangle
\end{aligned} \tag{3.32}$$

which states that $|\psi\rangle$ and $\hat{T}\,|\psi\rangle$ form degenerate states, which is known as Kramers' degeneracy. Let us now prove that time-reversed states are distinct from each other. Let's assume that

$$\hat{T}\,|\psi\rangle = A\,|\psi\rangle\,, \tag{3.33}$$

where A is an arbitrary constant. If we apply $\hat{T}$ to both sides, it follows that

$$\begin{aligned}
\hat{T}^2\,|\psi\rangle &= \hat{T}A\,|\psi\rangle \\
\hat{T}^2\,|\psi\rangle &= A^*\hat{T}\,|\psi\rangle \\
\hat{T}^2\,|\psi\rangle &= |A|^2\,|\psi\rangle\,.
\end{aligned} \tag{3.34}$$

However, $\hat{T}^2 = -1$ for spin 1/2 systems, meaning we have a contradiction and that the state $|\psi\rangle$ and it's time reversed partner $\hat{T}\,|\psi\rangle$ form a linearly independent set. This result is in agreement with Eq. 3.29, where we had shown that the states are orthogonal and so can not be scalar multiples of each other.

3.2.2 Time reversal for multiple bands

Now, let us consider time-reversal within a crystalline material. Applying the time-reversal operator to a Bloch wave flips the wave vector and spin of the state such that [50, 52]

$$\hat{T}\left|\psi_{n,s}\left(\mathbf{k}\right)\right\rangle = \left|\psi_{n,-s}\left(-\mathbf{k}\right)\right\rangle. \tag{3.35}$$

Due to Kramers degeneracy, this means states with reflected wave vectors and spin are degenerate in energy. In the case of the Γ-point Bloch functions, which have $\mathbf{k}=\mathbf{0}$, $\hat{T}$ maps between the spin up and spin down functions

$$\hat{T}\left|\psi_{n,s}\left(\mathbf{0}\right)\right\rangle = \left|\psi_{n,-s}\left(\mathbf{0}\right)\right\rangle \tag{3.36}$$

Since for $\mathbf{k}=\mathbf{0}$ we have that $\psi_{n,s}\left(\mathbf{0}\right)=u_{n,-s}\left(\mathbf{0}\right)$, this mapping is also true for the Γ-Bloch functions, giving

$$\hat{T}\left|u_{n,s}\left(\mathbf{0}\right)\right\rangle = \left|u_{n,-s}\left(\mathbf{0}\right)\right\rangle. \tag{3.37}$$

The $\mathbf{k}\cdot\mathbf{p}$ Hamiltonian in Eq. 3.17 was obtained using the basis in Eq. 3.8. Equation 3.37 tells us how $\hat{T}$ acts on the basis and we can now explicitly use $\hat{T}$ to write the basis as

$$\begin{aligned}
\left|u_1\right\rangle &= \left|S,\uparrow\right\rangle \quad & \left|u_5\right\rangle &= \hat{T}\left|u_1\right\rangle \\
\left|u_2\right\rangle &= \left|X,\uparrow\right\rangle \quad & \left|u_6\right\rangle &= \hat{T}\left|u_2\right\rangle \\
\left|u_3\right\rangle &= \left|Y,\uparrow\right\rangle \quad & \left|u_7\right\rangle &= \hat{T}\left|u_3\right\rangle \\
\left|u_4\right\rangle &= \left|Z,\uparrow\right\rangle \quad & \left|u_8\right\rangle &= \hat{T}\left|u_4\right\rangle,
\end{aligned} \tag{3.38}$$

which is called a Kramers basis [32]. A general state in the space spanned by this basis can then be written

$$\left|\alpha\right\rangle = \begin{bmatrix} \boldsymbol{\alpha}^{+} \\ \boldsymbol{\alpha}^{-} \end{bmatrix},$$

where

$$\boldsymbol{\alpha}^{\pm} = \begin{bmatrix} \langle u_{1,},\pm|\alpha\rangle \\ \langle u_{2,},\pm|\alpha\rangle \\ \langle u_{3,},\pm|\alpha\rangle \\ \langle u_{4,},\pm|\alpha\rangle \end{bmatrix}.$$

To preserve $\hat{T}^2=-1$ and to have the correct mapping between the Γ-point functions shown in Eq. 3.37, we choose the following representation

$$\hat{T} = -i\sigma\hat{C}, \tag{3.39}$$

where

$$\sigma = \begin{bmatrix} 0 & -iI_{4x4} \\ iI_{4x4} & 0 \end{bmatrix}. \tag{3.40}$$

This form of $\hat{T}$ is analogous to Eq. 3.22, but has been enlarged to accommodate the orbital space. The matrix σ plays the same role as σ_y did for the spin degree of freedom of the free electron in Eq. 3.22. Applying $\hat{T}$ on a general state $|\alpha\rangle$ gives

$$\hat{T}\,|\alpha\rangle = -i \begin{bmatrix} 0 & -iI_{4x4} \\ iI_{4x4} & 0 \end{bmatrix} \hat{C} \begin{bmatrix} \boldsymbol{\alpha}^{+} \\ \boldsymbol{\alpha}^{-} \end{bmatrix} = \begin{bmatrix} -\boldsymbol{\alpha}^{-*} \\ \boldsymbol{\alpha}^{+*} \end{bmatrix}, \tag{3.41}$$

where the spin is flipped similarly to the free electron, but the spatial functions are left unchanged as stated in Eq. 3.37. The time-reversal operator, as defined by Eq. 3.39, also satisfies

$$\hat{T}^2\,|\alpha\rangle = -\,|\alpha\rangle \tag{3.42}$$

$$\langle \hat{T}\alpha|\alpha\rangle = 0 \tag{3.43}$$

$$\langle \hat{T}\alpha|\hat{T}\beta\rangle = \langle\alpha|\beta\rangle^{*}, \tag{3.44}$$

which are the equivalent to Eqs. 3.25, 3.29 and 3.28. If we now calculate the commutator between the time-reversal operator and the Hamiltonian from Eq. 3.17, we find

$$\begin{aligned}\left[\hat{T}, \hat{H}^{1}_{\mathbf{k}\cdot\mathbf{p}}(\mathbf{k})\right] &= \begin{bmatrix} 0 & G_1(\mathbf{k}) - G_1^{*}(\mathbf{k}) \\ G_1^{*}(\mathbf{k}) - G_1(\mathbf{k}) & 0 \end{bmatrix} \hat{C} \\ &\neq 0,\end{aligned} \tag{3.45}$$

which indicates that the Hamiltonian does not respect time-reversal symmetry. Note if $G_1(\mathbf{k})$ were purely real, then the Hamiltonian would indeed commute with $\hat{T}$, however $G_1(\mathbf{k})$ is complex, as shown in Eq. 3.19. To remedy this, we can construct a new Hamiltonian from the Kramers basis in Eq. 3.38 by using Eq. 3.44 to write the spin down block as

$$\langle \hat{T}u_i|H|\hat{T}u_j\rangle = \langle u_i|H|u_j\rangle^{*}, \tag{3.46}$$

leading to the Hamiltonian

$$H^1_{\mathbf{k}\cdot\mathbf{p}}(\mathbf{k}) = \frac{\hbar^2 k^2}{2m_0} I_{8\times 8} + \begin{bmatrix} G_1(\mathbf{k}) & 0 \\ 0 & G_1^*(\mathbf{k}) \end{bmatrix}, \tag{3.47}$$

which does satisfy $\left[\hat{T}, \hat{H}\right] = 0$, implying a time-reversal invariant Hamiltonian.

One may ask why the original Hamiltonian didn't respect time reversal symmetry and had to be corrected afterwards. The nature of the problem is introduced when one takes the orbital space and enlarges it to include spin. To illustrate this, let us consider a system with no spin-orbit coupling in which case we have two uncoupled spaces, that of the orbitals and that of the spins:

$$\mathscr{H} = \mathscr{H}_{\mathsf{orb}} \otimes \mathscr{H}_s. \tag{3.48}$$

In the orbital space, we have the Hamiltonian being simply the constant terms and k-dependent terms calculated previously:

$$H_{\mathsf{orb}}(\mathbf{k}) = \frac{\hbar^2 k^2}{2m_0} I_{4\times 4} + G_1(\mathbf{k}) \tag{3.49}$$

When we proceed to include spin and augment this operator to the full space $\mathscr{H}$, the natural thing to do is to assert that

$$H(\mathbf{k}) = H_{\mathsf{orb}}(\mathbf{k}) \otimes I_{2\times 2} \tag{3.50}$$

$$= \frac{\hbar^2 k^2}{2m_0} I_{8\times 8} + \begin{bmatrix} G_1(\mathbf{k}) & 0 \\ 0 & G_1(\mathbf{k}) \end{bmatrix} \tag{3.51}$$

However, we do have certain degrees of freedom with how we proceed. Let us consider a transformation U which diagonalizes the Hamiltonian, allowing us to write

$$UHU^{-1} = H_d. \tag{3.52}$$

Since the Hamiltonian is Hermitian, meaning it is real in its diagonal form, we can take the complex conjugate and obtain

$$\left(UHU^{-1}\right)^* = H_d$$

$$U^* H^* U^{-1*} = H_d. \tag{3.53}$$

If we have that U^{-1} is the inverse of U, then it is also the case for their complex conjugated counterparts,

$$\begin{aligned} UU^{-1} &= 1 \\ \left(UU^{-1}\right)^* &= (1)^* \\ U^*U^{-1*} &= 1, \end{aligned} \tag{3.54}$$

and consequently

$$U^{'}H^*U^{'-1} = H_d, \tag{3.55}$$

where

$$U^{'} = U^*. \tag{3.56}$$

The eigenvalues of H^* are then the same as those of H, H^* is simply diagonalized by a different unitary transformation. This means we could instead construct the full space Hamiltonian as

$$H^1_{\mathbf{k}\cdot\mathbf{p}}(\mathbf{k}) = \frac{\hbar^2k^2}{2m_0}I_{8\times8} + \begin{bmatrix} G_1(\mathbf{k}) & 0 \\ 0 & G_1^*(\mathbf{k}) \end{bmatrix} \tag{3.57}$$

and still obtain the same eigenvalues, while respecting time reversal symmetry. One can then proceed to add spin-orbit coupling and other effects and continue to preserve the symmetry. The problem seems to be that we cannot simply augment the orbital space to include the spin space in the trivial fashion of Eq. 3.51. The naive expansion of the orbital Hamiltonian to the spin space (Eq. 3.51) is not compatible with any representation of $\hat{T}$ with $\hat{T}^2 = -1$.

Now having corrected the Hamiltonian to respect time reversal symmetry, Fig. 3.2 shows the dispersions calculated from Eq. 3.57 for GaN. In these results, we have also ignored the crystal-field splitting by putting $\Delta_{\mathsf{cr}} = 0$, which simply shifts some of the VBs. Most importantly, we find that the HH and LH bands disperse positively in k, closing the bandgap. It is expected that the $\mathbf{k}\cdot\mathbf{p}$ method will break down at some value of k, but the VBs are obviously incorrect for all $\mathbf{k}$, except at the Γ-point. These results could be improved by adding more and more bands until satisfied, but one might find themselves needing an increasing number of bands and parameters. Alternatively, one can add perturbative effects from remote bands, as is done in the following section.

3.3 Löwdin perturbation theory

We now look to refining the $\mathbf{k}\cdot\mathbf{p}$ Hamiltonian by adding effects from previously neglected bands, which are necessary for obtaining reasonably accurate band structure. Spin-orbit coupling and strain are introduced in the following section.

Until now, we have limited ourselves to the S, X, Y and Z Bloch functions in calculating the band structure

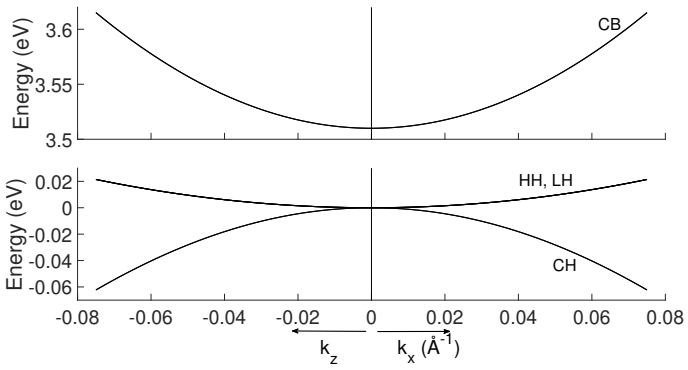

Figure 3.2: Band structure around the Γ-point for GaN, calculated from Eq. 3.57 with material parameters listed in Table A.1 from Appendix A. Left side panel is the band structure along the k_z direction, while right is for k_x. k_z is along the c-axis of the wurtzite crystal structure while k_x is in-plane. Shown are the conduction (CB), heavy hole (HH), light hole (LH), and crystal-field split-off (CH) bands, which are all doubly degenerate. The zero-energy point has been fixed to the valence band edge without spin-orbit and crystal-field.

of the wurtzite system. As shown in Fig. 3.2, such a model does not produce accurate valence bands and effects from other bands must be included for more accurate results. We could in principle include more bands in the eigenfunction expansion of Eq. 3.9 to achieve better accuracy. However, such an approach would also require an increasing number of parameters, requiring more theoretical and experimental work. Instead, we will use Löwdin perturbation theory [54] to treat the effects of outside bands. Löwdin perturbation theory divides the Γ-point Bloch functions into two classes. Class A consists of the bands whose interactions we treat explicitly, which are the Bloch functions already considered:

$$A = \{S, X, Y, Z\} \otimes \{\uparrow, \downarrow\}. \tag{3.58}$$

Class B consists of all other bands not included in A and are to be treated as a perturbation. Using Löwdin perturbation up to second order in k leads to the Hamiltonian [35, 39, 54]

$$H^2_{\mathbf{k}\cdot\mathbf{p},ij}(\mathbf{k}) = \frac{\hbar^2 k^2}{2m_0}\delta_{ij} + H_{1,ij}(\mathbf{k}) + \frac{\hbar^2}{2m_0}\sum_{\alpha,\beta=x,y,z}\sum_{\gamma\in B}\frac{\langle i|p_\alpha|\gamma\rangle\langle\gamma|p_\beta|j\rangle + \langle i|p_\beta|\gamma\rangle\langle\gamma|p_\alpha|j\rangle}{m_0(E_0 - E_\gamma)}k_\alpha k_\beta \tag{3.59}$$

where the last term on the right-hand side contains the perturbations due to the B class. The indices i and j indicate the bands and so take values 1 to 8. The superscript "2" indicates that it is second order in k. As discussed in Sec. 3.1, many of the $\langle i|p_\alpha|\gamma\rangle$ matrix elements are zero, depending on the symmetry of the states. The remaining nonzero matrix elements are not calculated directly and are therefore expressed as parameters, which are determined from fitting the $\mathbf{k}\cdot\mathbf{p}$ theory to experimental data or a more fundamental theory [36, 55, 56]. Carrying out the symmetry analysis gives [35, 39]

$$H^2_{\mathbf{k}\cdot\mathbf{p}}(\mathbf{k}) = \begin{bmatrix} G(\mathbf{k}) & 0 \\ 0 & G^*(\mathbf{k}) \end{bmatrix}, \tag{3.60}$$

where

$$G\left(\mathbf{k}\right)=G_1\left(\mathbf{k}\right)+G_2\left(\mathbf{k}\right) \tag{3.61}$$

$$G_2\left(\mathbf{k}\right)=\begin{bmatrix} A_2'\left(k_x^2+k_y^2\right)+A_1'k_z^2 & 0 & 0 & 0 \\ 0 & L_1'k_x^2+M_1k_y^2+M_2k_z^2 & N_1'k_xk_y & N_2'k_xk_z \\ 0 & N_1'k_yk_x & M_1k_x^2+L_1'k_y^2+M_2k_z^2 & N_2'k_yk_z \\ 0 & N_2'k_zk_x & N_2'k_zk_y & M_3\left(k_x^2+k_y^2\right)+L_2'k_z^2 \end{bmatrix}, \tag{3.62}$$

where A_i', L_i', M_i and N_i' contain the additional matrix elements introduced by the B class bands and are defined in Appendix A in terms of the Luttinger-related parameters A_i (Eq. A.12). The A_i are material dependent and are precisely the parameters determined by fitting the $\mathbf{k}\cdot\mathbf{p}$ model to experiments or theories.

3.4 Spin-orbit coupling and strain

Until now, we have neglected spin orbit coupling, leading to Hamiltonians that are block diagonal in spin. However, spin-orbit coupling can be included in the Hamiltonian from Eq. 3.2 as [32]

$$H_0^{\mathsf{so}}=\frac{\hbar}{4m_0^2c^2}\left(\boldsymbol{\nabla}V\times\mathbf{p}\right)\cdot\boldsymbol{\sigma}, \tag{3.63}$$

where

$$\boldsymbol{\sigma}=(\sigma_x,\sigma_y,\sigma_z). \tag{3.64}$$

Let's verify that H_0^{so} does respect time-reversal symmetry by calculating how it commutes with $\hat{T}$. Let's start with product $\hat{T}H_0^{\mathsf{so}}$ and use Eq. 3.22:

$$\begin{aligned}\hat{T}H_0^{\mathsf{so}}&=\hat{T}\frac{\hbar}{4m_0^2c^2}\left(\boldsymbol{\nabla}V\times\mathbf{p}\right)\cdot\boldsymbol{\sigma}\\&=\left(-i\sigma_y\hat{C}\right)\frac{\hbar}{4m_0^2c^2}\sum_{i=x,y,z}\left[\boldsymbol{\nabla}V\times(-i\hbar\boldsymbol{\nabla})\right]_i\sigma_i\\&=\frac{\hbar}{4m_0^2c^2}\sum_{i=x,y,z}\left[\boldsymbol{\nabla}V\times(-i\hbar\boldsymbol{\nabla})\right]_i i\sigma_y\hat{C}\sigma_i.\end{aligned} \tag{3.65}$$

The current goal is to move $\hat{T}$ to the right of H_0^{so}. To do so, we make use of the following anticommutator rules for the Pauli spin matrices:

$$\{\sigma_i,\sigma_j\}\equiv\sigma_i\sigma_j+\sigma_j\sigma_i=2\delta_{ij}I_{2\times2}, \tag{3.66}$$

to write

$$i\sigma_y\hat{C}\sigma_i=\sigma_i\left(-i\sigma_y\hat{C}\right)=\sigma_i\hat{T}, \tag{3.67}$$

which leads to

$$\begin{aligned}\hat{T}H_0^{\mathsf{so}} &= \frac{\hbar}{4m_0^2c^2}\sum_{i=x,y,z}\left[\boldsymbol{\nabla}V\times(-i\hbar\boldsymbol{\nabla})\right]_i\sigma_i\hat{T}\\ &= \frac{\hbar}{4m_0^2c^2}\left(\boldsymbol{\nabla}V\times\mathbf{p}\right)\cdot\boldsymbol{\sigma}\hat{T}\\ &= H_0^{\mathsf{so}}\hat{T}.\end{aligned} \tag{3.68}$$

We therefore conclude that $\left[H_0^{\mathsf{so}},\hat{T}\right]=0$ and that the spin-orbit coupling is indeed time-reversal invariant. Let's now see how this Hamiltonian translates to the space of the Bloch functions. Using the basis as written in Eq. 3.58, we can write the wavefunction as

$$\left|\psi_{n,\mathbf{k}}\right\rangle = \sum_{\alpha=1}^{4}\sum_{s=\uparrow,\downarrow}A_{i,s}^{n,\mathbf{k}}\left|\phi_{\mathbf{k}}\right\rangle\otimes\left|s\right\rangle \tag{3.69}$$

where

$$\left\langle\mathbf{r}|\phi_{\mathbf{k}}\right\rangle = e^{i\mathbf{k}\cdot\mathbf{r}}u_{\mathbf{0}}\left(\mathbf{r}\right)$$

Note that Eq. 3.69 is equivalent to Eq. 3.9 as we have only rewritten to highlight the tensor product of the orbital and spin spaces. The Pauli spin matrices in Eq. 3.63 only acts on the space of spins, while the rest only acts on the orbital portion of the wavefunction. We can therefore write

$$\begin{aligned}\hat{H}_0^{\mathsf{so}}\left|\psi_{n,\mathbf{k}}\right\rangle &= \left[\frac{\hbar}{4m_0^2c^2}\left(\boldsymbol{\nabla}V\times\hat{\mathbf{p}}\right)\cdot\boldsymbol{\sigma}\right]\left[\sum_{\alpha=1}^{4}\sum_{s=\uparrow,\downarrow}A_{i,s}^{n,\mathbf{k}}e^{i\mathbf{k}\cdot\mathbf{r}}u_{n,\mathbf{k}}\left(\mathbf{r}\right)\left|s\right\rangle\right]\\ &= \sum_{\alpha=1}^{4}\sum_{s=\uparrow,\downarrow}A_{i,s}^{n,\mathbf{k}}\left[\frac{\hbar}{4m_0^2c^2}\left(\boldsymbol{\nabla}V\times\hat{\mathbf{p}}\right)e^{i\mathbf{k}\cdot\mathbf{r}}u_{n,\mathbf{k}}\left(\mathbf{r}\right)\right]\cdot\boldsymbol{\sigma}\left|s\right\rangle\\ &= \sum_{\alpha=1}^{4}\sum_{s=\uparrow,\downarrow}A_{i,s}^{n,\mathbf{k}}\left[u_{n,\mathbf{k}}\left(\mathbf{r}\right)\left(\boldsymbol{\nabla}V\times\hat{\mathbf{p}}\right)e^{i\mathbf{k}\cdot\mathbf{r}}+e^{i\mathbf{k}\cdot\mathbf{r}}\left(\boldsymbol{\nabla}V\times\hat{\mathbf{p}}\right)u_{n,\mathbf{k}}\left(\mathbf{r}\right)\right]\cdot\boldsymbol{\sigma}\left|s\right\rangle\\ &= e^{i\mathbf{k}\cdot\mathbf{r}}\frac{\hbar}{4m_0^2c^2}\left[\hbar\left(\boldsymbol{\nabla}V\times\mathbf{k}\right)+\left(\boldsymbol{\nabla}V\times\hat{\mathbf{p}}\right)\right]\sum_{\alpha=1}^{4}\sum_{s=\uparrow,\downarrow}A_{i,s}^{n,\mathbf{k}}u_{n,\mathbf{k}}\left(\mathbf{r}\right)\cdot\boldsymbol{\sigma}\left|s\right\rangle\\ &= e^{i\mathbf{k}\cdot\mathbf{r}}\frac{\hbar}{4m_0^2c^2}\left[\hbar\left(\boldsymbol{\nabla}V\times\mathbf{k}\right)+\left(\boldsymbol{\nabla}V\times\hat{\mathbf{p}}\right)\right]\cdot\boldsymbol{\sigma}\left(\sum_{\alpha=1}^{4}\sum_{s=\uparrow,\downarrow}A_{i,s}^{n,\mathbf{k}}u_{n,\mathbf{k}}\left(\mathbf{r}\right)\left|s\right\rangle\right)\\ &= \mathsf{e}^{i\mathbf{k}\cdot\mathbf{r}}\hat{H}_{\mathsf{so}}\left|u_{n,\mathbf{k}}\right\rangle,\end{aligned}$$

where we have defined [32]

$$H_{\mathsf{so}} = \frac{\hbar}{4m_0^2c^2}\left(\boldsymbol{\nabla}V\times\mathbf{p}\right)\cdot\sigma+\frac{\hbar^2}{4m_0^2c^2}\left(\boldsymbol{\nabla}V\times\mathbf{k}\right)\cdot\sigma. \tag{3.70}$$

The first term is the spin-obit energy coming from the electron's orbit, while the second is from the crystal momentum. Typically, the second term is small compared to the first due to the velocity of the electrons in orbit being greater than the velocity of the wave packet associated to $\mathbf{k}$. It is therefore typical to neglect the second term and

approximate the spin-orbit coupling as [32]

$$H_{\mathsf{so}} \approx \hat{\mathbf{H}}_{\mathsf{S}} \cdot \sigma, \tag{3.71}$$

where

$$\hat{\mathbf{H}}_{\mathsf{S}} = \frac{\hbar}{4m_0^2c^2}\nabla V(\mathbf{r}) \times \hat{\mathbf{p}}. \tag{3.72}$$

The nonzero matrix elements for this contribution are [35]

$$\langle X|\hat{H}_{\mathsf{S}z}|Y\rangle = \langle Y|\hat{H}_{\mathsf{S}x}|Z\rangle = \langle Z|\hat{H}_{\mathsf{S}y}|X\rangle = -i\frac{1}{3}\Delta_{\mathsf{so}}. \tag{3.73}$$

For the spin component, the nonzero elements are

$$\begin{aligned} \langle\downarrow|\sigma_x|\uparrow\rangle &= 1 \\ \langle\downarrow|\sigma_y|\uparrow\rangle &= i \\ \langle\uparrow|\sigma_z|\uparrow\rangle &= 1 \\ \langle\downarrow|\sigma_z|\downarrow\rangle &= -1 \end{aligned} \tag{3.74}$$

The first two matrix elements in Eq. 3.74 couple the spin up and spin down blocks, removing the block diagonality of the Hamiltonian. The last two matrix elements couple the valence bands for both spins, splitting the HH and LH bands at the Γ-point.

Lastly, one can impose an external strain on a bulk crystal, deforming the lattice from its natural equilibrium. These deformations introduce deformation potentials in the Hamiltonian which modify the electronic structure. For small strains and neglecting its effects on spin-orbit coupling, strain can be included in the $\mathbf{k}\cdot\mathbf{p}$ Hamiltonian in the form [30, 39, 57]

$$H_{\mathsf{st}} = \begin{bmatrix} G_{\mathsf{st}} & 0 \\ 0 & G_{\mathsf{st}}^* \end{bmatrix}, \tag{3.75}$$

where a symmetry analysis of the wurtzite system results in

$$G_{\mathsf{st}} = \begin{bmatrix} a_2(\epsilon_{xx}+\epsilon_{yy}) + a_1\epsilon_{zz} & 0 & 0 & 0 \\ 0 & l_1\epsilon_{xx} + m_1\epsilon_{yy} + m_2\epsilon_{zz} & n_1\epsilon_{xy} & n_2\epsilon_{xz} \\ 0 & n_1\epsilon_{xy} & m_1\epsilon_{xx} + l_1\epsilon_{yy} + m_2\epsilon_{zz} & n_2\epsilon_{yz} \\ 0 & n_2\epsilon_{xz} & n_2\epsilon_{yz} & m_3(\epsilon_{xx}+\epsilon_{yy}) + l_2\epsilon_{zz} \end{bmatrix}, \tag{3.76}$$

with

$$\begin{aligned} l_1 &= D_2 + D_4 + D_5 \\ l_2 &= D_1 \\ m_1 &= D_2 + D_4 - D_5 \\ m_2 &= D_1 + D_3 \\ m_2 &= D_1 + D_3 \\ m_3 &= D_2 \\ n_1 &= 2D_5 \\ n_2 &= \sqrt{2}D_6. \end{aligned} \tag{3.77}$$

Here, ϵ_{ij} are the strain tensor components and D_i are the deformation potentials, which are, similarly to the A_i, material dependent parameters determined by fitting the model to experiment or theory.

With the additions of spin-orbit coupling and strain, the $\mathbf{k}\cdot\mathbf{p}$ Hamiltonian is written [39]

$$H_{\mathbf{k}\cdot\mathbf{p}}(\mathbf{k}) = \begin{bmatrix} G(\mathbf{k}) & \Gamma \\ -\Gamma^* & G^*(\mathbf{k}) \end{bmatrix}, \tag{3.78}$$

where

$$G(\mathbf{k}) = G_1(\mathbf{k}) + G_2(\mathbf{k}) + G_{\mathsf{so}} + G_{\mathsf{st}} \tag{3.79}$$

$$G_{\mathsf{so}} = \frac{\Delta_{\mathsf{so}}}{3}\begin{bmatrix} 0 & 0 & 0 & 0 \\ 0 & 0 & -i & 0 \\ 0 & i & 0 & 0 \\ 0 & 0 & 0 & 0 \end{bmatrix} \tag{3.80}$$

$$\Gamma = \frac{\Delta_{\mathsf{so}}}{3}\begin{bmatrix} 0 & 0 & 0 & 0 \\ 0 & 0 & 0 & 1 \\ 0 & 0 & 0 & -i \\ 0 & -1 & i & 0 \end{bmatrix} \tag{3.81}$$

and $G_1(\mathbf{k})$ and $G_2(\mathbf{k})$ are defined by Eqs. 3.19 and 3.62, respectively. Note that the matrix Γ is obtained from the nonzero matrix elements in Eqs. 3.73 and 3.74. Also, note that since we have included the effects of crystal field splitting in G_1, we do not have a term G_{cr} appearing in Eq. 3.79, which differs from the conventions of Ref. [39].

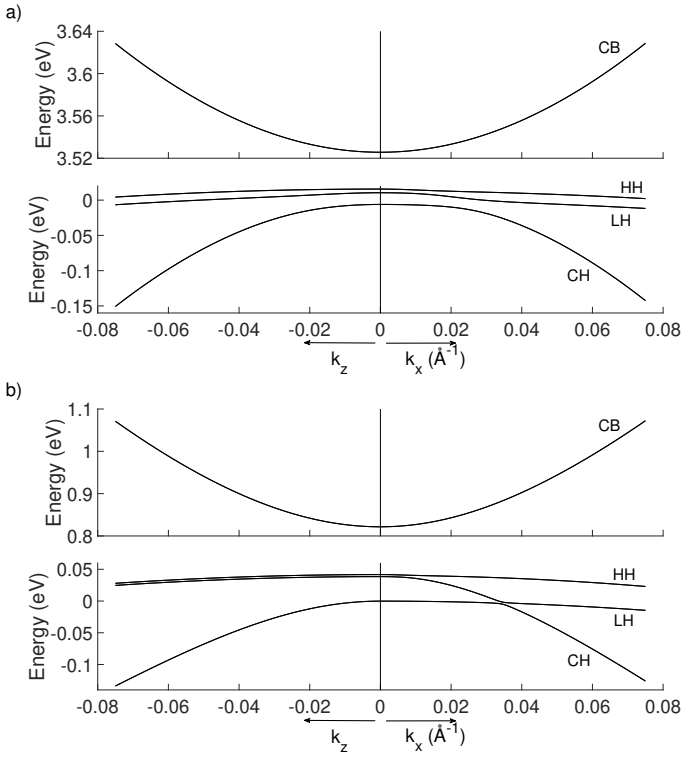

Figure 3.3: Band structure around the Γ-point for (a) GaN and (b) InN, which were calculated using Eq. 3.78 with parameters given in listed in Table A.1 from Appendix A. Left side of panels is the band structure along the k_z direction, while right is for k_x. k_z is along the c-axis of the wurtzite crystal structure while k_x is in-plane. Shown are the conduction (CB), heavy hole (HH), light hole (LH), and crystal-field split-off (CH) bands, which are all doubly degenerate. The zero-energy point has been fixed to the valence band edge without spin-orbit and crystal-field for both cases.

Having included spin-orbit coupling in the model, the Kane parameters from Eq. 3.20 become [35, 39]

$$\begin{aligned} P_1^2 &= \frac{\hbar^2}{2m_0}\left(\frac{m_0}{m_\mathrm{e}^{\parallel}}-1\right)\frac{3E_\mathrm{CV}\left(\Delta_\mathrm{so}+E_\mathrm{CV}\right)+\Delta_\mathrm{cr}\left(2\Delta_\mathrm{so}+3E_\mathrm{CV}\right)}{2\Delta_\mathrm{so}+3E_\mathrm{CV}} \\ P_2^2 &= \frac{\hbar^2}{2m_0}\left(\frac{m_0}{m_\mathrm{e}^{\perp}}-1\right)\frac{E_\mathrm{CV}\left[3E_\mathrm{CV}\left(\Delta_\mathrm{so}+E_\mathrm{CV}\right)\right]+\Delta_\mathrm{cr}\left(2\Delta_\mathrm{so}+3E_\mathrm{CV}\right)}{\Delta_\mathrm{cr}\Delta_\mathrm{so}+3\Delta_\mathrm{cr}E_\mathrm{CV}+2\Delta_\mathrm{so}E_\mathrm{CV}+3E_\mathrm{CV}^2}. \end{aligned} \tag{3.82}$$

Figure 3.3 shows the resulting band structure for both GaN and InN. Compared to Fig. 3.2, the VBs here have the correct curvature. These bulk states will now serve as a basis on which to construct a Hamiltonian for a QD system, as described in Chapter 4.

Chapter 4

$\mathbf{k} \cdot \mathbf{p}$ theory for quantum dots and optics

In the previous Chapter, we introduced the $\mathbf{k} \cdot \mathbf{p}$ method, where we use the crystal's discrete translation symmetry to write the eigenfunctions as Bloch waves. Naturally, this translation symmetry is broken when considering heterostructures, which consist of different materials. Let us consider the example of a heterojunction, which consists of two bulk materials. Although the translation symmetry is clearly broken at the material interface, the symmetry should be obeyed locally if far away from said material interface, in which case the wavefunction can be locally approximated as Bloch waves. However, the wavefunction must remain continuous, meaning it must continuously transform from one bulk state to the other as it crosses the junction. This slow transformation, which is due to a change in material, can be described by envelope functions, which are slowly varying with respect to the crystal lattice, while rapid variations due to the crystal lattice can be captured by Bloch functions. This envelope function approach can be applied to other heterostructures as well, such as QDs. As mentioned, it is assumed that these envelope functions are slowly varying with respect to the crystal lattice unit cell, which is accurate if the QD is large compared to the lattice constants [39, 41, 42, 58].

In this chapter, we look to describe the electronic structure and optical properties of QD superlattices, which is a periodic arrangement of QDs, such as shown in Fig. 4.1. Figure 4.1 shows an example of an hexagonal superlattice, which will be the system of focus in the Chapters 6 and 7, but the methods presented here can be applied to any superlattice. In this Chapter, we assume sharp material interfaces between the dot and host materials, and generalize for smoothly varying alloy profiles in Chapter 6. The standard method for extending the $\mathbf{k} \cdot \mathbf{p}$ method for QD systems is by using slowly varying envelope functions. The envelope functions are periodic with the superlattice and are expanded using a plane wave basis using the reciprocal wave vectors of the superlattice. This expansion leads to an eigenvalue problem for the eigenstate energies and expansion coefficients. The size of the matrix that is to be diagonalized in the eigenvalue problem depends on the number of wave vectors used to resolve the wavefunctions. In the case of the plane wave representation, the matrix is generally non-sparse and one can encounter memory issues if a large number of wave vectors is required for accuracy. However, the memory requirements of the numerical

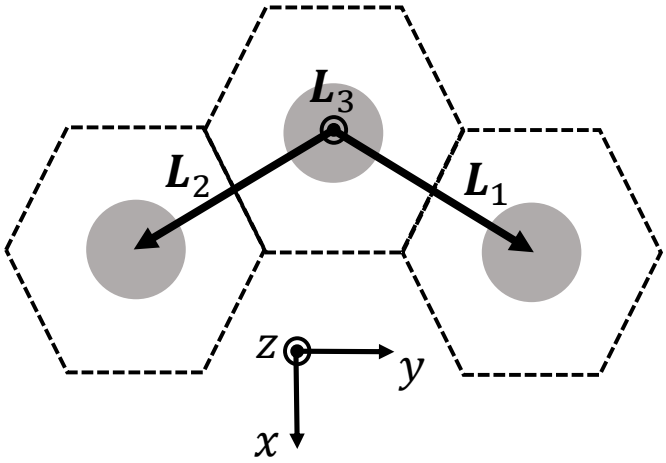

Figure 4.1: 3D InGaN/GaN quantum dot superlattice. White regions are GaN, the host material and grey regions indicate the indium rich regions, which are the QDs. Dashed lines indicate the unit cells and $\mathbf{L}_i$ are the basis vectors of the superlattice.

implementation can be reduced by taking advantage of the rotational symmetry of the QD system. In Chapter 6, we show how to construct a symmetry-adapted basis, which is more complicated than a simple plane-wave basis, but allows greater insight and computational efficiency.

The ultimate goal is to calculate optical absorption in the QD superlattice, which we can then use to predict power conversion efficiencies. In the second section of this chapter, we present a formalism to describe optical light absorption in the QD superlattice. The intensity of solar light is sufficiently weak that it does not modify the electronic structure of a QD system, but only causes the electrons to transition between the different states. We can therefore approximate the light-matter coupling as a perturbation on the original Hamiltonian used for the electronic structure. We then use Fermi's golden rule to calculate the transition rates between states in the QD superlattice, from which we are able to calculate absorption cross sections. In Chapter 7, we calculate absorptances from the absorption cross sections, which we couple into a detailed balance model to predict efficiencies. In the same chapter, we also a present a method that better captures the absorption from between the QD bound states and the continuum states of the host material compared to the method presented here.

4.1 Quantum dot $\mathbf{k}\cdot\mathbf{p}$ theory

When considering a bulk material, the wavefunctions are expanded in Eqs. 3.4 and 3.9 as

$$\psi_{n\mathbf{k}}(\mathbf{r}) = \sum_{\alpha=1}^{8} A_\alpha^n(\mathbf{k})\, e^{i\mathbf{k}\cdot\mathbf{r}} |u_\alpha\rangle . \tag{4.1}$$

In a quantum dot system, the material changes through the system and the eigenfunctions cannot be described a static mixture of Bloch waves as described by Eq. 4.1. To move to the quantum dot system, we proceed in an

analogous manner by expanding the wavefunction into Bloch functions, but by using envelope functions $F^{\alpha}(\mathbf{r})$, instead of simple constants. The expansion is therefore written

$$\psi_n(\mathbf{r}) = \sum_{\alpha=1}^{8} F_{\alpha}^{n}(\mathbf{r})\, u_{\alpha}(\mathbf{r}), \tag{4.2}$$

where envelope functions are responsible for capturing the changes in alloy profiles and the Bloch functions the rapid variations due to the crystalline potential. We assume that these envelope functions are slowly varying compared to the lattice constant, which is valid for QDs that are sufficiently big compared to said lattice constant. In this slowly varying envelope approximation, the envelope and Bloch functions vary on very different spatial scales such that the envelope functions can effectively be approximated as being constant on the scale of the crystal lattice unit cell. As a result, integrals involving the wavefunction can be approximated into products of two integrals; one over the envelope functions and one over the Bloch functions (See Appendix B). Using this approximation, the prescription to construct a QD Hamiltonian is to consider the eigenvalue problem [41, 42, 58, 59]

$$\sum_{\alpha=1}^{8} H_{\mathbf{k}\cdot\mathbf{p}}^{\alpha'\alpha} F_{\alpha}^{n}(\mathbf{r}) = E F_{\alpha'}^{n}(\mathbf{r}), \tag{4.3}$$

where $H_{\mathbf{k}\cdot\mathbf{p}}^{\alpha'\alpha}$ are the bulk Hamiltonian matrix elements from Eq. 3.78 (e.g. $H_{\mathbf{k}\cdot\mathbf{p}}^{11} = E_{\mathsf{C}} + A_2'\left(k_x^2 + k_y^2\right) + A_1' k_z^2 + a_2\left(\epsilon_{xx} + \epsilon_{yy}\right) + a_1\epsilon_{zz}$) such that

1. Material parameters are given a spatial dependence based on the alloy profile (e.g. $E_{\mathsf{C}} \to E_{\mathsf{C}}(\mathbf{r})$),
2. We apply the substitution $\mathbf{k} \to -i\boldsymbol{\nabla}$.

Appendix C presents a justification of this prescription.

Assuming sharp material interfaces between the dot and host material, the spatial dependence of material parameters can be described using a characteristic function $\chi_{\mathsf{d}}(\mathbf{r})$, which is 1 inside the dot and 0 outside. A material dependent parameter $f(\mathbf{r})$ (e.g. E_{c},A_2', etc...) can then be written

$$f(\mathbf{r}) = f_{\mathsf{d}}\chi_{\mathsf{d}}(\mathbf{r}) + f_{\mathsf{h}}\left[1 - \chi_{\mathsf{d}}(\mathbf{r})\right]. \tag{4.4}$$

Here, f_{d} and f_{h} are the parameter values of the host and alloyed dot material, respectively. In reality, devices often do not have sharp material interface, in which case the alloy profiles are smooth. An example of this is found in InGaN quantum dots grown by molecular beam epitaxy, where indium diffuses during the growth process [17]. Given that the electronic structure of QDs is sensitive to the alloy profile of the QDs, it is important to include smooth profiles in the modeling of such systems to have accurate results. In Chapter 6, we show that smoothly varying alloy profiles can be easily included by exchanging the characteristic function in the $\mathbf{k}\cdot\mathbf{p}$, strain, and piezoelectric potential calculations with a smoothly varying and normalized function.

As for point (2) of the list, discrete translation symmetry was used to write solutions as Bloch waves $\psi_{n\mathbf{k}}$ in the bulk system, where the wave vector $\mathbf{k}$ was a good quantum number. However, this translation symmetry is broken in a QD system, meaning $\mathbf{k}$ is no longer a good quantum number and the solutions cannot be expressed as pure Bloch waves. The substitution $\mathbf{k} \to -i\boldsymbol{\nabla}$ in the bulk matrix elements $H^{\alpha'\alpha}_{\mathbf{k}\cdot\mathbf{p}}$ can therefore be understood as a correction for the broken symmetry.

Following the substitution $\mathbf{k} \to -i\boldsymbol{\nabla}$, each $H^{\alpha'\alpha}_{\mathbf{k}\cdot\mathbf{p}}$ is regarded as an operator, which acts on the envelope functions. The envelope functions $F^n_\alpha(\mathbf{r})$ are periodic with the QD superlattice, which is shown in Fig. 4.1, and can be expanded in Fourier domain using the superlattice reciprocal wave vectors $\mathbf{q}$, which is written as

$$F^n_\alpha(\mathbf{r}) = \sum_{\mathbf{q}} C^n_{\alpha\mathbf{q}} \mathsf{e}^{i\mathbf{q}\cdot\mathbf{r}}, \tag{4.5}$$

such that

$$\psi_n(\mathbf{r}) = \sum_{\alpha=1}^{8}\sum_{\mathbf{q}} C^n_{\alpha\mathbf{q}} \mathsf{e}^{i\mathbf{q}\cdot\mathbf{r}} u_\alpha(\mathbf{r}), \tag{4.6}$$

with $C^n_{\alpha\mathbf{q}}$ being the expansion coefficients. These reciprocal wave vectors are written as

$$\mathbf{q} = m_1\mathbf{b}_1 + m_2\mathbf{b}_2 + m_3\mathbf{b}_3 \tag{4.7}$$

where $\mathbf{b}_i$ are the reciprocal basis vectors such that

$$\begin{aligned}
\mathbf{b}_1 &= \frac{2\pi}{L_1}[1,\ -\frac{1}{\sqrt{3}},\ 0] \\
\mathbf{b}_2 &= \frac{2\pi}{L_1}[1,\ \frac{1}{\sqrt{3}},\ 0] \\
\mathbf{b}_3 &= \frac{2\pi}{L_3}[0,\ 0,\ 1]
\end{aligned} \tag{4.8}$$

Here, $\mathbf{L}_i$ are the basis vectors of the QD superlattice in real space, as shown in Fig. 4.1. Note that the method presented here can be applied for QD superlattice of any periodicity. However, an hexagonal superlattice preserves the symmetry of the wurtzite crystal structure, which we will take advantage of in Chapter 6. Inserting Eq. 4.5 into Eq. 4.3, multiplying from the left with $\mathsf{e}^{-i\mathbf{q}'\cdot\mathbf{r}} u^*_{\alpha'}(\mathbf{r})$ and integrating over the volume V of the superlattice unit cell leads to

$$\sum_{\alpha=1}^{8}\sum_{\mathbf{q}} h^{\alpha'\alpha}(\mathbf{q}',\mathbf{q})\, C_{\alpha\mathbf{q}} \quad = \quad E C_{\alpha'\mathbf{q}'}, \tag{4.9}$$

where

$$h^{\alpha'\alpha}(\mathbf{q}',\mathbf{q}) \quad \equiv \quad \frac{1}{V}\int_V \mathsf{d}^3\mathbf{r}\, \mathsf{e}^{-i\mathbf{q}'\cdot\mathbf{r}} H^{\alpha'\alpha}_{\mathbf{k}\cdot\mathbf{p}} \mathsf{e}^{i\mathbf{q}\cdot\mathbf{r}}. \tag{4.10}$$

Equation 4.9 is an eigenvalue problem for the expansion coefficients, and we must now evaluate the matrix elements in Eq. 4.10. Given the substitution $\mathbf{k} \to -i\boldsymbol{\nabla}$, the matrix elements $H^{\alpha'\alpha}_{\mathbf{k}\cdot\mathbf{p}}$, with the exception of strain, can in general be written

$$H^{\alpha'\alpha}_{\mathbf{k}\cdot\mathbf{p}}(\mathbf{r}) = f^{\alpha'\alpha}(\mathbf{r}) + \sum_{i=x,y,z} f^{\alpha'\alpha}_i(\mathbf{r})\frac{\partial}{\partial x_i} + \sum_{i,j=x,y,z} f^{\alpha'\alpha}_{ij}(\mathbf{r})\frac{\partial^2}{\partial x_i \partial x_j}. \tag{4.11}$$

For example, in $H^{11}_{\mathbf{k}\cdot\mathbf{p}} = E_{\mathsf{C}} + A'_2\left(k_x^2 + k_y^2\right) + A'_1 k_z^2$, we would have $f^{11}(\mathbf{r}) = E_{\mathsf{C}}(\mathbf{r})$, $f^{11}_{xx}(\mathbf{r}) = f^{11}_{yy}(\mathbf{r}) = A'_2(\mathbf{r})$, and $f^{11}_{zz}(\mathbf{r}) = A'_1(\mathbf{r})$. The strain contributions to the Hamiltonian from Eq. 3.75 will be considered just below. Here, we consider sharp material interfaces and look for eigenstate such that the probability current is conserved across the interface. There has been much debate on how to exactly implement this boundary condition [60–64]. References [60–62, 64] showed that microscopic parameters, which are dependent on the interface and not only of the bulk materials, are needed for an accurate description. However, the approach typically used is a reordering of the operators in the Hamiltonian as to symmetrize them such that [41, 58, 65]

$$\begin{aligned}
&f^{\alpha'\alpha}(\mathbf{r}) \to f^{\alpha'\alpha}(\mathbf{r}) \\
&f^{\alpha'\alpha}_i(\mathbf{r})\frac{\partial}{\partial x_i} \to \frac{1}{2}\left(f^{\alpha'\alpha}_i(\mathbf{r})\frac{\partial}{\partial x_i} + \frac{\partial}{\partial x_i}f^{\alpha'\alpha}_i(\mathbf{r})\right) \\
&f^{\alpha'\alpha}_{ij}(\mathbf{r})\frac{\partial^2}{\partial x_i \partial x_j} \to \frac{1}{2}\left(\frac{\partial}{\partial x_i}f^{\alpha'\alpha}_{ij}(\mathbf{r})\frac{\partial}{\partial x_j} + \frac{\partial}{\partial x_j}f^{\alpha'\alpha}_{ij}(\mathbf{r})\frac{\partial}{\partial x_i}\right),
\end{aligned} \tag{4.12}$$

which is the method we use here. The problem originates from having an abrupt change in material, but we introduce a method to smooth the alloy profile in Chapter 6, removing the sharp interface, in which case the boundary conditions are more easily satisfied as material properties vary smoothly. With the use of Eq. 4.4, we can calculate the matrix elements in Eq. 4.10 for each of the three cases in Eq. 4.12. The corresponding three types of matrix elements are [43, 58]

$$h^{\alpha'\alpha}_{(0)}(\mathbf{q}', \mathbf{q}) = f^{\alpha'\alpha}_{\mathsf{h}}\delta_{\mathbf{q}',\mathbf{q}} + \frac{(2\pi)^3\left(f^{\alpha'\alpha}_{\mathsf{d}} - f^{\alpha'\alpha}_{\mathsf{h}}\right)}{V}\tilde{\chi}_{\mathsf{d}}(\mathbf{q}' - \mathbf{q}) \tag{4.13}$$

$$h^{\alpha'\alpha}_i(\mathbf{q}', \mathbf{q}) = \frac{q_i' + q_i}{2}\left[f^{\alpha'\alpha}_{\mathsf{h}}\delta_{\mathbf{q}',\mathbf{q}} + \frac{(2\pi)^3\left(f^{\alpha'\alpha}_{i,\mathsf{d}} - f^{\alpha'\alpha}_{i,\mathsf{h}}\right)}{V}\tilde{\chi}_{\mathsf{d}}(\mathbf{q}' - \mathbf{q})\right] \tag{4.14}$$

$$h^{\alpha'\alpha}_{ij}(\mathbf{q}', \mathbf{q}) = \frac{1}{2}\left(q_j q_i' + q_i q_j'\right)\left[f^{\alpha'\alpha}_{\mathsf{h}}\delta_{\mathbf{q}',\mathbf{q}} + \frac{(2\pi)^3\left(f^{\alpha'\alpha}_{ij,\mathsf{d}} - f^{\alpha'\alpha}_{ij,\mathsf{h}}\right)}{V}\tilde{\chi}_{\mathsf{d}}(\mathbf{q}' - \mathbf{q})\right], \tag{4.15}$$

where the tilde over the characteristic function indicates a Fourier transform, as defined in Appendix D. An example of Eq. 4.13 would be $h^{11}_{(0)}(\mathbf{q}', \mathbf{q})$ with $f^{11}_{\mathsf{h}} = E_{\mathsf{C},\mathsf{h}}$ and $f^{11}_{\mathsf{d}} = E_{\mathsf{C},\mathsf{d}}$. An example of Eq. 4.15 would be $h^{11}_{xx}(\mathbf{q}', \mathbf{q})$ with $f^{11}_{\mathsf{h}} = A'_{2,\mathsf{h}}$ and $f^{11}_{\mathsf{d}} = A'_{2,\mathsf{d}}$.

Let us now turn to the strain contributions from Eq. 3.75. Giving a spatial dependence to each material

parameter, each bulk matrix element in Eq. 3.75 can generally be written as

$$H_{\mathsf{st}}^{\alpha'\alpha}(\mathbf{r}) = \sum_{ij=1,2,3} f_{ij}^{\alpha'\alpha}(\mathbf{r})\,\epsilon_{ij}^{\mathsf{a}}(\mathbf{r}), \tag{4.16}$$

where $f_{ij}^{\alpha'\alpha}$ are the material parameters and $\epsilon_{ij}^{\mathsf{a}}(\mathbf{r})$ is the strain in the QD superlattice (or array). For example of $H_{\mathsf{st}}^{11} = a_2(\epsilon_{xx}+\epsilon_{yy}) + a_1\epsilon_{zz}$, in which case $f_{xx}^{11} = f_{yy}^{11} = a_2$ and $f_{zz}^{11} = a_1$ and all other $f_{ij}^{\alpha'\alpha}$ are zero. In this case, we can calculate the matrix elements in Eq. 4.10 to be

$$h_{\mathsf{st}}^{\alpha'\alpha ij}(\mathbf{q}',\mathbf{q}) = \frac{(2\pi)^3}{V} f_{\mathsf{h}}^{\alpha'\alpha ij}\tilde{\epsilon}_{ij}^{\mathsf{a}}(\mathbf{q}'-\mathbf{q}) + \frac{(2\pi)^6}{V^2}\left(f_{\mathsf{d}}^{\alpha'\alpha ij} - f_{\mathsf{h}}^{\alpha'\alpha ij}\right)\left(\tilde{\chi}_{\mathsf{d}} * \tilde{\epsilon}_{ij}^{\mathsf{a}}\right)(\mathbf{q}'-\mathbf{q}), \tag{4.17}$$

where we have written the second term on the right hand side using the convolution theorem, as presented in Appendix D. Calculation of the superlattice strain $\tilde{\epsilon}_{ij}^{\mathsf{a}}$ is presented in Chapter 5.

Since III-nitride wurtzite materials have non-centrosymmetric lattices, they exhibit spontaneous polarization. Additionally, when subject to external field such as like strain, they exhibit strong piezoelectric polarization. In QDs, such polarizations can be strong enough to spatially separate electron and hole states. Calculation of these polarizations and their corresponding scalar potentials are discussed in Chapter 5. Piezoelectric effects can be coupled into the Hamiltonian via the scalar potential as [43]

$$h_{\mathsf{piezo}}^{\alpha'\alpha}(\mathbf{q}',\mathbf{q}) = -\frac{e(2\pi)^3}{V}\tilde{\varphi}^{\mathsf{a}}\left(\mathbf{q}'-\mathbf{q}\right)\delta_{\alpha',\alpha} \tag{4.18}$$

where $\tilde{\varphi}^{\mathsf{a}} = \tilde{\varphi}^{\mathsf{a,st}} + \tilde{\varphi}^{\mathsf{a,sp}}$ is the total scalar potential in the QD superlattice, with $\tilde{\varphi}^{\mathsf{a,st}}$ being the strain-induced potential and $\tilde{\varphi}^{\mathsf{a,sp}}$ the spontaneous. The delta function in Eq. 4.18 indicates that the piezoelectric potential does not mix the Bloch functions, but only shifts the main diagonal, as is expected from an electric potential.

Equations 4.13, 4.14, 4.15, 4.17 and 4.18 provide the means to calculate $h^{\alpha'\alpha}(\mathbf{q}',\mathbf{q})$ in Eq. 4.9, which must then be numerically diagonalized to obtain the energies and wavefunctions. In real space $\mathbf{k}\cdot\mathbf{p}$ approaches, space is discretized into a mesh such that each point only couples to their nearest neighbors, leading to a sparse matrix. However, in the Fourier space approach the Hamiltonian $h^{\alpha'\alpha}(\mathbf{q}',\mathbf{q})$ produces a non-sparse matrix, where size of the matrix is determined by the number of bands and wave vectors included in the calculation. The number of bands is fixed by the bulk model used and the number of plane waves $\mathbf{q}$ must be chosen sufficiently high to properly resolve the states of interest. Since the matrix is non-sparse, the memory requirements therefore scale quickly with the number of wave vectors. In Chapter 6, we use a symmetry adapted basis, which is obtained by performing a basis transformation on both the bulk basis from Eq. 3.8 and the plane wave basis in Eq. 4.5. This symmetry adapted basis block diagonalizes the Hamiltonian, requiring then only the generation and diagonalization of a single block at a time.

4.2 Optics in quantum dot $\mathbf{k}\cdot\mathbf{p}$

We now have a method to calculate the eigenstates within a QD system, but that is not sufficient to know how the system will perform for solar applications. We must now determine how the system absorbs light, which we can eventually couple into a detailed balance model to predict efficiencies. In this section, we follow the methodology of [43, 66] to calculate absorption in QD systems within the $\mathbf{k}\cdot\mathbf{p}$ framework. We assume that the intensity of the electromagnetic wave is sufficiently small as to not modify the electronic structure of QD system. We therefore treat the electromagnetic wave as a perturbation and calculate the transition rate of electrons between states, from which we are able to calculate the absorption cross section.

In classical mechanics, electromagnetic waves can be coupled into the system through the canonical coupling $\mathbf{p} \to \mathbf{p} + e\mathbf{A}$, where $\mathbf{A}$ is the vector potential and e the electric charge. In the $\mathbf{k}\cdot\mathbf{p}$ framework, this is represented by shifting the wave vector such that the perturbation Hamiltonian is given by [43, 66, 67]

$$H'_{\mathbf{k}\cdot\mathbf{p}}\left(\mathbf{k},\mathbf{A}\right) = \hat{H}_{\mathbf{k}\cdot\mathbf{p}}\left(\mathbf{k}+\frac{e}{\hbar}\mathbf{A}\right) - \hat{H}_{\mathbf{k}\cdot\mathbf{p}}\left(\mathbf{k}\right), \tag{4.19}$$

where $\hat{H}_{\mathbf{k}\cdot\mathbf{p}}$ is defined in Eq. 3.78. Given the form of Eq. 4.19, k independent terms such as spin-orbit, crystal-field and strain do not contribute to the light-matter coupling, leaving only contributions from $G_1\left(\mathbf{k}\right)$ and $G_2\left(\mathbf{k}\right)$. The vector potential is defined such that

$$\mathbf{B} = \boldsymbol{\nabla}\times\mathbf{A} \tag{4.20}$$

and

$$\mathbf{E} = -\boldsymbol{\nabla}\varphi - \frac{\partial\mathbf{A}}{\partial t}. \tag{4.21}$$

Here, $\mathbf{B}$ being the magnetic field and φ is the scalar potential. Choosing the Coulomb gauge with $\varphi\left(\mathbf{r},t\right)=0$ gives

$$\boldsymbol{\nabla}\cdot\mathbf{A} = 0. \tag{4.22}$$

Considering the leading-order contribution to be linear in $\mathbf{A}$ gives

$$H'_{\mathbf{k}\cdot\mathbf{p}}\left(\mathbf{k},\mathbf{A}\right) = \begin{bmatrix} G'\left(\mathbf{k},\mathbf{A}\right) & 0 \\ 0 & G'^{*}\left(\mathbf{k},\mathbf{A}\right) \end{bmatrix}, \tag{4.23}$$

where

$$G^{'}\left(\mathbf{k},\mathbf{A}\right)=\frac{e}{\hbar}\begin{bmatrix} G_{11}^{'}\left(\mathbf{k},\mathbf{A}\right) & iP_2A_x & iP_2A_y & iP_1A_z \\ -iP_2A_x & G_{22}^{'}\left(\mathbf{k},\mathbf{A}\right) & N_1^{'}\left(k_xA_y+A_xk_y\right) & N_2^{'}\left(k_xA_z+A_xk_z\right) \\ -iP_2A_y & N_1^{'}\left(k_yA_x+A_yk_x\right) & G_{33}^{'}\left(\mathbf{k},\mathbf{A}\right) & N_2^{'}\left(k_yA_z+A_yk_z\right) \\ -iP_1A_z & N_2^{'}\left(k_zA_x+A_zk_x\right) & N_2^{'}\left(k_zA_y+A_zk_y\right) & G_{44}^{'}\left(\mathbf{k},\mathbf{A}\right) \end{bmatrix} \tag{4.24}$$

and

$$G_{11}^{'}\left(\mathbf{k},\mathbf{A}\right)=2A_2^{'}\left(A_xk_x+A_yk_y\right)+2A_1^{'}A_zk_z$$

$$G_{22}^{'}\left(\mathbf{k},\mathbf{A}\right)=2L_1^{'}k_xA_x+2M_1k_yA_y+2M_2k_zA_z$$

$$G_{33}^{'}\left(\mathbf{k},\mathbf{A}\right)=2M_1k_xA_x+2L_1^{'}k_yA_y+2M_2k_zA_z$$

$$G_{44}^{'}\left(\mathbf{k},\mathbf{A}\right)=2M_3\left(k_xA_x+k_yA_y\right)+2L_2^{'}k_zA_z.$$

Here, $G_{ij}^{'}$ are the diagonal matrix elements and are defined for brevity.

Given this perturbation, we are now interested in calculating how electrons transition between the different states of the QD system due the incident electromagnetic wave. From Fermi's golden rule, the transition rate W_{if} between an initial state ψ_i and final state ψ_f is [43, 66]

$$W_{if}\left(E\right)=\frac{2\pi}{\hbar}\left|\langle\psi_i|\hat{H}'|\psi_f\rangle\right|^2\delta\left(E_f-E_i-E\right) \tag{4.25}$$

where E is the energy of the incident photon and the delta function represents energy conservation, giving rise to a discrete absorption spectrum. In reality, the absorption or emission spectrum of QD devices contains both homogeneous and inhomogeneous broadening. The homogeneous broadening is due to electrons having finite lifetimes in excited states. Homogeneous broadening can have multiple sources, but an important one is the size distribution of QDs within a device. Broadening can be included by exchanging the delta function by a Gaussian function,

$$\delta\left(x\right)\rightarrow g\left(x,\Delta\right)=\frac{1}{\Delta\sqrt{2\pi}}\exp\left(-\frac{x^2}{2\Delta^2}\right), \tag{4.26}$$

where Δ characterizes broadening of the linewidth. We can then obtain the absorption cross section with [43, 66]

$$\sigma_{if}=\frac{W_{if}}{\Phi}, \tag{4.27}$$

where $\Phi=\bar{n}A\varepsilon_0cE/\hbar^2$ is the total incident photon flux from the light source, $\bar{n}$ the average refractive index, A the magnitude of the vector potential, ε_0 the vacuum permittivity and c the speed of light. Inserting Eq. 4.25 into Eq.

4.27 and using Eq. 4.26 gives

$$\sigma_{ij}(E) = \frac{2\pi\hbar}{\bar{n}\varepsilon_0 cE} |M_{ij}|^2 g(E_j - E_i - E, \Delta), \tag{4.28}$$

where

$$M_{ij} = \frac{1}{A} \langle \psi_i | \hat{H}' | \psi_j \rangle \tag{4.29}$$

is a matrix element that is independent of the magnitude of $\mathbf{A}$. The Hamiltonian $\hat{H}'$ is treated using the same procedure as outlined in Sec. 4.1 for the electronic structure calculation, which involves giving material parameters a spatial dependence and replacing wave vectors by derivatives. Using this procedure and the plane wave basis shown in Eq. 4.6, we obtain [43, 66]

$$M_{ij} = V \sum_{\alpha',\alpha=1}^{8} \sum_{\mathbf{q}',\mathbf{q}} C^{i*}_{\alpha',\mathbf{q}'} C^{j}_{\alpha,\mathbf{q}} h'_{\alpha'\alpha}\left(\mathbf{q}', \mathbf{q}\right), \tag{4.30}$$

where

$$h'_{\alpha'\alpha}\left(\mathbf{q}', \mathbf{q}\right) = \frac{1}{AV} \int_V \mathrm{d}^3\mathbf{r}\, \mathrm{e}^{-i\mathbf{q}'\cdot\mathbf{r}} H'^{\alpha'\alpha}_{\mathbf{k}\cdot\mathbf{p}} \mathrm{e}^{i\mathbf{q}\cdot\mathbf{r}}. \tag{4.31}$$

Here, $H'^{\alpha'\alpha}_{\mathbf{k}\cdot\mathbf{p}}$ are the matrix elements of Eq. 4.24 and Eq. 4.31 can be calculated to obtain identical expressions as those in Eqs. 4.13 and 4.14, but with primes. Note there are no k^2 terms in $H'_{\mathbf{k}\cdot\mathbf{p}}$ and therefore no matrix elements of the form of Eq. 4.15.

In this Chapter, we have described the electronic structure of QD superlattices and how they absorb light using $\mathbf{k}\cdot\mathbf{p}$ theory, which is a single-particle theory. In reality, there are generally multiple electrons inside the QD, which can all interact. Excitons, which consist of electron and hole pairs, are multiparticle states that can play a major role in solar cells. Due to the electron hole interaction, which is attractive, we expect the electronic gap of the dot, at which it can absorb light, to be slightly decreased. In other words, the lowest electron and hole states should be pulled closer together by the electron-hole interaction, which is neglected within $\mathbf{k}\cdot\mathbf{p}$ theory. This slight shift in the QD's electronic gap could be compensated by slight changes in either the dot size or composition.

One may also question how accurate it is to assume a perfectly periodic system, when no experimental system has actual perfect periodicity. If we consider QD superlattices such that the dots are sufficiently spaced as to not interact with each other in terms of wavefunction overlap and strain, then any aperiodicities in the superlattice have no effect since the dots are effectively isolated. If the dots are sufficiently close to be coupled to one another, then we expect deviations from periodicity to have some effects. For example, slightly changing the position of a single dot would modify the local strain and wavefunction overlaps between said dot and its neighbors. For that set of dots, the energy levels will undergo small shifts, effectively shifting the electronic gap of those dots.

We therefore expect to observe some linewidth broadening due to the breaking of the periodicity, similar to what happens when there is a distribution of QD sizes. The effects of aperiodicity can therefore be included through Δ, the linewidth broadening parameter in Eq. 4.26. Note that the broadening method shown in Eq. 4.26 considers the QD parameter variations to be correlated across all dots, which is not accurately the case. Uncorrelated variation in the QD parameters could be included by considering a supercell of a few QDs, where each QD would have slightly different parameters. However, such a system would be computationally difficult to model through Fourier-space $\mathbf{k}\cdot\mathbf{p}$ theory as the supercell would be larger compared to having only a single QD per unit cell. This large supercell would then require an increased number of wave vectors to reach the same magnitude in Fourier space compared to the single QD case. More importantly, compared to a single dot containing unit cell, wave vectors of larger magnitude would be necessary to resolve the wavefunction of all the dots in the supercell.

In Chapter 7, we use the methodology presented here to calculate absorption corresponding to transitions between bound states within the QD. We then present a novel method of calculating the absorption that corresponds to transitions between QD bound states in the CB and the continuum states of the host by approximating the host states as bulk GaN states. We also use the calculated absorption cross sections to obtain absorptances, which we couple into a detailed balance model to predict power conversion efficiencies.

Chapter 5

Strain and piezoelectricity

Self-assembled or Stranski-Krastanov QDs generally consist of materials that are lattice mismatched to the host, which is the case for InGaN/GaN QD systems. This lattice mismatch leads to deformations in the crystal lattice, which can significantly impact the electronic structure of nanostructures. Typically, these lattice deformations are characterized in terms of strain, a unitless metric that describes the relative change in a solid's dimensions due to some mechanical deformation. Strain is then also typically used as an input for electronic structure calculations as to include effects from such deformations.

Strain calculations can be divided into different scales and approaches. One can use an atomic model with interatomic force fields and calculate strain by minimizing the potential energy between atoms by changing their individual positions [68–70]. This method is well suited as an input for electronic structure models such as tight-binding, which is also atomic in nature. For macroscopic models, which assume continuous media, one can use real space or Fourier-space approaches. Naturally, the best approach is based on whether the electronic structure calculation is based in real space or Fourier space. The real space approach is similar to the atomistic case, as it seeks to minimize potential energy by deforming the continuous medium [38, 39, 69]. In the Fourier-space approach, Green's functions are typically used to construct the strain [42, 71].

Since our QD $\mathbf{k}\cdot\mathbf{p}$ model, which is described in Chapter 6, is based in Fourier space, we want analytical expression of the Fourier transform of both strain and the piezoelectric potential. We therefore follow [42, 71], which are in turn based on [72, 73], to calculate strain in Fourier space. To be more specific, we calculate the strain produced by a single QD and construct the strain for a QD superlattice using superposition of the single dot strain. Importantly, this strain calculation also assumes uniform elastic constants throughout the system. This assumption was justified in [42, 71] since they considered small dots in which the lattice constants approached those of the host material, making the system more accurately described by using the host material's elastic constant for the entirety of the system. In Chapter 6, we study larger dots whose lattice constants differ from the host's and so we extend this calculation to include spatially varying elastic constants. We show that this correction is important for the case of

large InGaN/GaN QDs.

Wurtzite InGaN materials lack inversion symmetry, leading to strong piezoelectricity, which means material deformations can produce internal polarization fields. In some cases, the strain-driven piezoelectric polarization inside QDs can be strong enough to spatially separate electron and hole states, greatly impacting the QDs' optical properties. In this chapter, we calculate the strain-induced piezoelectric potential from Maxwell's equations, while assuming a spatially uniform dielectric constant, and a linear relation between strain and the piezoelectric polarization [42]. In Chapter 6, we extend the piezoelectric potential calculation to include a spatially varying dielectric constant and show that it is important in obtaining accurate results in InGaN QD systems.

5.1 Constructing strain for quantum dot arrays

In this section, we calculate the strain produced by a single dot, while assuming continuous media with uniform elastic constants (i.e. dot and host have identical elastic constants). Here, we give only an outline of the derivation, see Appendix E for full details. The method begins by calculating the displacement field using a Green's function. From the displacement field, we can calculate strain and take the Fourier transform to obtain an analytical expression, which is used in QD $\mathbf{k}\cdot\mathbf{p}$ model for the electronic structure calculation.

In this calculation, we begin by considering a host material in which we replace a volume $V_{\mathtt{d}}$ with some other material. In our case we replace GaN with InGaN, which has a larger lattice constant compared to GaN. Once the system relaxes, this leads to a compressing strain inside the dot and tensile outside the dot. During this relaxation, the lattice undergoes a transformation, displacing atoms accordingly to minimize the system's potential energy. The transformation can therefore be described by how each atom was displaced. This concept also applies for continuous media, in which case the Green's function for the displacement field, $G_{ln}(\mathbf{r})$, is defined by [42, 71]

$$\lambda_{iklm}\frac{\partial^2 G_{ln}}{\partial x_k \partial x_m} = -\delta(\mathbf{r})\,\delta_{in}, \tag{5.1}$$

where λ is the elastic modulus tensor, whose elements are the elastic constants. Here, we use Einstein's summation convention. The right-hand side of Eq. 5.1 represents a point force at position $\mathbf{r}$ in the n^{th} direction. The resulting displacement $\mathbf{u}(\mathbf{r})$ due to the QD can then be obtained by convolving the Green's function with the forces over the surface of the quantum dot[42, 71], which is written as

$$u_i(\mathbf{r}) = u_i^{(0)}(\mathbf{r}) + \int_{S_{\mathtt{d}}} G_{in}\left(\mathbf{r}-\mathbf{r}'\right)\,\mathtt{d}F_n\left(\mathbf{r}'\right), \tag{5.2}$$

where $u_i^{(0)}$ is the initial displacement before relaxation of the lattice, $\mathtt{d}F_n$ is the infinitesimal force in the n direction and $S_{\mathtt{d}}$ is the QDs' surface. For this discussion, we assume sharp material interfaces, which means we can write the

initial displacement as

$$u_i^{(0)}(\mathbf{r}) = u_i^{\mathsf{T}} \chi_{\mathsf{d}}(\mathbf{r}). \tag{5.3}$$

where u_i^{T} is the initial displacement inside the dot and $\chi_{\mathsf{d}}(\mathbf{r})$ is a characteristic function, which is 1 inside the dot and 0 outside. In chapter 6, we discuss that the main results apply also with non-sharp material interfaces. The infinitesimal force at the QD surface can be expressed in terms of the initial stress σ_{nk}^{T} via

$$\mathsf{d}F_n = \sigma_{nk}^{\mathsf{T}} \mathsf{d}S_k^{'}, \tag{5.4}$$

where $\mathsf{d}\mathbf{S}^{'}$ is an infinitesimal surface element with direction pointing outwards along the surface normal. We assume the validity of the linear relation between stress and strain, and apply Hooke's law such that

$$\sigma_{nk}^{\mathsf{T}} = \lambda_{nkpr} \epsilon_{pr}^{\mathsf{T}}, \tag{5.5}$$

where

$$\epsilon_{pr}^{\mathsf{T}} = \begin{bmatrix} \varepsilon_{\mathsf{a}} & 0 & 0 \\ 0 & \varepsilon_{\mathsf{a}} & 0 \\ 0 & 0 & \varepsilon_{\mathsf{c}} \end{bmatrix} = \varepsilon_{\mathsf{a}} \delta_{pr} + \varepsilon_{\mathsf{ca}} \delta_{p3} \delta_{r3}. \tag{5.6}$$

Here, $\epsilon_{pr}^{\mathsf{T}}$ is the initial strain inside the dot with $\varepsilon_{\mathsf{c}} = (c_{\mathsf{h}} - c_{\mathsf{d}})/c_{\mathsf{d}}$, $\varepsilon_{\mathsf{a}} = (a_{\mathsf{h}} - a_{\mathsf{d}})/a_{\mathsf{d}}$ and $\varepsilon_{\mathsf{ca}} = \varepsilon_{\mathsf{c}} - \varepsilon_{\mathsf{a}}$, such that a is the in-plane lattice constant and c is the lattice constant along the c-axis. The subscript "d" and "h" indicate dot and host material. The resulting expression for the displacement field is then

$$u_i(\mathbf{r}) = u_i^{\mathsf{T}} \chi_{\mathsf{d}}(\mathbf{r}) + \int_{S_{\mathsf{d}}} G_{in}\left(\mathbf{r} - \mathbf{r}^{'}\right) \lambda_{nkpr} \epsilon_{pr}^{\mathsf{T}} \mathsf{d}S_k^{'}. \tag{5.7}$$

Using Gauss's theorem, we transform the surface integral into a volume integral,

$$u_i(\mathbf{r}) = u_i^{\mathsf{T}}(\mathbf{r}) \chi_{\mathsf{d}}(\mathbf{r}) + \int_{V_{\mathsf{d}}} \frac{\partial G_{in}\left(\mathbf{r} - \mathbf{r}^{'}\right)}{\partial x_k} \lambda_{nkpr} \epsilon_{pr}^{\mathsf{T}} \mathsf{d}V^{'}. \tag{5.8}$$

The displacement and strain fields are related by

$$\epsilon_{ij}(\mathbf{r}) = \frac{1}{2}\left(\frac{\partial u_i}{\partial x_j} + \frac{\partial u_j}{\partial x_i}\right). \tag{5.9}$$

Using the Fourier transform, we obtain [42]

$$\tilde{\epsilon}_{ij}(\mathbf{q}) = \tilde{\chi}_{\mathsf{d}}(\mathbf{q}) \left\{ \varepsilon_{\mathsf{a}} \delta_{ij} + \varepsilon_{\mathsf{ca}} \delta_{i3} \delta_{j3} + \frac{RP(\mathbf{q}) - SI(\mathbf{q})}{I(\mathbf{q}) Q(\mathbf{q}) - F(\mathbf{q}) P(\mathbf{q})} q_i q_j + \frac{SF(\mathbf{q}) - RQ(\mathbf{q})}{I(\mathbf{q}) Q(\mathbf{q}) - F(\mathbf{q}) P(\mathbf{q})} q_3 \frac{q_i \delta_{j3} + q_j \delta_{i3}}{2} \right\}, \tag{5.10}$$

where

$$
\begin{aligned}
P(\mathbf{q}) &\equiv C_{44}q^2 + (C_{33} - C_{13} - 2C_{44})\, q_3^2 \\
I(\mathbf{q}) &\equiv (C_{13} + C_{44})\, q_3^2 \\
Q(\mathbf{q}) &\equiv (C_{33} - 2C_{13} - 4C_{44} + C_{11})\, q_3^2 + (C_{13} + 2C_{44} - C_{11})\, q^2 \\
F(\mathbf{q}) &\equiv (C_{13} + 2C_{44} - C_{11})\, q_3^2 + C_{11}q^2 \\
R &= (3\alpha + 2\beta + \kappa)\, \varepsilon_a + (\alpha + \kappa)\, \varepsilon_{ca} \\
S &= (\gamma + 3\kappa + 4\rho)\, \varepsilon_a + (2\beta + \gamma + \kappa + 4\rho)\, \varepsilon_{ca} \\
\alpha &= C_{12} \\
\beta &= \frac{1}{2}(C_{11} - C_{12}) \\
\gamma &= C_{33} - 2C_{13} - 4C_{44} + C_{11} \\
\kappa &= C_{13} - C_{12} \\
\rho &= C_{44} + \frac{C_{12} - C_{11}}{2}.
\end{aligned}
\tag{5.11}
$$

Here, the tilde indicates a Fourier transform and analytical expressions for $\tilde{\chi}(\mathbf{q})$. The constants C_{ij} in Eq. 5.11 are the nonzero elements of the elastic constants tensor λ_{iklm}. The characteristic function in Eq. 5.10 contains information regarding the dot geometry, while the bracketed term contains information of the crystal structure and materials that make up the system.

Equation 5.10 represents the strain produced by a single dot in a host material such that they have identical elastic constants. References [42, 71] consider small QDs whose lattice constants approach those of the host material due to strain. In their case, it was shown that it is more accurate to use the host material elastic constants for the entire system. In Chapter 6, we consider larger dots whose elastic constants significantly differ from those of the host material. We therefore use an extended method presented by [42] which does include spatially varying elastic constants. This method was originally presented in the Appendices of [42], although they did not use it themselves. We conclude in Chapter 6 that spatially varying elastic constants are important in describing both strain and the electronic structure of large InGaN QDs.

The strain produced by a 3D array of dots can be obtained the superposition of single dot strains

$$
\epsilon_{ij}^{\mathsf{a}}(\mathbf{r}) = \sum_{\mathbf{R}} \epsilon_{ij}(\mathbf{r} + \mathbf{R}). \tag{5.12}
$$

The superscript "a" indicates that it is for an array of dots and the set of vectors $\mathbf{R}$ are linear combinations of the QD superlattice basis vectors. It can then be shown that the strain produced the array of QDs is [42, 71]

$$
\epsilon_{ij}^{\mathsf{a}}(\mathbf{r}) = \frac{(2\pi)^3}{V} \sum_{\mathbf{q}} \tilde{\epsilon}_{ij}(\mathbf{q})\, e^{i\mathbf{q}\cdot\mathbf{r}} \tag{5.13}
$$

where $\mathbf{q}$ are the reciprocal wave vectors of the QD superlattice and V is the volume of the superlattice unit cell.

5.2 Piezoelectric polarization fields

The strain calculated in the previous section represents a deformation of the lattice. Given that InGaN materials are strongly piezoelectric, this deformation can result in a polarization existing within the nanostructures. In this section, we first cover the general relationship between strain and the induced polarization. We then calculate the piezoelectric polarization inside a QD superlattice, which is in turn used in Sect. 5.3 to calculate the piezoelectric potential.

Let's first describe the relationship between strain and the piezoelectric polarization. Here, we take the leading order contribution to be linear, giving

$$P_i^{\mathsf{st}} = \sum_{j,k=1}^{3} e_{ijk}\epsilon_{jk}, \tag{5.14}$$

where $\mathbf{P}^{\mathsf{st}}$ is the strain induced polarization and e_{ijk} are called the piezoelectric constants. Nonlinearity between strain and polarization in III-V nitride materials has been investigated and shown to be important in matching experimental results [74, 75], but we limit ourselves to a linear regime for simplicity. Since strain is a symmetric tensor ($\epsilon_{ij} = \epsilon_{ji}$) and has only 6 independent components, we can simplify the mathematics by considering only the ϵ_{11}, ϵ_{22}, ϵ_{33}, ϵ_{23}, ϵ_{13} and ϵ_{12} strain components. We can do this by writing

$$\begin{aligned} P_i^{\mathsf{st}} &= \sum_{j=1}^{3} e_{ijj}\epsilon_{jj} + \sum_{\substack{i,j=1 \\ i\neq j}}^{3} e_{ijk}\epsilon_{jk} \\ &= \sum_{j=1}^{3} e_{ijj}\epsilon_{jj} + \sum_{\substack{i,j=1 \\ j>i}}^{3} 2e_{ijk}\epsilon_{jk}. \end{aligned} \tag{5.15}$$

In matrix form, this is written as

$$\begin{bmatrix} P_1^{\mathsf{st}} \\ P_2^{\mathsf{st}} \\ P_3^{\mathsf{st}} \end{bmatrix} = \begin{bmatrix} e_{111} & e_{122} & e_{133} & 2e_{123} & 2e_{113} & 2e_{112} \\ e_{211} & e_{222} & e_{233} & 2e_{223} & 2e_{213} & 2e_{212} \\ e_{311} & e_{322} & e_{333} & 2e_{323} & 2e_{313} & 2e_{312} \end{bmatrix} \begin{bmatrix} \epsilon_{11} \\ \epsilon_{22} \\ \epsilon_{33} \\ \epsilon_{23} \\ \epsilon_{13} \\ \epsilon_{12} \end{bmatrix}. \tag{5.16}$$

The constants e_{ijk} are material dependent quantities. For the case of wurtzite materials, this reduces to [43, 76]

$$\begin{bmatrix} P_1^{\mathsf{st}} \\ P_2^{\mathsf{st}} \\ P_3^{\mathsf{st}} \end{bmatrix} = \begin{bmatrix} 0 & 0 & 0 & 0 & 2e_{113} & 0 \\ 0 & 0 & 0 & 2e_{223} & 0 & 0 \\ e_{311} & e_{322} & e_{333} & 0 & 0 & 0 \end{bmatrix} \begin{bmatrix} \epsilon_{11} \\ \epsilon_{22} \\ \epsilon_{33} \\ \epsilon_{23} \\ \epsilon_{13} \\ \epsilon_{12} \end{bmatrix}, \tag{5.17}$$

with $e_{113} = e_{223}$ and $e_{311} = e_{322}$. Carrying out the matrix multiplication gives

$$\begin{bmatrix} P_1^{\mathsf{st}} \\ P_2^{\mathsf{st}} \\ P_3^{\mathsf{st}} \end{bmatrix} = \begin{bmatrix} 2e_{15}\epsilon_{13} \\ 2e_{15}\epsilon_{23} \\ e_{31}\left(\epsilon_{11}+\epsilon_{22}\right) + e_{33}\epsilon_{33} \end{bmatrix}, \tag{5.18}$$

where $e_{15} \equiv e_{113} = e_{223}$, $e_{31} \equiv e_{311} = e_{322}$ and $e_{33} \equiv e_{333}$ [76].

In the case of a QD superlattice, the value of the piezoelectric constants depends on the local indium fraction. In this case, we write the components of the strain-induced polarization as

$$P_i^{\mathsf{st,a}}(\mathbf{r}) = \sum_j f_{ij}(\mathbf{r})\,\epsilon_j^{\mathsf{a}}(\mathbf{r}), \tag{5.19}$$

where

$$f_{ij}(\mathbf{r}) = f_{ij}^{\mathsf{h}} + \left(f_{ij}^{\mathsf{d}} - f_{ij}^{\mathsf{h}}\right)\chi_{\mathsf{d}}(\mathbf{r}), \tag{5.20}$$

Here, $f_{ij}(\mathbf{r})$ contain the piezoelectric constants whose values depend on position (e.g. $f_{11}(\mathbf{r}) = 2e_{15}(\mathbf{r})$). f_{ij}^{h} is the value in the host material, while f_{ij}^{d} is for inside the dot. The case of smoothly varying alloy fraction is treated in Chapter 6. By taking the Fourier transform, we obtain

$$\tilde{P}_i^{\mathsf{st,a}}(\mathbf{q}) = \sum_j \left[f_{ij}^{\mathsf{h}}\tilde{\epsilon}_j(\mathbf{q}) + \frac{(2\pi)^3\left(f_{ij}^{\mathsf{d}} - f_{ij}^{\mathsf{h}}\right)}{V}\left(\tilde{\chi}_{\mathsf{d}} * \tilde{\epsilon}_j\right)(\mathbf{q}) \right], \tag{5.21}$$

where we have used the convolution theorem $\mathscr{F}\{f(\mathbf{r})\,g(\mathbf{r})\}(\mathbf{q}) = \frac{(2\pi)^3}{V}\left(\tilde{f} * \tilde{g}\right)(\mathbf{q})$ to evaluate the second term. Using Eqs. 5.18 and 5.21, we may write the Fourier transform of the polarization field as:

$$\begin{bmatrix} \tilde{P}_1^{\mathsf{st,a}} \\ \tilde{P}_2^{\mathsf{st,a}} \\ \tilde{P}_3^{\mathsf{st,a}} \end{bmatrix} = \begin{bmatrix} 2e_{15}^{\mathsf{h}}\tilde{\epsilon}_{13}(\mathbf{q}) + \frac{2(2\pi)^3\left(e_{15}^{\mathsf{d}} - e_{15}^{\mathsf{h}}\right)}{V}\left(\tilde{\chi}_d * \tilde{\epsilon}_{13}\right)_e(\mathbf{q}) \\ 2e_{15}^{\mathsf{h}}\tilde{\epsilon}_{23}(\mathbf{q}) + \frac{2(2\pi)^3\left(e_{15}^{\mathsf{d}} - e_{15}^{\mathsf{h}}\right)}{V}\left(\tilde{\chi}_d * \tilde{\epsilon}_{23}\right)_e(\mathbf{q}) \\ e_{31}^{\mathsf{h}}\left[\tilde{\epsilon}_{11}(\mathbf{q}) + \tilde{\epsilon}_{22}(\mathbf{q})\right] + \frac{(2\pi)^3\left(e_{31}^{\mathsf{d}} - e_{31}^{\mathsf{h}}\right)}{V}\left[\tilde{\chi}_{\mathsf{d}} * \left(\tilde{\epsilon}_{11} + \tilde{\epsilon}_{22}\right)\right](\mathbf{q}) + e_{33}^{\mathsf{h}}\tilde{\epsilon}_{33}(\mathbf{q}) + \frac{(2\pi)^3\left(e_{33}^{\mathsf{d}} - e_{33}^{\mathsf{h}}\right)}{V}\left(\tilde{\chi}_{\mathsf{d}} * \tilde{\epsilon}_{33}\right)(\mathbf{q}) \end{bmatrix}. \tag{5.22}$$

There also exists a spontaneous polarization in bulk InGaN materials, which is independent of any deformation. The spontaneous polarization is uniform throughout the material and points along the c-axis;

$$\mathbf{P}^{\mathsf{sp}}(\mathbf{r}) = \begin{bmatrix} 0 \\ 0 \\ P^{\mathsf{sp}} \end{bmatrix}.$$

In the case of QDs, we also give P^{sp} a spatial dependence and proceed in the same way as for the strain-driven polarization to obtain

$$\tilde{P}_3^{\mathsf{sp,a}}(\mathbf{q}) = P^{\mathsf{sp,h}}\delta_{\mathbf{q},\mathbf{0}} + \left(P^{\mathsf{sp,d}} - P^{\mathsf{sp,h}}\right)\tilde{\chi}(\mathbf{q})$$

Material parameters for these calculations may be found in Appendix A.

5.3 Piezoelectric potential

Let us now turn to calculating the piezoelectric potential that corresponds to the strain-induced and spontaneous polarization. We follow the derivation from [42], which assumes uniform dielectric constants. Similar to strain, the goal is to have an analytical expression for the Fourier transform of the potential so we can then use it in the QD $\mathbf{k}\cdot\mathbf{p}$ model. For the GaN/AlN systems considered in [42], the uniform elastic constants were a good approximation due to the dielectric constant being similar for both materials being considered. However, this is not the case for InGaN systems. In Chapter 6, we show how to include smoothly varying dielectric constants using similar calculations and compare to results from assuming a uniform dielectric constant of the host material. We show in Chapter 6 that it is important to consider the full spatial dependence of the dielectric constant for accurate results.

Let us consider a single QD in a host material. The displacement field $\mathbf{D}(\mathbf{r})$ can be written

$$\mathbf{D}(\mathbf{r}) = \varepsilon_0\mathbf{E}(\mathbf{r}) + \mathbf{P}_{\mathsf{tot}}(\mathbf{r}), \tag{5.23}$$

where $\mathbf{E}(\mathbf{r})$ is the electric field, ε_0 is the vacuum permittivity, and $\mathbf{P}_{\mathsf{tot}}$ is the total polarization. The total polarization consists of contributions from bound charges, strain and spontaneous polarizations, leading to

$$\mathbf{P}_{\mathsf{tot}}(\mathbf{r}) = \mathbf{P}_{\mathsf{bnd}}(\mathbf{r}) + \mathbf{P}_{\mathsf{st}}(\mathbf{r}) + \mathbf{P}_{\mathsf{sp}}(\mathbf{r}). \tag{5.24}$$

Here, we assume no free charge screening, and that $\mathbf{P}_{\mathsf{bnd}}$ is linear with the electric field and incorporated into ε as usual. In this case, we can write

$$\mathbf{D}(\mathbf{r}) = \varepsilon\mathbf{E}(\mathbf{r}) + \mathbf{P}(\mathbf{r}), \tag{5.25}$$

where

$$\mathbf{P}(\mathbf{r}) = \mathbf{P}_{\mathsf{st}}(\mathbf{r}) + \mathbf{P}_{\mathsf{sp}}(\mathbf{r}). \tag{5.26}$$

$\mathbf{P}(\mathbf{r})$ is therefore the residual polarization after electric-field induced bound charge has been included in ε. Taking the divergence of Eq. 5.25 leads to

$$\boldsymbol{\nabla}\cdot\mathbf{D} = \varepsilon\boldsymbol{\nabla}\cdot\mathbf{E} + \boldsymbol{\nabla}\cdot\mathbf{P} = \rho_{\mathsf{f}},$$

where ρ_{f} are the free charges. We assume there are no free charges within the system, giving

$$\varepsilon\boldsymbol{\nabla}\cdot\mathbf{E} + \boldsymbol{\nabla}\cdot\mathbf{P} = 0. \tag{5.27}$$

Using Einstein's summation convention and rewriting gives

$$\partial_m E_m = -\frac{1}{\varepsilon}\partial_n P_n. \tag{5.28}$$

Taking the Fourier transform of Eq. 5.28 and using $\mathscr{F}\{\partial_m f(\mathbf{r})\}(\mathbf{q}) = iq_m\tilde{f}(\mathbf{q})$, gives

$$q_m\tilde{E}_m = -\frac{1}{\varepsilon}q_n\tilde{P}_n. \tag{5.29}$$

We can relate the electric field to the scalar potential $\varphi(\mathbf{r})$ by

$$E_m = -\partial_m\varphi. \tag{5.30}$$

We can take the Fourier transform of Eq. 5.30 and use the property $\mathcal{F}\left\{\frac{\partial g}{\partial x_i}\right\} = iq_i\mathcal{F}\{g\}$ to obtain

$$\tilde{E}_m = -iq_m\tilde{\varphi} \tag{5.31}$$

Inserting Eq. 5.31 into Eq. 5.29 leads to

$$\tilde{\varphi} = -i\frac{1}{\varepsilon}\frac{q_n\tilde{P}_n}{q^2}. \tag{5.32}$$

Since this theory is linear in $\mathbf{P}$, one can obtain the piezoelectric potential for the array by superposition, as was done for strain with Eq. 5.12 and 5.13, and obtain [42]

$$\tilde{\varphi}^{\mathsf{a}} = -i\frac{1}{\varepsilon}\frac{q_n\tilde{P}^{\mathsf{a}}_n}{q^2}, \tag{5.33}$$

where the superlattice polarization field is given by Eq. 5.22. Similar to the case of strain and the elastic constants, Eq. 5.33 assumes a spatially uniform dielectric constant, which was justified for the materials considered in [42]. InGaN and GaN can have considerably different dielectric constants, depending on the indium fraction. For this reason, we extend this method in Chapter 6 to include a spatially varying dielectric constant and show that this correction is important in accurately describing the piezoelectric potential and electronic structure of InGaN QDs.

Chapter 6

Efficient Fourier space quantum dot $\mathbf{k} \cdot \mathbf{p}$ for wurtzite systems including smooth alloy profile and spatially varying elastic and dielectric constants

Reproduced from Journal of Applied Physics 129, 224301 (2021), with the permission of JAP [77]

Luc Robichaud and Jacob J. Krich

Original Abstract: We present methods to calculate the electronic structure of wurtzite quantum dot systems with continuous alloy profiles within Fourier-space-based $\mathbf{k} \cdot \mathbf{p}$ theory. We incorporate spatially varying elastic and dielectric constants in strain and piezoelectric potential calculations. A method to incorporate smooth alloy profiles in all aspects of the calculations is presented. We demonstrate our methodology for the case of a 1-dimensional InGaN quantum dot array and show the importance of including these spatially varying parameters in the modeling of devices. We demonstrate that the convergence of the lowest bound state energies is for good approximation determined by the largest wave vector used in constructing the states. We also present a novel approach of coupling strain into the $\mathbf{k} \cdot \mathbf{p}$ Hamiltonian, greatly reducing the computational cost of generating the Hamiltonian.

Notes:

- Since the publication of this paper, we have learned there was sign error in the e_{15} parameters used to calculate the piezoelectric potential. This error is widespread in literature, which includes the references used for said parameters. This sign error is discussed in detail in the erratum [75] to the paper [78] and also confirmed in [79]. This sign error was corrected for the calculations of Chapter 7.

- Original publication's introduction did not mention what type of machine calculations were performed on.
- Figure 6.1 and its mention in introduction were not included the original publication.
- Equations 6.2, 6.3, 6.4 and 6.7 and the discussions surrounding them were not included in the original publication.
- Figure 6.7 and the paragraph that refers to it were not included in the original publication.
- A typo was found in what is now Eq. A.11. The expression for the Kane parameter P_2^2 was missing a "3" in the denominator, which has been corrected in this thesis. This was merely a manuscript typo and does not impact results.
- Another typo has been fixed in the text of what is now Appendix D. It originally stated "$-m_j \leq i_j < m_j$" just above Eq. D.9, which has been corrected to "$-m_j \leq i_j \leq m_j$".

6.1 Introduction

Given their large range of bandgaps, from 0.78 eV to 3.51 eV, InGaN materials have attracted attention in applications such as LEDs, single-photon emitters, water splitting and solar cells [1, 7, 17–19]. For any application, device performance depends on having an electronic structure well tuned to its target application. Since the electronic structure of quantum dots (QDs) can be dramatically changed by varying their size and composition, they can be quite attractive for applications. InGaN QD structures grown by molecular beam epitaxy (MBE) have significant In diffusion [17], leading to a smoothly varying alloy profile without a sharp material interface. This indium diffusion results in a material whose elastic and electrical parameters vary with the local alloying fraction. Quantum dots with intentionally graded indium fractions have also been of interest [80]. Given the electronic structure's sensitivity to composition, accurate alloy profiles are crucial for accurate modeling.

Tight binding (TB) and $\mathbf{k}\cdot\mathbf{p}$ theory are standard approaches for calculating single-particle electronic structures for bulk materials and nanostructures. The table in Fig. 6.1 shows a comparison of the two methods when applied to QDs and encapsulates the essence of this introduction section. Both approaches rely on elastic, dielectric, and electronic parameters, which vary spatially in QD structures due to the changing alloy content. Essentially all methods calculate the continuously varying local strain field and its impact on the electronic structure through deformation potential and piezoelectric couplings. Frequently, calculations assume sharp material interfaces and uniform alloy content in the dot and host regions; they additionally assume that the elastic and dielectric constants are spatially uniform [42, 69]. Continuous spatial dependence of these material parameters is readily included in real-space methods, including both TB and $\mathbf{k}\cdot\mathbf{p}$. Strain, even with spatially varying elastic constants, can be calculated using real-space finite element methods for continuum elastic models [38, 39, 69] and with valence force fields in atomistic models [68–70]. Smooth variation of the alloy fraction can also be included [39]. However, both TB and real-space $\mathbf{k}\cdot\mathbf{p}$ have important limitations. Tight binding methods can be accurate but become expensive when considering systems with a large number of atoms [81], though linearly scaling methods extend their reach for an increasing number of systems [82]. The $\mathbf{k}\cdot\mathbf{p}$ method is not atomistic and gives a good balance between accuracy and computational requirements for mid-to-large dots [40]. Its real-space implementations using the finite difference method [38, 39] can be successful, but they can suffer from spurious mid-gap states arising from finite difference formulae effectively sampling bulk states at large wave vectors where $\mathbf{k}\cdot\mathbf{p}$ breaks down, especially at high alloy fractions [83, 84].

Fourier space approaches to $\mathbf{k}\cdot\mathbf{p}$ have been widely used with good success in modeling the electronic structure of QDs [41, 42, 58, 59, 85–88]. They provide an excellent compromise between computational cost and accuracy, allowing consideration of nanoscale structures beyond the scale of TB. Fourier space $\mathbf{k}\cdot\mathbf{p}$ methods give direct control of wave-vector sampling, making it easy to reject the spurious states [42, 58].

A hybrid approach using real-space parametrization and fast-Fourier-transform-based strain and Hamiltonian calculations allows rapid determination of band-edge energies in nanostructures, including piezoelectric potentials

and smoothly varying alloy profiles [80, 87, 88]. Each eigenstate must be found independently, making this approach particularly good when interested in the lowest electron and hole states or in small dots that only contain a few bound states. The traditional Fourier space approach, as taken by [41, 42, 58, 59, 85, 86], produces a non-sparse Hamiltonian, which is diagonalized to obtain a full eigenvalue spectrum, making it useful when interested in properties such as optical absorption. References [41, 58, 59, 85, 86] reduced the computational cost of this approach by using symmetry adapted bases that block diagonalize the Hamiltonian [41, 43, 59]. This latter Fourier space based $\mathbf{k} \cdot \mathbf{p}$ method has only been used with sharp material interfaces, spatially uniform elastic and dielectric constants, and spatially uniform dot and host alloy fractions. References [42, 43, 71] used a continuum elastic Green's function method for calculating strain. These works assumed spatially uniform elastic and dielectric constants for both the host and dot materials, which was justified for the sizes of their InAs/GaAs and GaN/AlN QD systems but would not be correct for larger dots. Reference [42] presented a method to include different host and dot material elastic constants but did not use it.

In isolated QDs, it is computationally challenging to calculate strain effects since strain generally decays more slowly than bound state wavefunctions. The unit cell must then be chosen large enough to resolve the strain decay, increasing the number of plane waves that must be calculated to resolve the electronic structure, at considerable computational expense. References [59, 78] presented a more efficient approach that uses two different unit cells; one for the electronic structure and one for strain. This method allows for the modeling of the electronic structure and strain, but introduces some complexity in calculating the Hamiltonian, which requires the calculation of multiple composed convolutions on different Fourier space meshes. These convolutions can be computationally costly depending on the sizes of meshes needed for convergence.

In this article, we show methods for and the importance of including two different sources of spatial variation in Fourier space $\mathbf{k} \cdot \mathbf{p}$ calculations for wurtzite InGaN systems: first, spatially varying elastic and dielectric constants and second, smooth alloy profiles, as are found in experimental devices. Our approach efficiently includes smooth alloy profiles in the strain, piezoelectric potential and electronic structure calculations. Smooth indium profiles both increases the accuracy of the simulations for simulating experimental devices and decreases their computational cost by removing the abrupt interfaces that otherwise require large numbers of plane waves to obtain convergence. The spatial variations of elastic and dielectric constants affect the calculation of strain and piezoelectric potentials, and we adapt the calculations presented by Ref. [42] to include a spatially varying dielectric constant. We also present a method to improve the efficiency of calculating the strain in using the two-unit-cell method for isolated QDs. By fixing the strain unit cell to be commensurate with the electronic unit cell, we present an approach that reduces the number of needed convolutions, significantly reducing the computational cost.

We demonstrate our methodology by calculating the electronic structure for a 1D array of InGaN QDs, modeling devices grown as LEDs and used for water splitting [17, 19]. In this example, we show the importance of the inclusion of spatially varying elastic and dielectric constants and smooth indium profiles for accurate electronic structures.

We also show that the most important criterion for convergence of the lowest QD electron and hole energies is the maximum wave vector included in the Fourier space sampling, which can be increased with low computational cost by using a small unit cell.

Section 6.2 contains strain and piezoelectric potential calculations using spatially varying elastic and dielectric parameters. Section 6.3 presents the $\mathbf{k} \cdot \mathbf{p}$ model used for electronic structure calculations and our novel approach to efficiently include strain through choices of unit cells. Section 6.4 introduces a method to use smooth indium profiles in all aspects of our calculations. Section 6.5 demonstrates our entire methodology for the case of a 1D QD array, such as QDs grown inside of nanowires [17].

All calculations done in this work were performed on a desktop machine with a Intel Core i5-3470 cpu@3.20Ghz processor and 24GB of RAM. All code was written in-house using Matlab R2017b.

	Tight-Binding	$\mathbf{k} \cdot \mathbf{p}$	
		Real space	Fourier space
Small dots	✓	✓	✓
Large dots	Many atoms	✓	✓
High alloy	✓	Midgap states	✓
Smooth alloy profiles	✓	✓	Developed here
Spatially varying elastic and dielectric constants	✓	✓	Developed here

Figure 6.1: Comparison of the tight-binding and $\mathbf{k} \cdot \mathbf{p}$ methods, where the latter is divided into real space and Fourier space approaches. In this work, we consider large dots and want the flexibility of considering high indium fractions. Fourier-space based $\mathbf{k} \cdot \mathbf{p}$ is the best approach for us, but lacks methods to include spatially varying alloy fractions and likewise for elastic and dielectric constants. Our work in this Chapter provides the necessary methods to include these effects.

6.2 Spatially varying elastic and piezoelectric constants

We begin by considering QD heterostructures with abrupt changes in alloy fraction. Alloying the host material changes the local lattice constants, leading to a lattice mismatch at the host and dot material boundary. This lattice mismatch is a source of strain throughout the QD system, affecting the electronic states of the system. For example, InN has a larger lattice constant than GaN, so alloying GaN with indium to form a QD produces strain in and near the QD. The propagation of that strain is determined by the elastic constant, which itself also varies with alloy fraction. Additionally, strain can generate strong piezoelectric potentials in materials such as III-nitrides. The piezoelectric potential in III-nitrides is particularly important along the c-axis and can be strong enough to spatially separate electron and hole states through the quantum-confined Stark effect [89].

In prior Fourier-space-based work, elastic and dielectric constants are largely assumed to be spatially uniform in Fourier-based calculations of strain and the piezoelectric potential. Reference [42] presented a method to include

differing host and dot elastic constants but did not use it in their calculations. They argued that the system's elastic constant largely depends on the nearest neighbor lattice spacing, which is strongly modified inside small dots from bulk values. They therefore used the spatially uniform elastic constant of the host material. In our case, we consider larger dots in which the lattice constant in the center of the dots can be significantly different from that in the barrier material, which implies that the local elastic constants should also be different from those in the barrier material. Having the local elasticity depend on local strain would make a computationally challenging nonlinear problem. Instead, we implement the method presented by [42] to include differing elastic constants, using the bulk elastic constants of alloys at each location. We compare those results to those obtained from using spatially uniform elastic constants, to highlight the differences in strain-induced dot energy levels. For the piezoelectric potential, we use a procedure similar to Ref. [42], but we also include spatially varying dielectric constants. The strain field and piezoelectric potential are coupled into a $\mathbf{k}\cdot\mathbf{p}$ model, presented in Section 6.3, for electronic structure calculations.

6.2.1 Quantum dot system

We consider a superlattice of wurtzite QDs embedded in a bulk host material, as shown in Fig. 6.2(a). InGaN QDs such as those described in Ref. [17] have a lens-like shape and do not have a sharply defined boundary. We approximate these QDs as being either cylindrical or hexagonal prisms. These choices of dot geometries simplify calculations, as described in Sec. 6.2.2, and preserve the C_{6v} symmetry of the material, which we take advantage of in Section 6.3 for electronic structure calculations. Hexagonal periodic boundary conditions are used to also preserve the material's C_{6v} symmetry. For single-dot calculations, the superlattice unit cell must be large enough that the choice of cell size does not affect results. For actual QD arrays, we consider only hexagonal superlattices in the plane.

In this periodic system, the real space QD superlattice is defined by the set of lattice vectors $\mathbf{L}_i$, as shown in Fig. 6.2(a). We denote the real space unit cell by Ω_e, its volume V_e, and the reciprocal-space unit cell by Ω_e^{-1}. The index "e" indicates that these quantities relate to the electronic cell, as opposed to the strain unit cell, which is introduced in Section 6.2.2. Imposing periodic conditions in real space implies a discrete reciprocal space with wave vectors

$$\mathbf{q} = i_1\mathbf{b}_1 + i_2\mathbf{b}_2 + i_3\mathbf{b}_3 \qquad i_1, i_2, i_3 \in \mathbb{Z} \tag{6.1}$$

where $\mathbf{b}_i$ are the reciprocal basis vectors, similar to [43]. Due to the symmetry of the system, we have $L_1 = L_2$, which we define as L_{12}. In our reciprocal-space calculations, we sample on sets of the wave vectors $\mathbf{q} \in \Omega_\mathsf{e}^{-1}$. We define m_{12} and m_3 such that $i_1, i_2 = \{-m_{12}, \cdots, 0, \cdots, m_{12}\}$ and $i_3 = \{-m_3, \cdots, 0, \cdots, m_3\}$. This sampling produces a hexagonal mesh of size $N = N_1N_2N_3$ where $N_i = 2m_i + 1$. To obtain a C_6 symmetric mesh, we remove points such that $|q_x| > m_{12}\frac{2\pi}{L_1}$, leaving a mesh whose size we denote by N_e.

By choosing the unit cell dimensions L_i large enough, it is possible to remove electronic coupling between

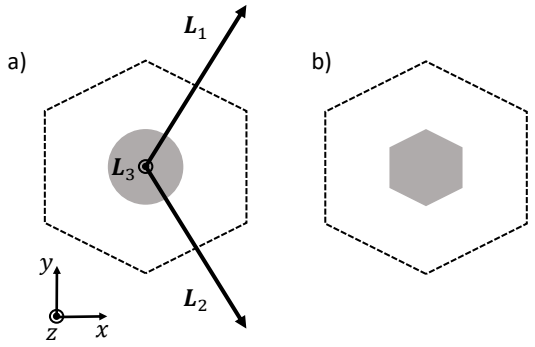

Figure 6.2: (a) Unit cell of the cylindrical QD superlattice and its basis vectors. Dashed lines show the unit cell boundaries of the QD superlattice. White regions are the host material and grey regions are the QDs. (b) Hexagonal prism QD.

neighboring dots. This flexibility allows us to model 3D, 2D and 1D arrays of coupled dots. The isolated dot case can also be obtained by choosing both L_{12} and L_3 sufficiently large. Section 6.2.2 presents a method that also uncouples dots in terms of strain, which is based on calculating strain and the electronic structure using different unit cells.

We illustrate the methods presented in this manuscript by modeling a QD system inspired by Ref. [17]. That system consists of InGaN dots grown in GaN nanowires. We approximate this system as an infinite 1D QD array, by choosing L_3 to match the measured dot-dot spacing and L_{12} large enough to avoid dot-dot coupling, but we do not consider the nanowire itself and instead embed the dots in bulk GaN. We choose the dot indium alloy fraction, radius and height based on the experimental device. System parameters are listed in Table 6.1, and material parameters are in Appendix A. In some instances, wurtzite QD possess a clear hexagonal geometry [90]. Therefore, we consider both cylindrical and hexagonal prism QDs, as shown in Fig. 6.2(b). The hexagonal dots have dimensions chosen to give an area of πR^2, preserving the volume of the cylindrical dots. In all of the cases studied, there is only a small difference between the circular and hexagonal dots, and we show the circular ones in most results. We illustrate the small differences in Section 6.5. All results are for the cylindrical case unless stated otherwise.

Table 6.1: Default quantum dot superlattice parameters used unless specified otherwise.

Parameter	Value
X_0	0.45
h	40 $\mathring{A}$
R	200 $\mathring{A}$
L_{12}	500 $\mathring{A}$
L_3	70 $\mathring{A}$
m_{12}	10
m_3	4
n_{12}	6
n_3	1
$\boldsymbol{\delta}$	$[1.5, 1.5, 2.5]$ $\mathring{A}$

6.2.2 Strain

In this section, we present how we calculate strain with elastic constants that depend on alloy fraction for 3D, 2D and 1D QD superlattices and isolated dots. Our method follows from Refs. [42, 59]. We calculate the strain produced by a single isolated dot and construct the QD superlattice strain by linear superposition.

The calculated strain is to be coupled into the electronic structure calculations. However, strain decays considerably slower than bound electronic wavefunctions. In the case of isolated dots, the unit cell must be large enough to accommodate the strain decay. Choosing a unit cell large enough to capture the strain decay reduces the maximum wave vector attainable when using a fixed number of plane waves. As we demonstrate in Section 6.5, accurately describing the electronic states requires using sufficiently large wave vectors, and thus, a large unit cell requires a large number of plane waves. Following Ref. [59], we consider that the electronic model and strain model each have their own real space unit cells. This additional degree of freedom allows accurate and computationally efficient determination of both electronic structure of rapidly decaying confined QD states and longer-range strain effects in isolated dots. In the case of a QD superlattice, different real-space electronic and strain unit cells are not required.

In prior work, lattice-mismatch-driven strain has been calculated for a single dot using a continuum theory with a Green's function approach while assuming spatially uniform elastic constants [42, 71, 91]. We briefly present the method to include spatially varying elastic constants from Appendix A of [42], correcting typos in Eqs. A7 and A8. We show how the spatially varying elastic constants modify strain and how this modified strain changes the piezoelectric potential in Section 6.2.3. We show that the elastic constant correction is necessary to obtain accurate strain and piezoelectric potentials.

In the case of a single QD with sharp material interfaces and elastic constants $\lambda_{ijmn}(\mathbf{r})$ that differ between dot and host materials, we can write

$$\lambda_{ijmn}(\mathbf{r}) = \lambda^{\mathsf{d}}_{ijmn} + \lambda^{\mathsf{h}}_{ijmn}\left[1 - \chi_{\mathsf{d}}(\mathbf{r})\right], \tag{6.2}$$

where $\lambda^{\mathsf{h}}_{ijmn}$ and $\lambda^{\mathsf{d}}_{ijmn}$ are the host and dot's elastic constants, respectively. Assuming spatially varying elastic constants, the Green's tensor $\tilde{G}_{in}$ for the displacement field in an infinite anisotropic elastic medium must satisfy

$$\frac{\partial}{\partial x_k}\lambda_{iklm}(\mathbf{r})\frac{\partial}{\partial x_m}G(\mathbf{r},\mathbf{r}') = -\delta(\mathbf{r}-\mathbf{r}')\,\delta_{in} \tag{6.3}$$

Note that this is the analogue of Eq. 5.1, but for spatially varying λ_{iklm}. Taking the Fourier transform of Eq. 6.3, we obtain

$$\begin{aligned}\lambda^{\mathsf{h}}_{iklm}q_k q_m \tilde{G}_{ln}(\mathbf{q},\mathbf{r}') &\\ + \Delta\lambda_{iklm}\sum_{\mathbf{q}'}\tilde{\chi}_{\mathsf{d}}(\mathbf{q}-\mathbf{q}')\,q_k q'_m \tilde{G}_{ln}(\mathbf{q}',\mathbf{r}') &\\ = \frac{1}{(2\pi)^3}\mathsf{e}^{i\mathbf{q}\cdot\mathbf{r}'}\delta_{in}.&\end{aligned} \tag{6.4}$$

Here, $\Delta\lambda_{ijmn} = \lambda^{\mathsf{h}}_{ijmn} - \lambda^{\mathsf{d}}_{ijmn}$, the tildes indicate Fourier-space quantities and $\tilde{\chi}_{\mathsf{d}}$ is the Fourier transform of the characteristic function of the dot, which is given in Appendix F. We write the Fourier-space strain tensor ϵ_{ij} as

$$\tilde{\epsilon}_{lm}(\mathbf{q}) = \epsilon^{\mathsf{T}}_{lm}\tilde{\chi}_{\mathsf{d}}(\mathbf{q}) + \tilde{\epsilon}^{\mathsf{c}}_{lm}(\mathbf{q}), \tag{6.5}$$

where

$$\epsilon^{\mathsf{T}}_{lm} = \varepsilon_{\mathsf{a}}\delta_{lm} + \varepsilon_{\mathsf{ca}}\delta_{l3}\delta_{m3} \tag{6.6}$$

The first term in Eq. 6.5 is the initial strain due to lattice mismatch and the second term is lattice relaxation due to elasticity. Here, $\varepsilon_{\mathsf{a}} = \left(a^{\mathsf{h}} - a^{\mathsf{d}}\right)/a^{\mathsf{d}}$, $\varepsilon_{\mathsf{c}} = \left(c^{\mathsf{h}} - c^{\mathsf{d}}\right)/c^{\mathsf{d}}$, $\varepsilon_{\mathsf{ca}} = \varepsilon_{\mathsf{c}} - \varepsilon_{\mathsf{a}}$. a^{h} and c^{h} are the lattice constants of the host material and, a^{d} and c^{d} are of dot material. More specifically, a is the xy-plane lattice constant and c is the lattice constant along the z-axis. Reference [42] showed that the Green's tensor can be related to the strain $\tilde{\epsilon}^{\mathsf{c}}_{lm}(\mathbf{q})$ to obtain

$$\begin{aligned}\lambda^{\mathsf{h}}_{iklm} q_k \tilde{\epsilon}^{c}_{lm}(\mathbf{q}) \\ + \Delta\lambda_{iklm} q_k \sum_{\mathbf{q}'} \tilde{\chi}_{\mathsf{d}}\left(\mathbf{q}-\mathbf{q}'\right)\tilde{\epsilon}^{c}_{lm}\left(\mathbf{q}'\right) \\ = -\lambda^{\mathsf{d}}_{ikpr}\tilde{\epsilon}^{T}_{pr} q_k \tilde{\chi}^{d}(\mathbf{q}),\end{aligned} \tag{6.7}$$

This is a nonlinear differential in $\tilde{\epsilon}^{\mathsf{c}}_{lm}(\mathbf{q})$, and we seek a solution in the form of a power series such that

$$\tilde{\epsilon}^{\mathsf{c}}_{lm}(\mathbf{q}) = \tilde{\epsilon}^{(0)}_{lm}(\mathbf{q}) + \tilde{\epsilon}^{(1)}_{lm}(\mathbf{q}) + \tilde{\epsilon}^{(2)}_{lm}(\mathbf{q}) + \cdots, \tag{6.8}$$

with $\tilde{\epsilon}^{(N)}_{lm}(\mathbf{q}) \propto \left(\frac{\Delta\lambda}{\lambda}\right)^N$, and the condition $\frac{\Delta\lambda}{\lambda} \ll 1$ ensures convergence of the series. The leading term $\tilde{\epsilon}^{(0)}_{lm}$ corresponds to uniform elastic constants of the dot with each subsequent term being a correction to include spatial variations due to the alloy profile. By inserting Eq. 6.8 into Eq. 6.7 and using the Einstein summation convention, we find that

$$\begin{aligned}\tilde{\epsilon}^{(N)}_{lm}(\mathbf{q}) = \frac{(2\pi)^3}{2}\Big[F^{(N)}_{p}(\mathbf{q})\, q_l \tilde{G}^{\mathsf{h}}_{mp}(\mathbf{q}) \\ + F^{(N)}_{p}(\mathbf{q})\, q_m \tilde{G}^{\mathsf{h}}_{lp}(\mathbf{q})\Big]\end{aligned} \tag{6.9}$$

where

$$F^{(0)}_{i}(\mathbf{q}) = -\lambda^{\mathsf{d}}_{ikpr}\epsilon^{T}_{pr} q_k \tilde{\chi}_{\mathsf{d}}(\mathbf{q}) \tag{6.10}$$

$$F^{(N)}_{i}(\mathbf{q}) = -\Delta\lambda_{iklm} q_k \frac{(2\pi)^3}{V}\sum_{\mathbf{q}'}\tilde{\chi}_{\mathsf{d}}\left(\mathbf{q}-\mathbf{q}'\right)\tilde{\epsilon}^{(N-1)}_{lm}\left(\mathbf{q}'\right) \tag{6.11}$$

Equations 6.9 and 6.11 are corrected from Ref. [42] and $\tilde{G}^{\mathsf{h}}_{in}$ is the Green's tensor for a system with uniform elastic constants of the host material, as shown in Eq. E.31.

We compare the strain corrected at various orders according to Eq. 6.8 to the usually considered case of uniform elastic constants of the host material. Figure 6.3 shows the convergence of the strain corrections for the 1D QD

array system described in Section 6.2.1. We quantify convergence with the following metric for the norm of the strain:

$$|\tilde{\epsilon}| = \sqrt{\sum_{m \geqslant l} \frac{V}{(2\pi)^3} \int \mathbf{dq}^3 \; |\tilde{\epsilon}_{lm}(\mathbf{q})|^2} \tag{6.12}$$

where $m \geqslant l$ indicates the sum of the unique elements of the strain tensor ($\tilde{\epsilon}_{11}$, $\tilde{\epsilon}_{22}$, $\tilde{\epsilon}_{33}$, $\tilde{\epsilon}_{23}$, $\tilde{\epsilon}_{13}$, $\tilde{\epsilon}_{12}$). The green line in Fig. 6.3 compares $\tilde{\epsilon}$ when calculated from Eq. 6.9 to $\tilde{\epsilon}^{\mathsf{GaN}}$, which is calculated assuming spatially uniform elastic constants of GaN. Blue line shows the self-convergence of the power series in Eq. 6.8. From these results, we conclude that a second order correction is sufficient to have strain converged within 1% in self-convergence and that this converged strain differs from the uniform case by about 6%, indicating that the elastic constant corrections produce significant changes in strain fields of InGaN systems. In Sec. 6.2.3, we show that the calculated piezoelectric potential remains essentially unchanged from 3rd order corrections and up, consistent with Fig. 6.3. Given that including these corrections is not computationally costly, we have included third order corrections in all of our calculations unless stated otherwise.

Figure 6.4 shows the hydrostatic strain, $\epsilon_{\mathsf{hydro}} = \epsilon_{xx} + \epsilon_{yy} + \epsilon_{zz}$, along a cut through the axis of the dot, showing relaxation of strain inside the dot with each additional correction. For this sample dot, the bulk lattice constants are 5% larger in the dot than in the barrier, and the compressive strain near the center ($\epsilon_{zz} \approx -0.012$, $\epsilon_{xx} \approx -0.028$) produces local lattice constants that are closer to the bulk InGaN values than bulk GaN, which is consistent with the choice to model spatially varying elastic constants.

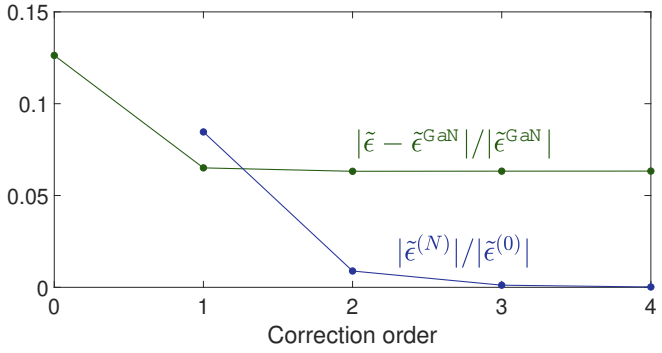

Figure 6.3: Convergence of the strain due to spatially varying elastic constants with perturbation order for a 1D QD array as described in Table 6.1. Green line is the relative difference between the corrected strain and the strain with uniform λ of GaN. The zeroth term is the case of uniform λ of InGaN with alloy fraction of the dot. Converged strain has 6% relative difference from the case of λ^{GaN}, indicating that the corrections are necessary for accurate strain fields. Blue line is the magnitude of each term in Eq. 6.8 as a fraction of the zeroth term. Correction magnitudes are less than 1% starting from second order.

The strain produced by the QD superlattice can be obtained from linear superposition of the single-dot strain. However, we want the ability to study dots that are completely uncoupled, both electronically and from strains of the fictitious periodic array. References [59, 78] proposed a method to allow the simultaneous treatment of a large unit cell for the strain problem and a small unit cell for the electronic problem, which together allow isolated dots to be considered in a computationally tractable manner. In this case of two independent cells, the strain is calculated

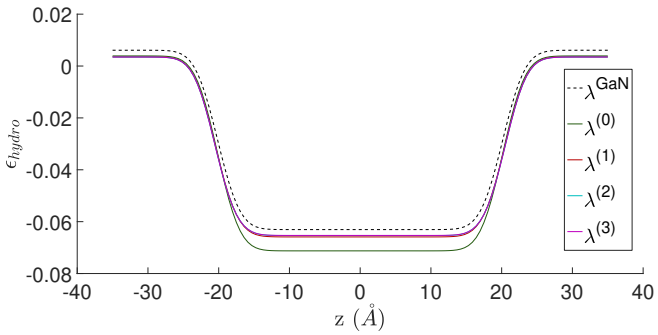

Figure 6.4: Hydrostatic strain for increasing correction orders in the elastic constants. Black dashed line is strain assuming uniform elastic constants of the host material λ^{GaN} while solid lines are for spatially varying elastic constants with correction order $\lambda^{(N)}$. As the correction order $\lambda^{(N)}$ increases, the strain moves toward the uniform case λ^{GaN}. Note that the lines for $\lambda^{(2)}$ and $\lambda^{(3)}$ are overlapping. However, the uniform case λ^{GaN} underestimates the strain in the dot.

in its own real space unit cell Ω_{s} with volume V_{s}. We denote the strain reciprocal unit cell as Ω_{s}^{-1} such that it contains the wave vectors $\mathbf{Q}$, which are defined similarly to Eq. 6.1 for the electronic cell. Given that strain relaxes more slowly than bound electronic wavefunctions, we only consider $V_{\mathsf{s}} \geq V_{\mathsf{e}}$. In this two-unit-cells approximation, the Fourier transform of the strain produced by the QD array is

$$\begin{aligned}\tilde{\epsilon}_{ij}^{\mathsf{a}}(\mathbf{q}) &= \frac{(2\pi)^3}{V_{\mathsf{s}}} \sum_{\mathbf{Q}\in\Omega_{\mathsf{s}}^{-1}} \tilde{\epsilon}_{ij}(\mathbf{Q})\, \tilde{\chi}_{\mathsf{e}}(\mathbf{q}-\mathbf{Q}) \\ &= \frac{(2\pi)^3}{V_{\mathsf{s}}} \left(\tilde{\epsilon}_{ij} * \tilde{\chi}_{\mathsf{e}}\right)_{\mathsf{s}}(\mathbf{q}), \end{aligned} \tag{6.13}$$

where χ_{e} is the characteristic function of the electronic unit cell Ω_{e} in Ω_{s}, which is given for our case in Appendix F. Superscript "a" indicates array. We follow the notation that $\mathbf{q} \in \Omega_{\mathsf{e}}^{-1}$ and $\mathbf{Q} \in \Omega_{\mathsf{s}}^{-1}$. $\left(\tilde{\epsilon}_{ij} * \tilde{\chi}_{\mathsf{e}}\right)_{\mathsf{s}}(\mathbf{q})$ denotes a convolution where the subscript "s" indicates that the convolution is over the wave vectors $\mathbf{Q} \in \Omega_{\mathsf{s}}^{-1}$, see Appendix D for Fourier transform and convolution definitions. We show in Sec. 6.3.2 that choosing the linear dimensions of Ω_{s} to be integer multiples of the linear dimensions of Ω_{e} ensures that all vectors $\mathbf{q} \in \Omega_{\mathsf{e}}^{-1}$ are also in Ω_{s}^{-1}. This choice allows Eq. 6.13 to be evaluated efficiently.

6.2.3 Piezoelectric potential

III-nitride materials are strongly piezoelectric, having both spontaneous and strain-driven polarizations [92, 93]. Calculation of the polarization from an electric field requires knowledge of the static dielectric constant ε of the material. In prior work, Fourier space based approaches have assumed a uniform dielectric constant. Given the large difference in ε_{r} between GaN and InN (9.8 and 13.8, respectively), spatial variation can be significant in InGaN QD systems. We present a method to obtain the Fourier transform of the scalar potential $\tilde{\varphi}(\mathbf{q})$ assuming $\varepsilon(\mathbf{r})$ changes with the local alloy fraction. We find that correcting for the spatial dependence of the dielectric function leads to important changes in the piezoelectric potential and show in Sec. 6.5 that this change significantly shifts the lowest

QD energy levels. We do not consider metallic screening, which can be important in highly doped materials [94–96].

Generally, we can write the displacement field $\mathbf{D}(\mathbf{r})$ as

$$\mathbf{D}(\mathbf{r}) = \varepsilon_0 \mathbf{E}(\mathbf{r}) + \mathbf{P}_{\mathsf{tot}}(\mathbf{r}),$$

where $\mathbf{E}(\mathbf{r})$ is the electric field, ε_0 is the vacuum permittivity, and $\mathbf{P}_{\mathsf{tot}}$ is the total polarization. In the strained material, there are three sources of polarization: bound charge, strain and spontaneous polarization,

$$\mathbf{P}_{\mathsf{tot}}(\mathbf{r}) = \mathbf{P}_{\mathsf{bnd}}(\mathbf{r}) + \mathbf{P}_{\mathsf{st}}(\mathbf{r}) + \mathbf{P}_{\mathsf{sp}}(\mathbf{r}).$$

Here, we assume no free charge screening. Assuming $\mathbf{P}_{\mathsf{bnd}}$ to be linear with the electric field and incorporated into $\varepsilon(\mathbf{r})$ as usual,

$$\mathbf{D}(\mathbf{r}) = \varepsilon(\mathbf{r})\mathbf{E}(\mathbf{r}) + \mathbf{P}_{\mathsf{st}}(\mathbf{r}) + \mathbf{P}_{\mathsf{sp}}(\mathbf{r}), \tag{6.14}$$

where $\mathbf{P}_{\mathsf{st}}(\mathbf{r}) + \mathbf{P}_{\mathsf{sp}}(\mathbf{r}) = \mathbf{P}(\mathbf{r})$ is the residual polarization after electric-field-induced bound charge has been included in $\varepsilon(\mathbf{r})$.

We take $\varepsilon(\mathbf{r})$ to be ε^{h} in the host material and ε^{d} in the dot material, so

$$\varepsilon(\mathbf{r}) = \varepsilon^{\mathsf{h}} + \left(\varepsilon^{\mathsf{d}} - \varepsilon^{\mathsf{h}}\right)\chi_{\mathsf{d}}(\mathbf{r}). \tag{6.15}$$

We obtain ε^{d} by linear interpolation of the binary compounds' bulk dielectric constants. Taking the divergence of Eq. 6.14, using $\boldsymbol{\nabla}\cdot\mathbf{D} = 0$ and taking the Fourier transform gives

$$\mathscr{F}\{\varepsilon(\mathbf{r})E_m(\mathbf{r})\}(\mathbf{q}) = -\frac{q_n}{q_m}\tilde{P}_n(\mathbf{q}), \tag{6.16}$$

where we have used the property $\mathscr{F}\left\{\partial_n \tilde{P}_n\right\} = -(iq_n)\mathscr{F}\{P_n\}$. Taking the inverse Fourier transform and solving for the electric field gives

$$E_m(\mathbf{r}) = -\frac{1}{\varepsilon(\mathbf{r})}\mathscr{F}^{-1}\left\{\frac{q_n}{q_m}\tilde{P}_n(\mathbf{q})\right\} \tag{6.17}$$

where $\mathscr{F}^{-1}$ represents the inverse Fourier transform. Using $E_m = -\partial_m\varphi$, where $\partial_m \equiv \frac{\partial}{\partial x_m}$ and $\varphi(\mathbf{r})$ is the scalar potential,

$$\tilde{\varphi}(\mathbf{q}) = -\frac{i}{q_m}\mathscr{F}\left\{\frac{1}{\varepsilon(\mathbf{r})}\mathscr{F}^{-1}\left\{\frac{q'_n}{q'_m}\tilde{P}_n(\mathbf{q}')\right\}(\mathbf{r})\right\}. \tag{6.18}$$

For the case of sharp alloy interfaces, $\chi_{\mathsf{d}}(\mathbf{r})$ is either 1 or 0 and Eq. 6.15 gives

$$\frac{1}{\varepsilon(\mathbf{r})} = \frac{1}{\varepsilon^{\mathsf{h}}} + \left(\frac{1}{\varepsilon^{\mathsf{d}}} - \frac{1}{\varepsilon^{\mathsf{h}}}\right)\chi_{\mathsf{d}}(\mathbf{r}). \tag{6.19}$$

We treat the case of smoothly varying alloy fraction in Sec. 6.4. Putting this result in Eq. 6.18 gives

$$\tilde{\varphi}\left(\mathbf{q}\right) = \tilde{\varphi}^{\mathsf{h}}\left(\mathbf{q}\right) + \Delta\tilde{\varphi}\left(\mathbf{q}\right) \tag{6.20}$$

with

$$\tilde{\varphi}^{\mathsf{h}}\left(\mathbf{q}\right) = -\frac{i}{q_m}\frac{1}{\varepsilon^{\mathsf{h}}}\frac{q_n}{q_m}\tilde{P}_n\left(\mathbf{q}\right) \tag{6.21}$$

$$\Delta\tilde{\varphi} = \frac{-i}{q_m}\left(\frac{1}{\varepsilon^{\mathsf{d}}} - \frac{1}{\varepsilon^{\mathsf{h}}}\right)\mathscr{F}\left\{\chi_{\mathsf{d}}\mathscr{F}^{-1}\left\{\frac{q'_n}{q'_m}\tilde{P}_n\left(\mathbf{q}'\right)\right\}\right\} \tag{6.22}$$

Here, $\tilde{\varphi}^{\mathsf{h}}$ is the contribution to φ with $\varepsilon_{\mathsf{r}}\left(\mathbf{r}\right) = \varepsilon^{\mathsf{h}}$, and $\Delta\tilde{\varphi}$ is the change in $\tilde{\varphi}$ due to the dot material having a different dielectric constant. See reference [43] for both spontaneous and strain-induced polarization fields $\tilde{P}_n\left(\mathbf{q}\right)$ for the wurtzite crystal structure.

We now show the piezoelectric potentials that result from this formulation, for our model system in Sec. 6.2.1. Figure 6.5(a) shows $\varphi\left(z\right)$ along the central axis of the QD calculated with constant ε of the dot and host and with Eq. 6.20. As expected, the calculation with spatially varying $\varepsilon\left(\mathbf{r}\right)$ agrees with $\varphi^{\mathsf{d}}_{\mathsf{uni}}$ inside the dot and also agrees with $\varphi^{\mathsf{h}}_{\mathsf{uni}}$ outside the dot, with a transition near the boundary that is captured by neither of the uniform cases.

Figure 6.4 showed how spatially varying elastic constants change strain profiles. Figure 6.5(b) shows how those strain corrections change φ. The peak correction of 8 mV is significant if looking to converge the energy levels within a few meV.

6.3 Commensurate unit cells for efficient coupling of strain in $\mathbf{k}\cdot\mathbf{p}$

Here, we briefly present the QD $\mathbf{k}\cdot\mathbf{p}$ model we use for electronic structure calculations. This QD Hamiltonian is written in a symmetry adapted basis, which reduces the computational cost for calculating and diagonalizing the Hamiltonian. In this symmetry adapted basis, we show how the strain produced by the QDs contributes to the Hamiltonian. We also introduce strain effects using a larger unit cell than the electronic cell defined in Fig. 6.2. In this section, our goal is to show our method of efficiently including strain in the QD $\mathbf{k}\cdot\mathbf{p}$ model, which we do by choosing the strain unit cell's dimensions to be integer multiples of the unit cell used for the electronic structure calculations. The $\mathbf{k}\cdot\mathbf{p}$ model and symmetry adapted basis are standard, and we briefly describe them and refer to the sources for full descriptions.

We use the 8-band $\mathbf{k}\cdot\mathbf{p}$ model for bulk wurtzite material presented in Ref. [39] in the basis of Γ-point Bloch functions, which includes spin-orbit coupling, crystal field splitting, and strain. Since choosing angular momentum $\hat{J}_z$ eigenfunctions aids in the construction of a symmetry adapted basis, we rotate the 8-band Hamiltonian into the $\hat{J}_z$ eigenbasis, similar to Ref. [35]. See Appendix A for details. Recent work has alternatively obtained $\mathbf{k}\cdot\mathbf{p}$ parameters directly in the symmetry adapted basis using *ab initio* calculations [97].

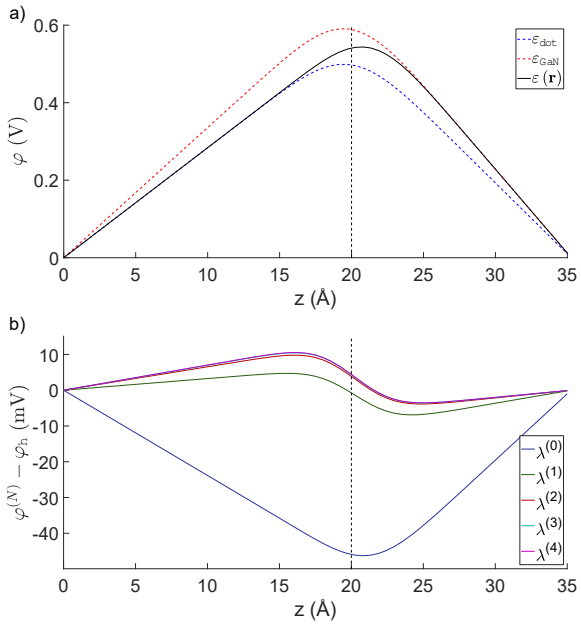

Figure 6.5: (a) Piezoelectric potential $\varphi(z)$ along the central axis, beginning in the center of the dot. Blue and red dashed lines show φ calculated with uniform $\varepsilon(\mathbf{r}) = \varepsilon^{\mathsf{h}}$ and $\varepsilon(\mathbf{r}) = \varepsilon^{\mathsf{d}}$, respectively. Black line shows the case with spatially varying $\varepsilon(\mathbf{r})$. Note that the φ is antisymmetric in z. These results show that the case of uniform ε cannot accurately describe φ throughout the system. Strain calculations include third-order corrections for the nonuniform elastic constants. (b) Potential difference for various elastic constant corrections. Difference is with respect to $\varphi_{\mathsf{h}}(\mathbf{r})$, which is calculated with uniform $\lambda(\mathbf{r}) = \lambda^{\mathsf{GaN}}$. The zeroth order case (blue line) shows $\lambda(\mathbf{r}) = \lambda^{\mathsf{d}}$. Includes a spatially varying dielectric constant. System parameters are given in Table 6.1. Both calculations implement an alloy smoothing of $\boldsymbol{\delta} = [1.5, 1.5, 2.5]\,\mathring{A}$, which is described in Sec. 6.4. Vertical dashed lines indicate the nominal material interface without smoothing.

6.3.1 Quantum dot $\mathbf{k}\cdot\mathbf{p}$

We construct the QD Hamiltonian by giving the bulk Hamiltonian a spatial dependence. The solution is expanded using slowly varying envelope functions [41, 42, 58, 59]. The envelope functions are periodic with the superlattice and can be expanded in Fourier domain using the superlattice reciprocal wave vectors $\mathbf{q}$ defined in Eq. 6.1. Writing the envelope functions in terms of plane waves leads to a non-sparse Hamiltonian [42, 58]. Due to the broken translation symmetry, we apply the substitution $k_j \to -i\frac{\partial}{\partial x_j}$ and symmetrize the operations to preserve Hermiticity [41, 58, 65]. For computational efficiency, we use a symmetry adapted basis, which takes advantage of the C_6 symmetry of the wurtzite crystal structure by block diagonalizing the Hamiltonian. Symmetry adapted bases have been fully described for both zincblende and wurtzite systems [41, 43]. The symmetry-adapted basis reduces the Fourier space sampling to a single sextant $0 \le q_y \le \tan\left(\frac{2\pi}{6}\right) q_x$ of the full space and block diagonalizes the Hamiltonian into 6 blocks, which are labeled by $m_f = \{-5/2, -3/2, -1/2, 1/2, 3/2, 5/2\}$. The label m_f can be interpreted as a total quasi angular momentum [43, 59]. The basis elements are

$$|m_f, \alpha, \mathbf{q}\rangle = \Lambda(m_f, \alpha, \mathbf{q}, \mathbf{r})\,|u_\alpha\rangle \tag{6.23}$$

where

$$\Lambda\left(m_f,\alpha,\mathbf{q},\mathbf{r}\right)=\frac{1}{\sqrt{6}}\sum_{l=0}^{5}e^{i\left(\overleftrightarrow{\mathbf{R}}_l\mathbf{q}\right)\cdot\mathbf{r}}e^{il\phi[m_f-J_z(\alpha)]} \tag{6.24}$$

when either q_x or q_y is nonzero and $\Lambda\left(m_f,\alpha,\mathbf{q},\mathbf{r}\right)=e^{i\mathbf{q}\cdot\mathbf{r}}$ when $q_x=q_y=0$ and $J_z(\alpha)=m_f$. $\overleftrightarrow{\mathbf{R}}_l$ is the $l\phi$ rotation around the z-axis with $\phi=2\pi/6$. This basis consists of the basis functions of the irreducible representations of the double group $\bar{C}_6$. This block diagonalization greatly reduces the computational cost to diagonalize the Hamiltonian. Equation 6.24 distinguishes wave vectors that are purely along the z-axis from those that have an xy-component, which we denote by $\mathbf{q}_z$ and $\mathbf{q}$, respectively. These two cases differ because a z-axis rotation leaves $\mathbf{q}_z$ invariant while sending $\mathbf{q}$ to a new wave vector $\overleftrightarrow{\mathbf{R}}_l\mathbf{q}$. The case of $|m_f,\alpha,\mathbf{q}_z\rangle$ with $J_z\left(\alpha\right)\neq m_f$ does not exist in the basis set. In this basis, the eigenvalue problem is

$$\sum_{\alpha=1}^{8}\sum_{\mathbf{q}}\mathcal{H}_{m_f\alpha'\alpha}\left(\mathbf{q}',\mathbf{q}\right)A_{im_f}^{\alpha}\left(\mathbf{q}\right)=E_iA_{im_f}^{\alpha'}\left(\mathbf{q}'\right) \tag{6.25}$$

where

$$\begin{aligned}\mathcal{H}_{m_f\alpha'\alpha}\left(\mathbf{q}',\mathbf{q}\right)&\equiv\langle m_f,\alpha',\mathbf{q}'|\hat{\mathcal{H}}|m_f,\alpha,\mathbf{q}\rangle\\&=\frac{1}{V_{\mathsf{e}}}\int_{V_{\mathsf{e}}}\mathrm{d}^3\mathbf{r}\,\Lambda^*\left(\mathbf{r}\right)H_{\alpha'\alpha}\Lambda\left(\mathbf{r}\right)\end{aligned} \tag{6.26}$$

where we have dropped some arguments in Λ for brevity. $H_{\alpha'\alpha}$ are the bulk Hamiltonian matrix elements presented in Appendix A. Expressions for $\mathcal{H}_{m_f\alpha'\alpha}\left(\mathbf{q}',\mathbf{q}\right)$ are fully written out in Appendix G in terms of the bulk Hamiltonian matrix elements and QD characteristic function.

6.3.2 Strain and piezoelectric coupling

Deformation potentials and piezoelectric effects, which are both strain-driven, are important for accurate calculations of electronic structure in III-N materials. However, including deformation potentials can be computationally costly for the case of isolated dots. The two-unit cell approach presented in Sec. 6.2.2 allows for the study of isolated dots, but at the cost of computationally expensive convolutions. Additionally, another layer of convolutions appears in the Hamiltonian matrix elements, leading to composed convolutions. Here, we present the matrix elements due to strain and show our computationally efficient approach of dealing with these composed convolutions by choosing the linear dimensions of the real-space strain cell Ω_{s} to be integer multiples of those of the electronic cell Ω_{e}.

The bulk strain Hamiltonian matrix elements in Eqs. A.4 and A.6 can be written as

$$H_{\alpha'\alpha}=\sum_{ij}f_{\alpha'\alpha}^{ij}\epsilon_{ij}\left(\mathbf{r}\right)$$

where the $f^{ij}_{\alpha'\alpha}$ consist of $\mathbf{k}\cdot\mathbf{p}$ parameters (a_i, l_i, m_i and n_i). Using the prescription of Sec. 6.3.1 and defining

$$S^{ll'm_f}_{\alpha',\alpha} \equiv e^{i\phi\left\{l\left[m_f - J_z(\alpha)\right] - l'\left[m_f - J_z(\alpha')\right]\right\}}$$
$$S^{l'm_f}_{\alpha'} \equiv e^{-il'\phi\left[m_f - J_z(\alpha')\right]},$$

the strain contributions to the QD Hamiltonian are

$$\mathcal{H}^{ij,\mathsf{st}}_{m_f\alpha'\alpha}(\mathbf{q}',\mathbf{q}) = \frac{1}{6}\sum_{l,l'=0}^{5} S^{ll'm_f}_{\alpha',\alpha} h^{ij,\mathsf{st}}_{\alpha'\alpha}\left(\overleftrightarrow{\mathbf{R}}_{l'}\mathbf{q}', \overleftrightarrow{\mathbf{R}}_{l}\mathbf{q}\right)$$
$$\mathcal{H}^{ij,\mathsf{st}}_{m_f\alpha'\alpha}(\mathbf{q}',\mathbf{q}_z) = \frac{1}{\sqrt{6}}\sum_{l'=0}^{5} S^{l'm_f}_{\alpha'} h^{ij,\mathsf{st}}_{\alpha'\alpha}\left(\overleftrightarrow{\mathbf{R}}_{l'}\mathbf{q}', \mathbf{q}_z\right)$$
$$\mathcal{H}^{ij,\mathsf{st}}_{m_f\alpha'\alpha}(\mathbf{q}'_z,\mathbf{q}_z) = h^{ij,\mathsf{st}}_{\alpha'\alpha}(\mathbf{q}'_z,\mathbf{q}_z)$$

where

$$h^{ij,\mathsf{st}}_{\alpha'\alpha}(\mathbf{q}',\mathbf{q}) = \frac{(2\pi)^3 f^{ij,\mathsf{h}}_{\alpha'\alpha}}{V_{\mathsf{e}}}\tilde{\epsilon}^{\mathsf{a}}_{ij}(\mathbf{q}'-\mathbf{q}) + \frac{(2\pi)^6\left(f^{ij,\mathsf{d}}_{\alpha'\alpha} - f^{ij,\mathsf{h}}_{\alpha'\alpha}\right)}{V_{\mathsf{e}}^2}\left(\tilde{\chi}_{\mathsf{d}} * \tilde{\epsilon}^{\mathsf{a}}_{ij}\right)_{\mathsf{e}}(\mathbf{q}'-\mathbf{q}). \tag{6.27}$$

Here, $f^{ij,\mathsf{h}}_{\alpha'\alpha}$ and $f^{ij,\mathsf{d}}_{\alpha'\alpha}$ are the $\mathbf{k}\cdot\mathbf{p}$ parameters for bulk host and dot materials, respectively. $\tilde{\epsilon}^{\mathsf{a}}_{ij}$ is the strain produced by the QD array calculated in Sec. 6.2.2. The subscript "e" in $\left(\tilde{\chi}_{\mathsf{d}} * \tilde{\epsilon}^{\mathsf{a}}_{ij}\right)_{\mathsf{e}}$ indicates that the convolution is over the wave vectors $\mathbf{q} \in \Omega_{\mathsf{e}}^{-1}$. Inserting the superlattice strain from Eq. 6.13 into the $\mathbf{k}\cdot\mathbf{p}$ strain matrix elements from Eq. 6.27 leads to composed convolutions,

$$\left(\tilde{\chi}_{\mathsf{d}} * \tilde{\epsilon}^{\mathsf{a}}_{ij}\right)_{\mathsf{e}}(\mathbf{q}) = \sum_{\mathbf{q}'\in\Omega_{\mathsf{e}}^{-1}} \tilde{\chi}_{\mathsf{d}}(\mathbf{q}')\,\tilde{\epsilon}^{\mathsf{a}}_{ij}(\mathbf{q}-\mathbf{q}')$$
$$= \frac{(2\pi)^3}{V_{\mathsf{s}}}\sum_{\mathbf{q}'\in\Omega_{\mathsf{e}}^{-1}} \tilde{\chi}_{\mathsf{d}}(\mathbf{q}') \sum_{\mathbf{Q}\in\Omega_{\mathsf{s}}^{-1}} \tilde{\epsilon}_{ij}(\mathbf{Q})\,\tilde{\chi}_{\mathsf{e}}(\mathbf{q}-\mathbf{q}'-\mathbf{Q}) \tag{6.28}$$

which can be computationally demanding depending on the number of wave vectors used. The original proposal of using a large strain cell with a smaller electronic cell imposed no relationship between their sizes [59, 78]. Equation 6.28 then requires evaluating $\tilde{\chi}_{\mathsf{e}}$ at points $\mathbf{q}-\mathbf{q}'-\mathbf{Q}$ that are contained on neither the electronic nor strain meshes, requiring a unique convolution be calculated for every $\mathbf{q}' \in \Omega_{\mathsf{e}}^{-1}$. It is well known that using the convolution theorem to compute a convolution between two vectors of length N has a computational cost that scales as $N\log(N)$. Similarly, the computational cost for a convolution on a 3D $N\times N\times N$ mesh scales as $N^3\log(N)$. Computing the composed convolutions in Eq. 6.28 would then scale as $N_{\mathsf{e}}^3\log(N_{\mathsf{e}})\,N_{\mathsf{s}}^3\log(N_{\mathsf{s}})$ since a convolution in $\mathbf{Q}$ has to be calculated for each $\mathbf{q}'$. Note that the convolutions in Eq. 6.28 are linear convolutions, which implies that the arrays of function values must be padded with zeros before using the convolution theorem, as detailed

in Appendix D. This zero padding increases both N_e and N_s. We show that choosing a strain unit cell to be a supercell of the electronic unit cell reduces the required number of convolutions, leading to an improved scaling of $N_\mathsf{e}^3 \log(N_\mathsf{e}) + N_\mathsf{s}^3 \log(N_\mathsf{s})$.

Choosing the strain unit cell linear dimensions to be multiples of the electronic cell, we have

$$L_i^\mathsf{s} = n_i L_i^\mathsf{e} \qquad i = 12, 3 \tag{6.29}$$

where the n_i take positive integer values. This choice of real-space unit cells leads to the electronic Fourier space mesh being contained in the strain mesh $\Omega_\mathsf{e}^{-1} \subset \Omega_\mathsf{s}^{-1}$. The wave vectors $\mathbf{Q}$ then have a spacing that is a fraction of the spacing of the electronic wave vectors $\mathbf{q}$,

$$\Delta Q_i = \frac{\Delta q_i}{n_i} \tag{6.30}$$

See Fig. 6.6 for an example of commensurate meshes and their overlapping Fourier-space meshes. Note that from Eq. 6.28, $\tilde{\epsilon}_{ij}^\mathsf{a}$ is then only sampled at points $\Delta\mathbf{q} = \mathbf{q} - \mathbf{q}'$, which belong to the electronic mesh. Our procedure starts with using the convolution theorem (see Appendix D) to efficiently calculate the inner convolution $\left(\tilde{\epsilon}_{ij} * \tilde{\chi}_\mathsf{e}\right)_\mathsf{s}(\mathbf{Q})$ on the strain mesh to obtain $\tilde{\epsilon}_{ij}^\mathsf{a}(\mathbf{Q})$. Since the wave vectors $\mathbf{Q}$ also contain the wave vectors $\mathbf{q}$, we can then extract the points that lie on the electronic mesh to obtain $\tilde{\epsilon}_{ij}^\mathsf{a}(\mathbf{q})$. Lastly, we perform the second convolution $\left(\tilde{\chi}_\mathsf{d} * \tilde{\epsilon}_{ij}^\mathsf{a}\right)_\mathsf{e}(\mathbf{q})$, again using the convolution theorem. This workflow is shown in Fig. 6.8. This method computes only two 3D convolutions and so has a complexity scaling of $N_\mathsf{e}^3 \log(N_\mathsf{e}) + N_\mathsf{s}^3 \log(N_\mathsf{s})$, which is a considerable improvement compared to the non-commensurate case. Note that N_s is generally much larger than N_e to obtain appropriate convergence, so the computational cost is dominated by the convolutions on Ω_s^{-1}.

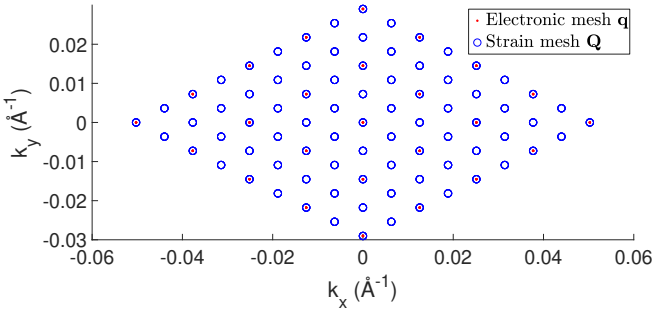

Figure 6.6: Example of commensurate Fourier space meshes where $n_{12} = 2$, leading to $\Delta Q_i = \frac{\Delta q_i}{2}$, which implies the vectors $\mathbf{Q}$ contain all the vectors $\mathbf{q}$.

By limiting ourselves to commensurate unit cells, we may not be choosing the optimal unit cell size in terms of Fourier-space sampling. In other words, we are likely to have a strain unit cell that is larger than is necessary, which means more wave vectors are necessary to reach the same maximum point in Fourier space. Therefore, we can decrease N_s if we allow ourselves to consider non-commensurate cells so that the strain unit cell is more optimal. However, in our case with commensurate cells, we always perform two 3D convolutions, while with

non-commensurate cells, we would have to perform N_e 3D convolutions, which can be observed from Eq. 6.28. Therefore, if we used non-commensurate cells, we would reduce the number of wave vector points, but by increasing the number of necessary convolutions. We can then ask if the commensurate cell method is always faster than considering incommensurate unit cells or if there is some set of parameters that would allow the incommensurate case to be faster. Regardless of method, we expect to approach the complexity scalings described above in order to converge the system and so expect the commensurate method to always be faster near convergence, which is the parameter space of interest.

Let us consider a small example for the case of an isolated QD (large n_{12} and n_3). For simplicity, let us ignore the truncation of the mesh for the C_6 symmetry, and assume that $m_{12} = m_3$ and $n_{12} = n_3$. This means we have a $N_\mathsf{e} \times N_\mathsf{e} \times N_\mathsf{e}$ electronic mesh, where $N_\mathsf{e} = (2m_{12} + 1) = (2m_3 + 1)$ and, assuming commensurate cells, a $N_\mathsf{s} \times N_\mathsf{s} \times N_\mathsf{s}$ strain mesh, where $N_\mathsf{s} = n_{12}N_\mathsf{e} = n_3 N_\mathsf{e}$. Consider the case where the ideal strain cell is 7.1 times bigger than the electronic cell, leading to $N'_\mathsf{s} = 7.1N_\mathsf{e}$ strain mesh points. In our approach of commensurate cells, we are forced to take $n_{12} = n_3 = 8$, giving $N_\mathsf{s} = 8N_\mathsf{e}$ strain mesh points for the case of commensurate cells and leading to a ratio of $N'_\mathsf{s}/N_\mathsf{s} = 7.1/8 = 0.89$. In the case of the commensurate cells, we would have scaling of the computational cost that goes like $C_\mathsf{c} = \alpha \left[N_\mathsf{e}^3 \log(N_\mathsf{e}) + N_\mathsf{s}^3 \log(N_\mathsf{s})\right]$ and $C_\mathsf{i} = \alpha \left[N_\mathsf{e}^3 \log(N_\mathsf{e})\, N_\mathsf{s}'^3 \log(N'_\mathsf{s})\right]$ for the incommensurate cells, where α is a constants. Taking $m_{12} = m_3 = 6$, we find $S_\mathsf{i}/S_\mathsf{c} = 3833$ and therefore treating slightly more wave vectors with commensurate boxes is expected to be significantly more efficient. The commensurate cell method being more efficient is also observed for any value of $n_{12} > 1$ such that $n'_{12} = n_{12} - 0.9$, as shown in Fig. 6.7. To speed up the calculation in the case of incommensurate cells, one could calculate the quantity $\tilde{\epsilon}^\mathsf{a}_{ij}$ from Eq. 6.28 on the strain mesh and use 3D interpolation to obtain its values on the electronic mesh, but that method would also require care in convergence and accuracy.

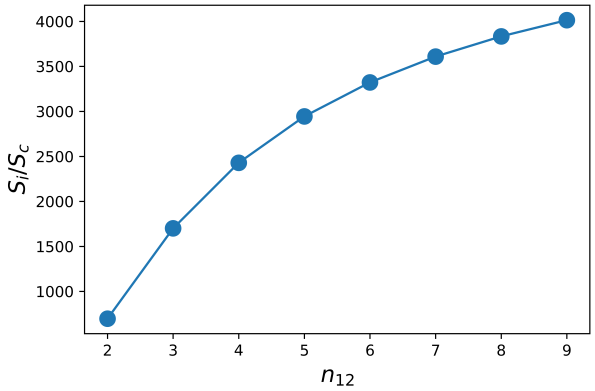

Figure 6.7: Ratio of the computational scaling of the incommensurate box and commensurate box methods as n_{12} is varied and $n'_{12} = n_{12} - 0.9$. Here, we have taken $m_{12} = m_3 = 6$.

The piezoelectric potential brings no additional complexity, and the workflow for calculating the piezoelectric potential is shown in Fig. 6.8. The potential is initially calculated on the strain mesh, and the electronic mesh

portion is extracted to calculate the piezoelectric potential contributions to the Hamiltonian, which are written out in Appendix G.

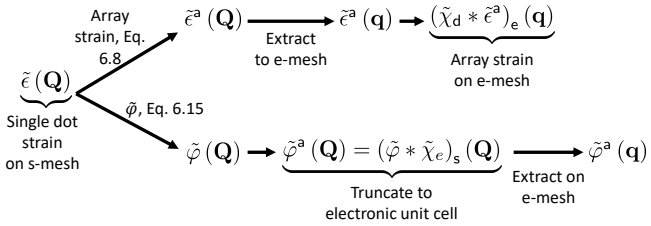

Figure 6.8: Workflows for calculating strain $\tilde{\epsilon}^{a}$ and piezoelectric potential $\tilde{\phi}^{a}$ on the electronic mesh of an array of dots, beginning from the strain of a single dot on the strain mesh. Upper path shows the composed convolutions of the form in Eq. 6.28, which are necessary to compute the matrix elements in Eq. 6.27. Lower branch shows steps for calculating $\tilde{\phi}^{a}$, which is used in Eqs. G.13, G.14 and G.15. e-mesh and s-mesh signify the Fourier space electronic and strain meshes, respectively.

6.4 Smooth alloy profile

When InGaN devices are grown by MBE, indium diffuses between layers [17]. While most studies of MBE-grown materials simulate abrupt junctions, this diffusion leads to smoothing of the material interfaces, producing a continuously varying alloy fraction, which changes the local band properties and lattice constant, which in turn change strain and polarization fields. This smooth alloy profile must be included for accurate modeling. The smooth indium profiles produced by diffusion differ from the random alloy fluctuations studied in [69] using atomistic modeling. Reference [70] has used random fluctuations at material interfaces to study quantum well width fluctuations, which is similar to the profiles produced by indium diffusion. In this section, we present a method to include alloy diffusion effects in Fourier-space calculations by effectively smoothing the characteristic function of the dot. Smooth indium profiles also provide a computational benefit, since sharp features of the confining potentials are removed, so fewer wave vectors are required to attain convergence. We use this method to produce an alloy profile that models indium diffusion and address how spatially varying material parameters can be included within piezoelectric potential and electronic structure calculations. Our examples focus on indium alloying, but the methods are general for all $\mathbf{k} \cdot \mathbf{p}$ calculations of alloy structures. Reference [98] presents a similar procedure for strain calculations only, with a linearly graded alloy profile.

6.4.1 Smoothing method

In the case of a sharp material interface, the local alloy fraction $X(\mathbf{r})$ can be defined by the characteristic function of the dot

$$X(\mathbf{r}) = X_0 \chi_{\mathsf{d}}(\mathbf{r}),$$

where the characteristic function $\chi_{\mathsf{d}}(\mathbf{r})$ defines the geometry of the dot with indium fraction X_0. By convolving with a Gaussian $G(\mathbf{r},\boldsymbol{\delta}) = \frac{1}{(2\pi)^{\frac{3}{2}}\delta_x\delta_y\delta_z}\mathsf{e}^{-\frac{1}{2}\left(\frac{x^2}{\delta_x^2}+\frac{y^2}{\delta_y^2}+\frac{z^2}{\delta_z^2}\right)}$ or other kernel, we can obtain a smooth version of the characteristic function

$$\begin{aligned} X_{\mathsf{sm}}(\mathbf{r}) &= (X_0\chi_{\mathsf{d}} * G)(\mathbf{r}) \\ &= X_0\chi_{\mathsf{sm}}(\mathbf{r}), \end{aligned}$$

where $\boldsymbol{\delta} = [\delta_x, \delta_y, \delta_z]$ controls the radius of smoothing and needs to be chosen to model the desired alloy diffusion. $G(\mathbf{r},\boldsymbol{\delta})$ is normalized to preserve the total amount of alloying element, and $\chi_{\mathsf{sm}}(\mathbf{r})$ is a smoothed characteristic function. Using the convolution theorem, the smoothed characteristic function satisfies

$$\tilde{\chi}_{\mathsf{sm}}(\mathbf{q}) = \tilde{\chi}_{\mathsf{d}}(\mathbf{q})\,\mathsf{e}^{-\frac{\left(\delta_x^2q_x^2+\delta_y^2q_y^2+\delta_z^2q_z^2\right)}{2}}.$$

Note that $\chi_{\mathsf{sm}}(\mathbf{r})$ is no longer strictly a characteristic function, as it takes values continuously between 0 and 1. We now show that it can be inserted in place of the characteristic function in the previous sections to give $\mathbf{k}\cdot\mathbf{p}$ parameters, strain and piezoelectric fields accurately with a smooth alloy profile.

6.4.2 Material parameters

We focus on the case of InGaN to illustrate the interpolation of material parameters. In the case of sharp material interfaces, the host and dot regions each consist of uniform material. The host material is a binary material and has well-defined parameters. The dot region consists of alloyed InGaN, and its parameters are obtained by either linear or bowed interpolation of bulk GaN and InN parameters, which are listed in Appendix A.

In the case of a smooth alloy profile, the dot and host regions are no longer uniform, giving the material parameters a smooth spatial dependence. Parameters that were linearly interpolated in the sharp interface case can still be obtained from a simple linear interpolation based on the local alloy fraction $X(\mathbf{r})$. The bandgap E_{CV} is nonlinear in the alloy fraction due to a bowing factor. This nonlinearity prevents us from using the convolution theorem in calculating the Hamiltonian matrix elements. However, we show that neglecting the bowing parameters in the alloy-smoothing region can still give computationally efficient and accurate smoothed profiles when the alloy fraction is not too large.

The local value for any of the linearly interpolated material parameters depends on the local alloy fraction

$$f(\mathbf{r}) = f^{\mathsf{B}}X(\mathbf{r}) + [1 - X(\mathbf{r})]\,f^{\mathsf{A}} \tag{6.31}$$

where f can be a parameter such as lattice constant, and subscripts A and B stand for the two binary materials, GaN and InN for example. For this case of linearly interpolated quantities, smoothed parameters can be written

as follows:

$$f(\mathbf{r}) = f^{\mathsf{d}}\chi_{\mathsf{sm}}(\mathbf{r}) + [1 - \chi_{\mathsf{sm}}(\mathbf{r})]\, f^{\mathsf{A}} \tag{6.32}$$

where f^{d} is the linearly interpolated material parameter at the nominal alloy fraction X_0 of the QD.

Bandgaps do not vary linearly with alloy fraction and are generally well described with a bowing term, as

$$E_{\mathsf{CV}}(\mathbf{r}) = E^{\mathsf{B}}_{\mathsf{CV}} X(\mathbf{r}) + [1 - X(\mathbf{r})]\, E^{\mathsf{A}}_{\mathsf{CV}} - X(\mathbf{r})\,[1 - X(\mathbf{r})]\, C$$

where C is a bowing constant. More complicated forms allow the bowing factor to depend on alloy fractions [99], but we do not consider such effects. Following the same procedure as in Eq. 6.32, a smoothed version can be written as follows:

$$\begin{aligned} E_{\mathsf{CV}}(\mathbf{r}) = E^{\mathsf{A}}_{\mathsf{CV}} + \left[E^{\mathsf{B}}_{\mathsf{CV}} - E^{\mathsf{A}}_{\mathsf{CV}}\right] E^{\mathsf{A}}_{\mathsf{CV}} X_0 \chi_{\mathsf{sm}}(\mathbf{r}) \\ - C X_0 \chi_{\mathsf{sm}}(\mathbf{r})\,[1 - X_0 \chi_{\mathsf{sm}}(\mathbf{r})] \end{aligned} \tag{6.33}$$

where the first two terms are the linear interpolation and the last term is the bowing. This bowing term brings additional complexity when performing $\mathbf{k}\cdot\mathbf{p}$ calculations due to the nonlinearlity in $\chi_{\mathsf{sm}}(\mathbf{r})$. Dealing with this nonlinearity is trivial for the case of sharp material interfaces since $\chi^2 = \chi$, which is not true for χ_{sm}. The bandgap appears in the Hamiltonian through the diagonal element E'_{C} in Eq. A.5. In the plane wave basis, the contributions of the nonlinear term $CX_0^2\chi^2_{\mathsf{sm}}$ are

$$\begin{aligned} h^{\mathsf{nonlinear}}_{E_{\mathsf{CV}}}(\mathbf{q}', \mathbf{q}) &= C X_0^2 \frac{1}{V} \int_V \mathsf{d}^3\mathbf{r}\, \mathsf{e}^{-i\mathbf{q}'\cdot\mathbf{r}} \chi^2_{\mathsf{sm}}(\mathbf{r})\, \mathsf{e}^{i\mathbf{q}\cdot\mathbf{r}} \\ &= C X_0^2 \frac{(2\pi)^6}{V^2} \left(\chi_{\mathsf{sm}} * \chi_{\mathsf{sm}}\right)(\mathbf{q}' - \mathbf{q})\,. \end{aligned}$$

Additional convolutions must then be calculated to include the bowing of the band gap, increasing the computational cost. However, we show that we can, to good approximation, use a bandgap that is linearly interpolated between the host and dot bandgaps,

$$E_{\mathsf{CV}}(\mathbf{r}) \approx E^{\mathsf{d}}_{\mathsf{CV}} \chi_{\mathsf{sm}}(\mathbf{r}) + [1 - \chi_{\mathsf{sm}}(\mathbf{r})]\, E^{\mathsf{h}}_{\mathsf{CV}}. \tag{6.34}$$

Here, $E^{\mathsf{d}}_{\mathsf{CV}}$ is the bulk bandgap at an alloy fraction of X_0 and $E^{\mathsf{h}}_{\mathsf{CV}}$ is the bulk band gap of the host material. This linear interpolation gives a good approximation for the bandgap for most regions, as shown in Fig. 6.9 and overestimates E_{CV} near the interfaces. Disagreements increase with dot indium fraction. The regions with largest deviation are in the same locations where E_{CV} changes over 1.5 eV, so we expect the slight shift of position where each bandgap occurs to have minimal effect. We can estimate from Fig. 6.9 that the shift in the effective height of the dot in the z-direction is smaller than $\delta_z/2$, so a particle-in-a-box model allows the fractional change in the

most confined energy level to be estimated to be approximately $\delta_z/h \approx 6\%$. The neglect of the χ^2_{sm} term allows the theory to stay linear and therefore efficiently calculated with the convolution theorem. If the smoothing radius becomes comparable to the dot dimensions, this approximation may need to be reconsidered.

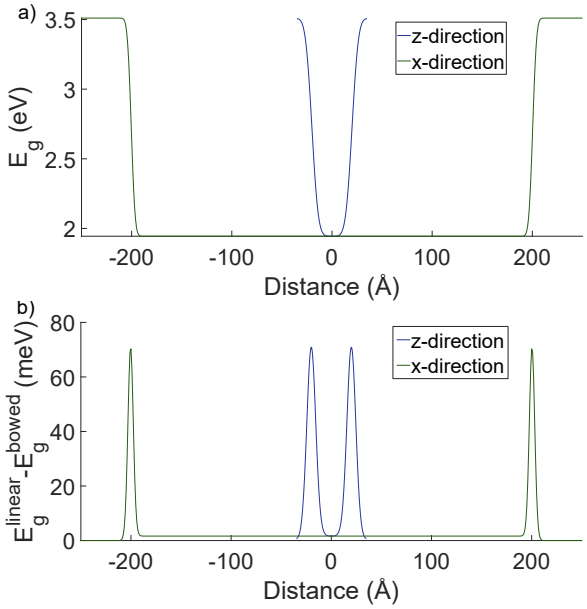

Figure 6.9: (a) Bandgap in a QD system obtained by bowed interpolation using Eq. 6.33 along the z and x axes through the center of the dot. Bandgap obtained from linear interpolation using Eq. 6.34 is visually indistinguishable. (b) Difference of the bowed and linearly interpolated band gaps along the z and x axes. QD parameters are listed in Table 6.1. For computational simplicity and smooth curves, these results were obtained using a rectangular real-space unit cell with dimensions $L_{\mathsf{x}} = L_{\mathsf{y}} = 500\mathring{A}$, $L_{\mathsf{z}} = 70\mathring{A}$ and a smoothing of $\delta = [3, 3, 5]\mathring{A}$.

6.4.3 Strain and the piezoelectric potential

Here we show how smoothing is included in the strain and piezoelectric potential calculations. Once calculated, those strains and piezoelectric potentials can be included in the $\mathbf{k} \cdot \mathbf{p}$ model exactly as shown in Sec. 6.3.2.

Following the derivations from Refs. [42, 71], it is not obvious how smoothing is to be implemented in strain calculations since they begin from the stress of the sharp interface dot/barrier interface. However, Ref. [91] presents an alternative derivation for the same strain calculation indicating that $\chi(\mathbf{r})$ in the strain expressions can be exchanged for the smoothed version $\chi_{\mathsf{sm}}(\mathbf{r})$ without any further changes, which is the approach taken by Ref. [98].

For the piezoelectric potential, Eq. 6.19 for the spatially varying inverse dielectric constant assumed sharp interfaces. In the case of a smooth indium profile, we use Eq. 6.31 to write

$$\varepsilon(\mathbf{r}) = \varepsilon^{\mathsf{B}} X(\mathbf{r}) + [1 - X(\mathbf{r})]\,\varepsilon^{\mathsf{A}} \tag{6.35}$$

In the scenario where $X(\mathbf{r})$ is spatially varying, Eq. 6.19 can no longer be applied, because the inverse of the

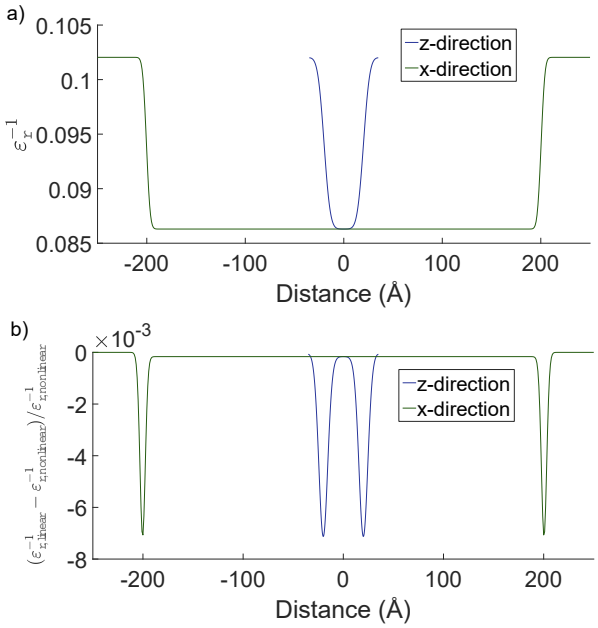

Figure 6.10: (a) Inverse dielectric constant from Eq. 6.35 along the z and x axes through the center of the dot. Linearly interpolated inverse from Eq. 6.36 is visually indistinguishable. (b) Relative difference of the linear and nonlinear interpolations. QD parameters are listed in Table 6.1. Results used the same rectangular mesh and smoothing as in Fig. 6.9.

dielectric constant is not a linear function of indium. However, similar to the bandgap, we find that

$$\frac{1}{\varepsilon(\mathbf{r})} \approx \frac{1}{\varepsilon^{\mathsf{d}}}\chi_{\mathsf{sm}}(\mathbf{r}) + [1 - \chi_{\mathsf{sm}}(\mathbf{r})]\frac{1}{\varepsilon^{\mathsf{A}}} \tag{6.36}$$

still gives an accurate representation of $\varepsilon^{-1}(\mathbf{r})$. Figure 6.10 shows in our test case a disagreement of less than 1 percent between the inverse dielectric from Eq. 6.35 and the linear interpolation in Eq. 6.36. The form of Eq. 6.36 allows us to use Eqs. 6.20-6.22 for the piezoelectric potential with a simple substitution of $\chi(\mathbf{r})$ by $\chi_{\mathsf{sm}}(\mathbf{r})$.

6.5 Impacts of corrections

In this section, we apply our methodology to study the case of a 1D array of QDs, inspired by those in Ref. [17]. Unlike those experimental dot arrays embedded in nanowires, ours is an infinite 1D chain embedded in bulk GaN. We achieve this 1D array by taking $n_3 = 1$ to fully couple the dots in the z-direction and choose L_{12} and n_{12} sufficiently large to avoid both electronic and strain effects from neighboring dots in the xy-plane. In the experimental dot arrays, strain can be significantly modified by the nanowire walls, but the strength of the piezoelectric field along the wire axis, which plays the most important role in modifying the band structure from a strain-free calculation, is significant in both cases [1].

We investigate convergence of the lowest electron and hole state energies E_{C} and E_{V}, which define the fundamental gap of the dot $E_0 \equiv E_{\mathsf{C}} - E_{\mathsf{V}}$. More specifically, we show that the largest wave vector sampled plays a

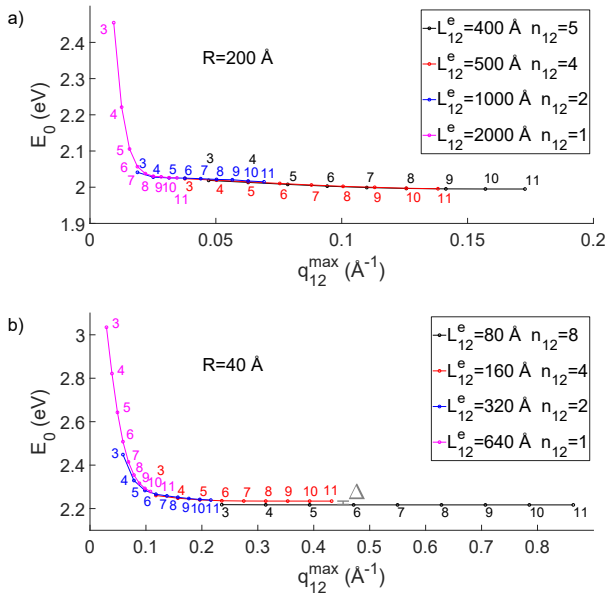

Figure 6.11: Convergence of the fundamental gap E_0 for a 1D array of QDs versus the maximum magnitude of q_{12} included in the $\mathbf{k}\cdot\mathbf{p}$ calculations. L^e_{12} and n_{12} vary while (a) has $R = 200\mathring{A}$ with strain box size held constant at $L^s_{12} = 10R$ and (b) has $R = 40\mathring{A}$ with $L^s_{12} = 16R$. Plane wave sampling m_{12} from 3 to 11 are shown for each choice of L^e_{12}; the number next to each point indicates m_{12}. Different values of m_{12}, L^e_{12} that produce the same q^{max}_{12} can be seen to produce approximately the same E_0, showing that q^{max}_{12} is a useful metric for convergence of these states. Since $q^{max}_{12} = m_{12}\pi/L^e_{12}$ and computational cost scales with m_{12}, smaller L^e_{12} allows easier access to large q^{max}_{12}. In both panels, the black curves have $L^e_{12} = 2R$, so the dots touch each other at the 6 edges of the hexagonal unit cell. In the larger dot, there is no signature of dot-dot tunneling, while in the smaller dot, tunneling of the wavefunctions into neighboring dots causes E_0 to have a significant change, labeled Δ. For the $R = 40\mathring{A}$ case, E_c and E_v were found to be converged within 5 meV with $m_{12} = 7$, $m_3 = 4$ and $n_{12} = 4$, smaller than those required for the larger dot, reported in Table 6.1.

dominant role in convergence and that the choice of hexagonal or circular dot cross sections is not significant for dots that maintain the same volume. We also show the energy shifts experienced by these two states when using uniform or spatially varying material parameters and when including alloy smoothing.

Table 6.2: Energy shifts due to spatially varying $\lambda(\mathbf{r})$ and $\varepsilon(\mathbf{r})$ relative to the case with uniform constants of the host material λ^{GaN} and ε^{GaN}. Cylindrical dot with parameters in Table 6.1.

Energy shifts	$\lambda(\mathbf{r})$ & ε^{GaN}	λ^{GaN} & $\varepsilon(\mathbf{r})$	$\lambda(\mathbf{r})$ & $\varepsilon(\mathbf{r})$
ΔE_C (meV)	16.7	46.7	64.7
ΔE_V (meV)	-5.1	-30.6	-37.4
ΔE_0 (meV)	21.7	77.4	102.1

We model an infinite 1D QD array with parameters listed in Table 6.1. The 1D dot array has an experimentally well characterized dot-dot spacing in z, which fixes $L^e_3 = L^s_3 = L_3$, leaving L_{12} and n_{12} to be fixed. These QDs have a rather large radius, so the smallest spatial feature that we need to resolve is the decay of the bound wavefunctions into the classically forbidden region. Given that bound wavefunctions decay faster than strain, we need wave vectors that are relatively large to be able to resolve the wavefunctions. Increasing m_{12} increases the maximum wave vector contained in the mesh, but we can also sample at larger wave vectors by using a smaller L^e_{12}. However, if the

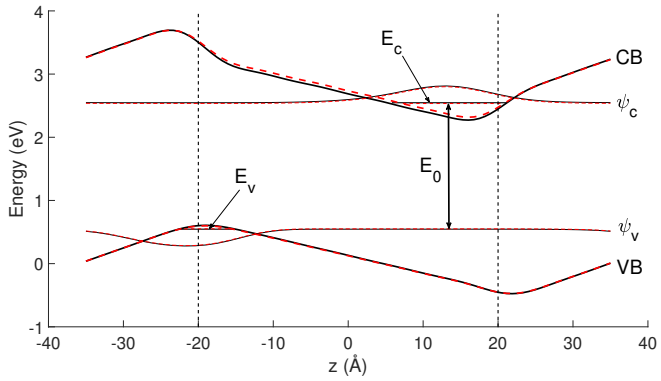

Figure 6.12: Electronic structure of a cylindrical (solid, black) and hexagonal prism (dashed, red) QD superlattice system along the central axis of the dot for $\boldsymbol{\delta} = [1.5, 1.5, 2.5]\mathring{A}$, corresponding to $s = 1$ in Fig. 6.13(a). Other system parameters are in Table 6.1. The circular and hexagonal dots are not significantly different for these band-edge states, with eigenenergies differing by less than 12 meV. Thick lines labeled CB and VB are the bulk band edges under the influence of the piezoelectric field and the diagonal component of the deformation potential. Lowest bound electron and hole states energies, E_{C} and E_{V}, are shown by the horizontal lines. Thin lines labeled ψ_{C} and ψ_{V} are z-axis projections of the probability distributions obtained from the envelope functions for these states. Dashed vertical lines are the nominal material interfaces before smoothing. These calculations include spatially varying elastic and dielectric constants.

electronic cell is chosen too small, then there can be electronic wavefunction overlap between states of neighboring dots. We must then choose L_{12}^{e} as small as possible while also avoiding dot-dot interactions. As for strain, in order to study a 1D array, we must choose n_{12} sufficiently large to have $L_{12}^{\mathsf{s}} = n_{12}L_{12}^{\mathsf{e}}$ large enough that the strain of the QD superlattice does not extend across neighboring strain unit cells in the xy-plane.

With this intuition, we turn to the convergence of E_0 in terms of m_{12}, L_{12}^{e} and n_{12}. Figure 6.11(a) shows the importance of the largest $\mathbf{q}$ in the electronic mesh, q_{12}^{max}, for convergence of E_0. In this study, L_{12}^{e} and n_{12} are chosen to keep a constant $L_{12}^{\mathsf{s}} = L_{12}^{\mathsf{e}}n_{12} = 2000\mathring{A}$. We observe that E_0 is to good approximation a function of only q_{12}^{max} and not of m_{12} and L_{12}^{e}, converging toward the same value for all choices of L_{12}^{e}. We also observe that the smallest L_{12}^{e} with highest m_{12} gives the most converged E_0, since $q_{12}^{\mathsf{max}} = m_{12}\pi/L_{12}^{\mathsf{e}}$. The black line in Fig. 6.11(a) represents the case of dots touching in the xy plane and, interestingly, does not break the convergence trend. However, we do find a break in the convergence trend for smaller dots in Fig. 6.11(b). This difference occurs because smaller dots have wavefunctions that extend further outside the dot region, which makes them more able to tunnel to a neighboring dot. Consequently, care has to be taken in choosing the unit cell dimensions for small QDs.

The lowest QD confined electron and hole energies, E_{C} and E_{V}, have each been converged within 5 meV by choosing m_{12}, m_3 and n_{12} sufficiently large, see Table 6.1. At these parameters, a full simulation is takes about 32 minutes. Material parameters are listed in Appendix A. Band edges and the lowest energy states are shown in Fig. 6.12. The thick lines labeled CB and VB represent the bulk band edges modified by the piezoelectric potential and diagonal portion of the deformation potential; the valence band edge includes a third of the trace of the 3×3 valence band block from Eq. A.6. Figure 6.12 shows the electronic structure of both circular and hexagonal QDs. Convergence parameters were kept the same for both sets of calculations, and the radii were chosen to maintain

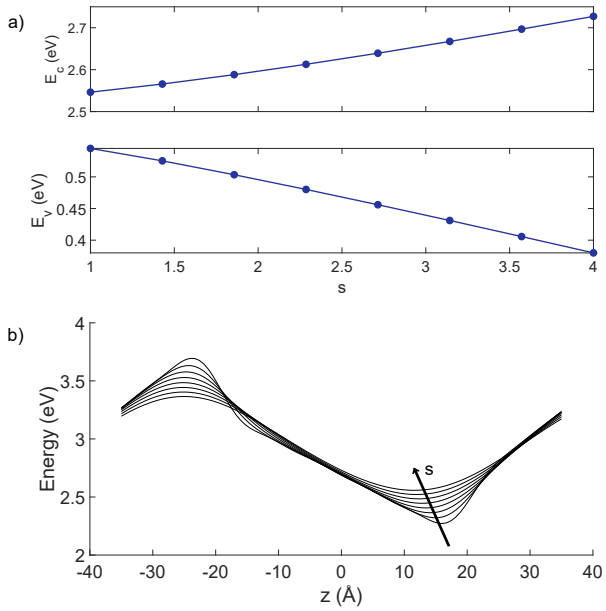

Figure 6.13: Effects of varying the indium diffusion through the parameter s such that $\boldsymbol{\delta} = s[1.5, 1.5, 2.5]\mathring{A}$ for (a) E_C and E_V and (b) bulk conduction band edge. Remaining parameters are as listed in Table 6.1. Increase in indium diffusion leads to less confinement, which pushes the two states apart in energy, widening the electronic gap E_0. Electronic structure for $s = 1$ is shown in Fig. 6.12.

the same volume. We conclude that the energies of the most confined electron and holes states are insensitive to the dot geometry.

The modifications in both the strain and piezoelectric potential due to spatially varying elastic and dielectric constants also have effects on the electronic structure. Table 6.2 shows how much E_V and E_C shift due to the corrections. We find that both corrections push the states apart, leading to an energy gap 100 meV larger than from simpler calculations with uniform ε and λ, a significant change that shows the importance of accurate modeling of dielectric and elastic parameters.

Figure 6.13(a) shows that indium diffusion pushes the lowest electron and hole states apart, which is due to changes in the confining potentials. From Fig. 6.13(b), we see that indium diffusion reduces the depth of the confining potential. The valence band shows similar behavior, leading to E_V being pushed down in energy. Consequently, the gap E_0 increases with indium diffusion.

In the case of sharp material interfaces, large wave vectors are needed to resolve the discontinuous parameter profiles. Smoothing removes the sharp interfaces, reducing the required $q_{12}^{\max}$ for the same degree of convergence. This reduction gives convergence with smaller m_{12} and m_3 and therefore reduced computational cost are needed with increasing $\boldsymbol{\delta}$. In Figs. 6.13 (a) and (b), we converged for the case of $s = 1$, guaranteeing convergence for the rest of the sweep.

6.6 Conclusions

We have demonstrated techniques for and results of four modifications of standard Fourier space QD $\mathbf{k}\cdot\mathbf{p}$ theory. We have presented a method to include smoothly varying alloy profiles in Fourier-based strain, piezoelectric potential and $\mathbf{k}\cdot\mathbf{p}$ calculations. We have shown that the effects of spatially varying elastic and dielectric parameters are non-negligible on the strain and piezoelectric potential and also produce important shifts of the lowest electron and hole states, significantly changing the calculated gap of the QD. For the case of $\mathbf{k}\cdot\mathbf{p}$ theory for isolated dots, we have presented a new method of overlapping electronic and strain meshes to facilitate the coupling of strain into the $\mathbf{k}\cdot\mathbf{p}$ Hamiltonian, greatly reducing the computational cost of calculating the Hamiltonian matrix elements. Lastly, we have shown that the maximum wave vector contained in the electronic sampling mesh is the most important criterion for determining convergence of QD levels.

Acknowledgements

We acknowledge useful conversation with Stanko Tomić about Fourier space $\mathbf{k}\cdot\mathbf{p}$ methods. We acknowledge funding from the Ontario Early Researcher Award and NSERC CREATE TOP-SET Program (Award number 497981).

Data availability

The data that support the findings of this study are available from the corresponding author upon reasonable request.

Chapter 7

InGaN quantum dot superlattices as ratchet band solar cells

*Reproduced from IEEE Journal of Photovoltaics, **12**, 474 (2022), with the permission of JPV [100]*

Luc Robichaud and Jacob J. Krich

We investigate the construction of ratchet band solar cells using InGaN quantum dots. The strong piezoelectric potentials can spatially separate electron and hole states. This spatial separation reduces both radiative and non-radiative recombination within the quantum dot, providing one of the key characteristics of a ratchet band system. Ratchet band solar cells have proven difficult to realize experimentally, and the piezoelectric potential in InGaN quantum dots could provide a spatial ratchet that can operate at room temperature with broadband absorption. We use a $\mathbf{k}\cdot\mathbf{p}$ model to calculate the electronic structure and absorptance of a superlattice of InGaN/GaN quantum dots. We present an improved method to calculate the absorptance for the bound-to-continuum transition by using bulk $\mathbf{k}\cdot\mathbf{p}$ states to approximate the host material continuum states. We show an example dot structure that could act as a ratchet band solar cell. Using the absorptances of the quantum dot array, we calculate a detailed balance efficiency of 36% for the system. Optimizing the dot geometry and alloy fraction allows detailed balance efficiencies up to 42%, but at the cost of losing the spatial ratchet.

Notes:

Shortly after this paper was published and I defended my thesis, I found a scaling error in the absorption cross-sections calculations. The error was in the units of the matrix elements of Eq. 7.2, which were too large by a factor of 25.6. The absorption cross sections depend on the matrix element squared, so they all must be decreased by a factor of 656 compared to the published version. Figure 7.5 has been changed to reflect the new, smaller, absorption cross sections. Unfortunately, this large change indicates that these QD systems are not nearly as absorptive as we had thought. For all later results, the absorptivity α is proportional to the absorption cross sections, and alpha

enters the absorptance a only when multiplied by the number of layers of dots, N_{L}, as in Eq. 7.9. Therefore, all previous results are correct as long as the values of N_{L} from the original manuscript are multiplied by 656. So, for example, the base case of N_{L}=200 studied for most of this chapter actually becomes N_{L}=1.3×10^5. Figures 7.5, 7.8, 7.11 and the discussion have been updated to make this change.

Had this error been caught in advance, we would have instead considered more strongly doped QDs to increase absorption. The weakest absorption, as shown in Fig. 7.5, is the CI absorption. Assuming σ_{CI} to scale linearly with the number of electrons, increasing the doping from $3\times10^{17}\,\mathrm{cm}^{-3}$ to $2\times10^{20}\,\mathrm{cm}^{-3}$ for the clear ratchet system and $1\times10^{18}\,\mathrm{cm}^{-3}$ to $7\times10^{20}\,\mathrm{cm}^{-3}$ for the efficiency optimized systems would entirely compensate for the decrease in σ_{CI}. With appropriate optimization of dot geometry and alloy fraction, we believe that a more reasonable doping level could be found that gives satisfactory efficiency. The IV absorption could then be regained by optimizing the QD geometry and alloying as to give the IV process access to a larger portion of the solar spectrum. The central point of this Chapter, which is that the InGaN QD system can realize a spatial ratchet, remains unaffected by this error.

An erratum will be submitted to the journal.

Also different from the original publication is:

- Figure 7.2 and its mentions in the text were not included in the original publication.
- Original publication's introduction did not mention what type of machine calculations were performed on.

7.1 Introduction

The Shockley-Queisser limit is the limiting efficiency for a solar cell with a single band gap, 31% under a 1-sun 6000-K black body [25]. Several architectures promise higher efficiencies, and multijunction devices have already surpassed the Shockley-Queisser limit. The ratchet band solar cell is one such promising system, having a 1-sun detailed balance limiting efficiency of 48.5% [13].

The ratchet band solar cell (RBSC) was originally proposed to consist of 4 bands: valence (VB), intermediate (IB), ratchet (RB) and conduction (CB) [13]. Figure 7.1(a) shows a RBSC, adapted for quantum dot (QD) systems by including a VB offset. Two key features make RB systems highly efficient. First, recombination from the RB to the VB is forbidden, so that carriers have long lifetimes in the RB after fast relaxation from the IB. The defining characteristics of a RB system are three optical transitions with threshold energies E_{CV}, E_{CI}, and E_{IV}, as indicated by the colored arrows in Fig. 7.1(a). The second advantageous feature is that $E_{\mathsf{CI}}+E_{\mathsf{IV}}$ does not need to equal E_{CV}, unlike in a standard intermediate band solar cell (IBSC) [5]. This relaxation can lead to better voltage matching between the subgap and CV transitions than in an IB system [26, 101].

While realizations of RB systems have been demonstrated using InAs QDs [15], quantum-cascade-style AlGaAs/-GaAs quantum well superlattice [14] and erbium-doped GaAs [16], none has been implemented that can function

at room temperature with the required broadband absorptions. We propose using InGaN QDs in GaN for RBSCs. InGaN QD systems have been of interest for IBSCs [1, 7]. Confined systems such as QDs and wells have electronic structures that are tunable by change of size and composition such that the optical threshold energies do not necessarily sum to the host material's band gap, as required for an RBSC [15]. InGaN QDs are also strongly piezoelectric such that the strain-driven piezoelectric potential can spatially separate the lowest confined electron and hole states [89], as illustrated in Fig. 7.3. This system presents a realizable spatial ratchet with optical transitions as indicated in Fig. 7.3, analogous to those of Fig. 7.1(a). Separating the states reduces the wavefunction overlap, reducing both radiative recombination and local nonradiative processes.

In this work, we construct an example of a clear ratchet (CR) band system, attainable with a 3-dimensional superlattice of InGaN QDs in GaN. We calculate the electronic structure of the QD superlattice, including strain, deformation potentials, and piezoelectric potentials, using a computationally efficient symmetry adapted $\mathbf{k}\cdot\mathbf{p}$ method for cylindrical QDs that includes effects of alloy diffusion and nonuniform elastic and dielectric constants [77]. We calculate the subgap absorption cross sections of the dots and construct absorptances of systems with 665-131000 QD layers and an ideal Lambertian back reflector [102], where the quantum dot structure is doped so some IB states in the QD are filled. We find the energy thresholds corresponding to E_{IV} and E_{CI} in Fig. 7.1(a). We show how E_{IV} changes with doping, demonstrating the key feature of a RB system: An absorption threshold E_{IV} larger than the fundamental gap of the quantum dot system, in the limit that the doping goes to zero. For the absorption cross sections, we demonstrate an improved method for calculating bound-to-continuum absorption.

We use detailed balance calculations to determine the limiting efficiency possible for such devices, using both idealized energy thresholds and the $\mathbf{k}\cdot\mathbf{p}$-predicted absorptances. The full process of our modeling is shown in Fig. 7.2. Also shown by the grey arrow is the option to optimize by varying the system's parameters. We use the efficiency landscape to optimize the QD geometry and alloy fraction, giving an efficiency of 42%, larger than the 36% of the CR system. The efficiency-optimized (EO) system does not have a ratchet. Despite the differences in detailed balance efficiencies, in real materials with nonradiative recombination, the ratchet structure may have a higher efficiency than the EO structure due to reduced IV recombination. While both systems considered here show need of many QD layers, we also show that the efficiency of the CR system is sensitive on the number layers, while the EO system is less sensitive, meaning we could consider a system where we sacrifice some of the spatial ratchet so we can reduce the number of layers.

This manuscript is an extended version of an IEEE Photovoltaics Specialists Conference Proceeding [103], which presented preliminary results on the CR system. This version adds Section 7.4 with the detailed balance efficiency calculations for the QD system using idealized energy thresholds as well as $\mathbf{k}\cdot\mathbf{p}$-predicted absorptances. With those efficiencies, we optimize the QD geometry and indium fraction to maximize efficiency. In addition to Sec 7.4, this version adds Figures 7.3(b), 7.4, 7.5(b), 7.6(b), 7.8, 7.9, 7.10, 7.11 and new results in Fig. 7.7.

All calculations done in this work were performed on a desktop machine with a Intel Core i5-3470 cpu@3.20Ghz

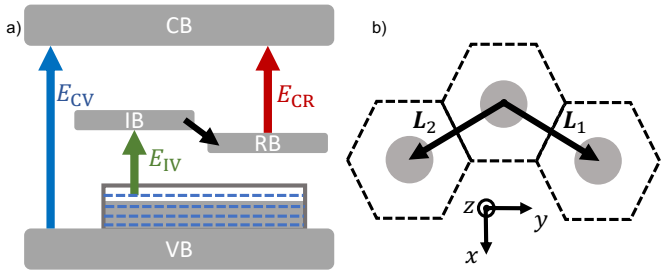

Figure 7.1: (a) QD ratchet band systems, including a VB offset. Colored arrows show the energy thresholds for each transition. Carriers relax from IB to RB. (b) One plane of a hexagonal superlattice of InGaN QDs in GaN. Grey regions indicate the indium-rich regions before indium diffusion, after which there are no sharp material interfaces. L_i are the QD superlattice basis vectors. Dashed region is a superlattice unit cell.

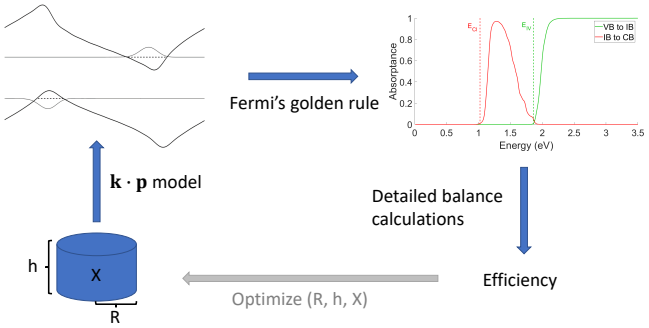

Figure 7.2: Workflow used for modeling InGaN/GaN QD ratchet band solar cell. We start by fixing the system's parameters such as radius, height, indium fraction and unit cell size. Having fixed the parameters, we calculate the electronic structure of the system using the $\mathbf{k}\cdot\mathbf{p}$ model. From the electronic structure, we calculate the optical properties using Fermi's golden rule. Lastly, the calculated absorptances are fed into detailed balance calculations to obtain the power conversion efficiency. Efficiency can then be optimized by varying the system's parameters. In Section 7.4, we vary the dot radius, height and indium fraction, while keeping the dot-to-dot spacing constant.

processor and 24GB of RAM. All code was written in-house using Matlab R2017b.

7.2 Quantum dot electronic structure

We use an 8-band $\mathbf{k}\cdot\mathbf{p}$ model to calculate the single-particle electronic structure of a superlattice of wurtzite InGaN QDs, which we approximate as cylindrical. We previously showed that considering hexagonal dots makes essentially no difference for the most confined energy levels [77]. To preserve the C_6 symmetry of the wurtzite crystal structure, hexagonal periodic boundary conditions are imposed, producing a 3D QD superlattice, as illustrated in Fig. 7.1(b)[42, 58]. The electronic structure methods are described in Ref. [77], and we give a brief summary here. The Hamiltonian is calculated using a symmetry adapted basis, which reduces the computational cost by block diagonalizing the Hamiltonian [43, 59]. Lattice-mismatch driven strain is calculated using a continuum approximation and is included directly in the $\mathbf{k}\cdot\mathbf{p}$ model by deformation potentials [42]. The piezoelectric potential, which is crucial for generating spatially separated electron and hole states, is calculated from the strain using

Maxwell's equations. Indium diffusion is incorporated by smoothing the indium profile with a Gaussian kernel of 5 Å in each direction [77]. Material parameters are the same as those used in Ref. [77] except for the sign of the e_{15} piezoelectric constant.[1] The $\mathbf{k}\cdot\mathbf{p}$ method gives well-resolved energies and eigenstates for the most confined energy levels but is less accurate for the states approaching the continuum [59, 85].

In this work, we highlight two QD superlattices. The first is designed to show a CR effect, which should be experimentally measurable. These QDs have 90 Å radius, 125 Å height and 40% indium fraction with a barrier of 100 Å between dots in both the z direction and in-plane. The resulting hexagonal superlattice unit cell has a thickness of 225 Å and hexagonal edge length of 162 Å, producing a QD areal density of 1.5×10^{11} cm^{-2}. The barrier thicknesses were chosen to be sufficiently small to ensure strong absorption and to help with convergence of the electronic structure [77]. To resolve the states, 25 plane waves were used in the axial direction and 17 were used along each in-plane hexagonal principal axis in the reciprocal space. Note our sampling grid is not rectangular but instead truncated to have a C_6 symmetric grid [77], as is required by a symmetry adapted basis, resulting in a total of 5425 plane waves. We refer to this system as the "clear ratchet" (CR). We also highlight another structure designed to optimize the detailed balance efficiency of the system. This system has dots with a 35 Å radius, 95 Å height, and 76% indium fraction. We kept the same 100 Å dot-to-dot barriers as in the CR system, resulting in a unit cell thickness of 195 Å, hexagonal edge length of 98 Å and an areal QD density of 4.0×10^{11} cm^{-2}. To resolve the states, we found that 19 plane waves were needed along each of the axial and in-plane directions, which gave 5149 plane waves after truncation. We refer to this system as the "efficiency optimized" (EO). The optimization process that produced this structure is described in Section 7.4.

Figure 7.3 shows the electronic structure for both systems. As usual for QD IBSCs, we consider the QD-confined states in the CB to be the IB, while the continuum states form the CB. The VB states are separated by about 2-4 meV for both the CR and EO systems, indicating a high density of states in the VB offset. Colored arrows show the equivalent transition energies of the ideal RBSC shown in Fig. 7.1(a). The IV transition moves electrons from the confined VB states to the confined IB states. In the case of the CR in Fig. 7.3(a), after an electron-hole pair is created via the IV transition, the electron and hole relax towards opposite ends of the dot due to the piezoelectric potential. Once relaxed, the electrons can no longer recombine because states of lower energy are either filled or spatially separated, increasing their lifetime and enabling them to wait longer for a photon for the CI transition. In the EO system of panel (b), the piezoelectric fields are weaker, and there is considerable overlap between the lowest IB and VB states; this system does not have a ratchet. We define the energy separation between the lowest hole and electron states to be E_0. While Fig. 7.3 shows a cut through a single dot in the array, the QD-containing region of the full device is terminated with GaN, and the E_{CV} and E_{CI} energies must be defined by that GaN band structure, to enable extraction of carriers. We therefore take the CI transition to be from the IB to the CB continuum of the

[1] There is a sign error in e_{15} in [77], which follows [39]. This widespread sign error is discussed in greater detail in the erratum [75] to [78], which implements an 8-band $\mathbf{k}\cdot\mathbf{p}$ model using a plane wave basis to describe III-N QDs. This correct sign was also confirmed using ab initio DFT in [79]. We thank Stanko Tomić for making us aware of this error.

host GaN, which is at 3.53 eV in this study; the bandgap of GaN is 3.51 eV and the reference energy is the GaN VB edge without spin-orbit coupling and crystal-field splitting, as described in [35, 39]. Figure 7.3 shows approximate energy thresholds E_{XY} for transitions between bands. In reality, absorption for the IV and CI transitions begins at smaller energies than indicated by the arrows, as we show in detail below. The CI transition can begin at lower energy due to occupancy of higher-lying states in the IB, and the IV transition can begin at lower energy due to the finite spatial extent of the bound wavefunctions. For the systems we consider, $E_{\mathsf{CI}} + E_{\mathsf{IV}} < E_{\mathsf{CV}}$, as depicted in Fig. 7.1(a).

The spatial separation of the lowest energy states in the ratchet system can be seen in the overlap of the VB and IB wavefunctions. In Fig. 7.4, we investigate the overlap between the lowest hole state ψ_1^{VB} and CB states ψ_i^{CB} using the metric

$$\Lambda_i = \int d^3\mathbf{r} \left|\psi_1^{\mathsf{VB}}(\mathbf{r})\right| \left|\psi_i^{\mathsf{CB}}(\mathbf{r})\right|, \tag{7.1}$$

which is bounded between 0 and 1. While all eigenstates are orthogonal, Λ_i is small when states have no spatial overlap. In the CR system, Λ_i is considerably smaller, especially for the lowest energy states, showing the spatial ratchet separating the lowest IB eigenstates from the VB ones. In both systems, Λ_i increases for higher energy CB states, which are increasingly delocalized. This effect is larger for the CR system, in which the lowest CB states have strongly reduced overlap with the lowest hole state.

These overlaps are indicative of a spatial ratchet, but not sufficient to conclude that the ratchet is functioning. The key feature of the RBSC threshold energies in Fig. 7.3 is that there is no IV absorption at the energy E_0, due to the spatial separation of electron and hole states. The actual absorption threshold E_{IV} is larger than E_0, which is essential to constructing the RB system. We now turn to calculating these thresholds quantitatively by constructing the absorption cross sections of a single dot and then the absorptances of the full dot array.

7.3 Optical absorption

Given our interest in blocking recombination within the QD, we focus on the IV and CI subgap transitions. Since the QD $\mathbf{k}\cdot\mathbf{p}$ model describes well the bound electron and hole states, we naturally use these to calculate the absorption for the IV transition. In contrast, the CI transition reaches the continuum, for which we introduce other methods. Beginning with the IV transition, in the electric dipole approximation, we can calculate the absorption cross section between initial and final bound states $|\psi_i\rangle$ and $|\psi_f\rangle$, respectively. The relevant dipole matrix element is [43, 67],

$$M_{if} = \frac{1}{A}\langle\psi_i|\hat{H}'|\psi_f\rangle, \tag{7.2}$$

where $\hat{H}'(\mathbf{k}) = \hat{H}\left(\mathbf{k} + \frac{e}{\hbar}\mathbf{A}\right) - \hat{H}(\mathbf{k})$ is the interaction Hamiltonian, $\hbar$ the reduced Planck's constant, e the electric charge and $\mathbf{A}$ the vector potential. Here, $\hat{H}$ is the QD $\mathbf{k}\cdot\mathbf{p}$ Hamiltonian. We only keep terms that are linear in $\mathbf{A}$.

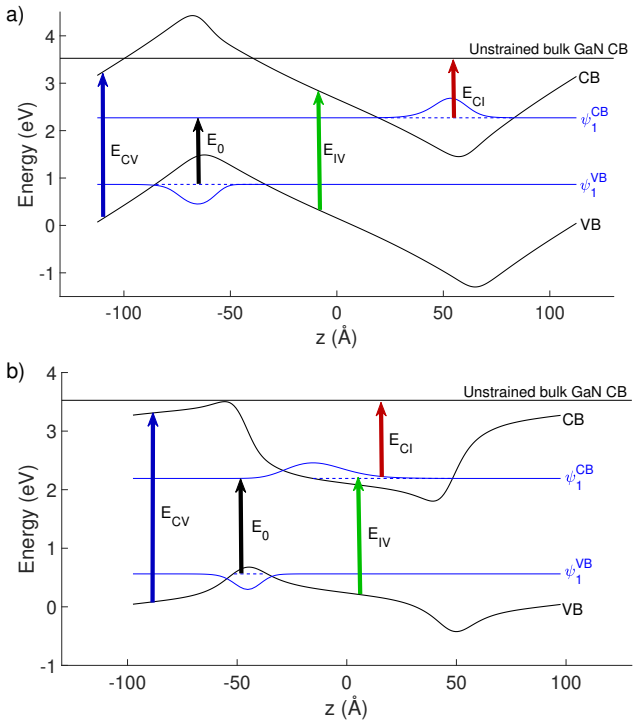

Figure 7.3: Electronic structures of InGaN QD superlattices in GaN along a cut through the axis of the cylinders. (a) clear ratchet (CR) system and (b) efficiency optimized (EO) system. Solid black lines are bulk band edges, which are modified by the piezoelectric potential and the diagonal portion of the deformation potential. Blue dashed lines are the lowest electron/hole state energies. Blue solid lines are z-axis projections of the squared wavefunctions. Note that the electron state of the CR is localized at the top of the dot and the hole at the bottom, increasing excitation lifetimes. The EO wavefunctions do not show spatial separation.

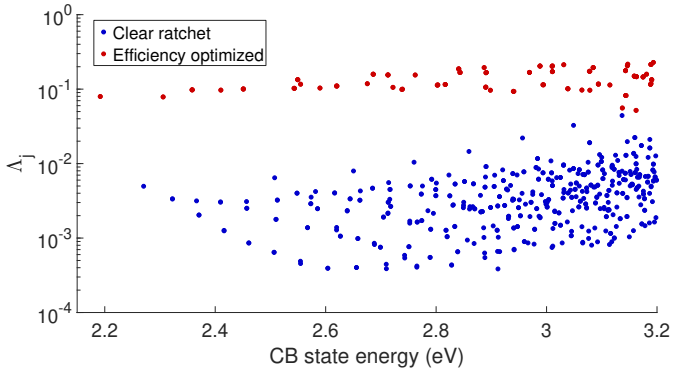

Figure 7.4: Spatial overlap between electronic states with energy E and the lowest hole state, as defined by Eq. 7.1 for the CR (blue) and EO (red) systems. The CR system spatially separates the states significantly more than the EO system.

From these matrix elements, the absorption cross section is [43]

$$\sigma_{if}(E) = \frac{2\pi\hbar}{\bar{n}\varepsilon_0 cE} |M_{if}|^2 (f_i - f_f)\, g(E_f - E_i - E), \tag{7.3}$$

where $\bar{n}$ is the average refractive index, ε_0 the vacuum permittivity, c the speed of light, f_i the Fermi-Dirac distribution at energy E_i, and

$$g(E) = \frac{1}{\Delta\sqrt{2\pi}} \exp\left(-\frac{E^2}{2\Delta^2}\right) \tag{7.4}$$

represents inhomogeneous broadening due to variation in QD sizes, which is controlled by the parameter Δ. The total absorption cross section for the bound-to-bound approach can then be obtained by summing over all possible transitions

$$\sigma_{\mathsf{BB}}(E) = \sum_{if} \sigma_{if}(E) \tag{7.5}$$

where i and f both run over all states in the VB, IB, and CB, although only occupied states contribute to i and unoccupied states contribute to f. In what follows, all cross sections are calculated using a temperature of 300 K. Based on photoluminescence measurements, the inhomogeneous broadening from self-assembled QDs ranges widely from 20-200 meV depending on temperature, growth, and the number of QD layers [20, 104, 105]. Calculations assume Δ=20 meV unless otherwise specified, and we show the sensitivity of the device efficiency and ratchet to Δ.

The CI process involves transitions to higher energy continuum states that are not necessarily well resolved in the $\mathbf{k}\cdot\mathbf{p}$ model, which is best at capturing the lower-energy states, which require fewer plane waves. In this case, it is preferable to approximate the continuum states using a model in which they are well described [85, 106, 107]. Reference [85] approximates the continuum states as CB plane waves with a parabolic dispersion. Since we work within the $\mathbf{k}\cdot\mathbf{p}$ framework, we can easily describe the continuum states as the bulk states of the $\mathbf{k}\cdot\mathbf{p}$ model of GaN. These states are modified plane waves that include mixing between the 8 bands of the $\mathbf{k}\cdot\mathbf{p}$ model and nonparabolicity of the dispersion, with all effects kept to the same order of approximation as for the bound states. The states from this approach should better capture the high energy states in the QD array than a simple effective mass approximation for the plane wave states. It is then a simple matter to calculate transition dipole matrix elements from the bound states to the bulk GaN states. As with the standard bound-to-free calculation, this approximation for the free states assumes that the continuum states are only lightly perturbed by the presence of the quantum dot, which becomes more accurate at higher energy.

Under this approximation, we take the dipole matrix elements from bound state $|\psi_i\rangle$ to free state $|\psi(\mathbf{k})\rangle$ to be

$$M_i(\mathbf{k}) = \frac{1}{A} \langle\psi_i|\hat{H}'|\psi(\mathbf{k})\rangle\,. \tag{7.6}$$

The continuum states $|\psi(\mathbf{k})\rangle$ are eigenstates of a bulk GaN Hamiltonian whose material parameters are independent of space; the states are normalized to the volume of the superlattice unit cell to give the proper matrix element [85].

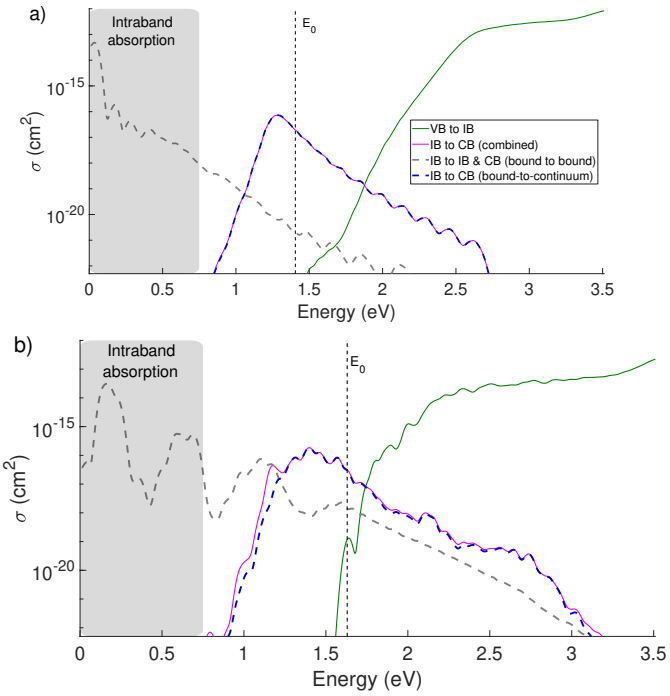

Figure 7.5: Absorption cross sections calculated using the bound-to-bound, bound-to-continuum, and combined approaches for (a) the CR system and (b) the EO system. In the CR system, the combined result for σ_{CI} overlaps with the bound-to-continuum result. Regions in grey represent intraband absorption that do not contribute to current generation. Vertical dashed lines show E_0 as defined in Fig. 7.3. Fermi level is fixed such that there are 4.9 electrons in each QD for the CR system and 6.1 for the EO.

The material parameters contained in the interaction Hamiltonian $\hat{H}'$ vary spatially according to the alloy profile of the QD superlattice. The cross section $\sigma_i(E, \mathbf{k})$ is calculated from $M_i(\mathbf{k})$ similarly to Eq. 7.3, and the associated total absorption cross section is [85]

$$\sigma_{\mathsf{BC}}(E) = \frac{V}{(2\pi)^3} \sum_i \int d^3\mathbf{k}\ \sigma_i(E, \mathbf{k}) \tag{7.7}$$

where V is the volume of the QD superlattice unit cell. The integral in Eq. 7.7 is calculated directly in the k-space used for the $\mathbf{k} \cdot \mathbf{p}$ calculations.

Figure 7.5 shows the 300 K cross sections obtained from both bound-to-bound and bound-to-continuum calculations. To ensure that both subgap optical transitions can occur, we consider the Fermi level to be fixed to give 6 electrons per QD if the temperature were 0 K. At 300 K, this Fermi level gives 4.9 electrons per QD in the CR and 6.1 electrons per QD in the EO and correspond to doping in the QD region of the device of approximately 3×10^{17} cm^{-3} for the CR and 10^{18} cm^{-3} for the EO system. The bound-to-bound calculations for IV and CI transitions consider all possible pairs of bound states corresponding to each transition. Since the IB and CB are both formed from the conduction band states of the original materials, the cross sections labeled as CI include absorptions that can also be thought of as being intraband transitions within the IB; that is, the final state is below the 3.53 eV GaN CB level, so they do not produce carriers that can be collected. This range of energies is

highlighted in Fig. 7.5 in grey and is not relevant for device operation.

For absorptions that end with an electron above the barrier-material CB edge, which can produce current, the bound-to-continuum calculation initially underestimates the cross section, as it underestimates the density of receiving states at the threshold. On the other hand, at higher energies, the bound-to-bound calculation considerably underestimates absorption for the CI transition as it is computationally costly to include sufficient plane waves to resolve the free states; in both cases, the larger value is more accurate as it has better sampling over the receiving states. We combine the reliable portions of both methods by adding σ_{BC} to the portion of σ_{BB} in which the final states have energy above the 3.53 eV GaN CB energy level, making the resulting carriers capable of being collected. With this restriction, only a portion of the transitions that produce the grey line also contribute to the CI cross section, and the combined line (magenta) is not simply the sum of the blue and grey lines. For the CR device, this combined method (magenta) is nearly on top of the bound-to-continuum method (blue), showing that the bound-to-continuum alone is sufficient for calculating the cross section. For the EO device, however, the bound-to-bound calculation causes a more significant change at low energy, reducing E_{CI} compared to where it would be with only the bound-to-continuum model.

Figure 7.5 makes clear that both systems display broadband subgap absorption, which has been a challenge in other ratchet band implementations. Note in particular that σ_{IV} for the EO system rises much more rapidly than with the CR. The spatial separation of states in the CR reduces the optical absorption, which is part of why the CR does not have the highest detailed balance efficiency, as is shown in Sec. 7.4. However, the CR should have reduced IV recombination compared to the EO.

We move from the individual dot to the absorptance of the full array by considering the effective absorption coefficient $\alpha(E)$ of the QD material for normally incident light, with each dot treated independently,

$$\alpha(E) = \rho\sigma(E), \tag{7.8}$$

where ρ is the volumetric density of dots. To achieve strong absorption, we consider the statistical light-trapping limit [102], in which the absorptance is

$$a(E) = \frac{4\bar{n}^2\alpha(E) N_{\mathsf{L}} L_3}{4\bar{n}^2\alpha(E) N_{\mathsf{L}} L_3 + 1}, \tag{7.9}$$

where N_{L} is the number of layers of dots and L_3 is the height of a supercell in the z-direction.

The key feature of a ratchet band is having the absorption threshold for the IV process be at energy larger than E_0, the fundamental gap of the system. We begin by considering a strongly absorbing system with 131000 layers of QDs. The system has a ratchet regardless of whether such a large number of dot layers is considered, as we show below. We observe the ratchet effect in Fig. 7.6(a), in which E_{IV} is 0.46 eV above E_0. Here, we define E_{IV} and E_{CI} as the lowest energy at which their respective absorptances equal 1%. We choose the number of plane waves to

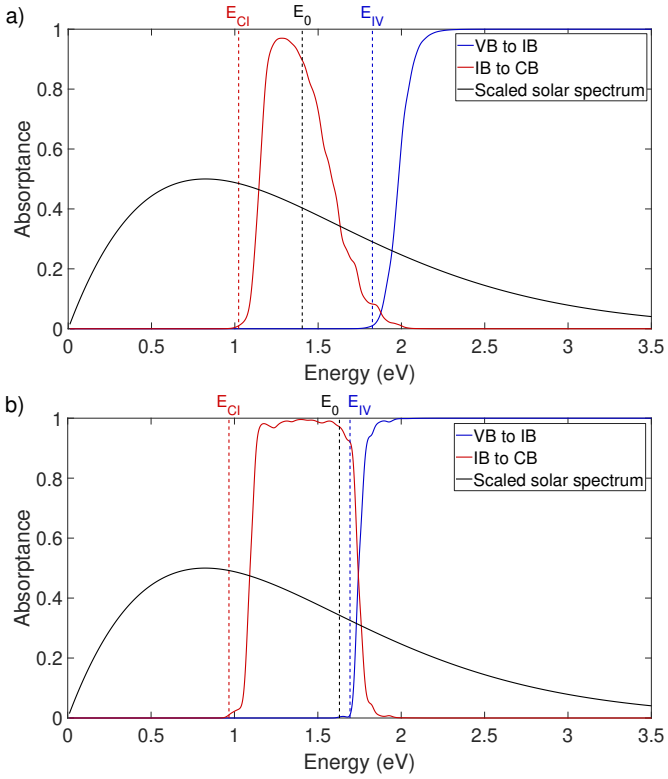

Figure 7.6: Absorptances for the two subgap transitions calculated from the $\mathbf{k}\cdot\mathbf{p}$ model with 131000 layers of QDs for (a) the CR system and (b) the EO system. Absorptances for the CI transition were calculated from the combined approach, detailed in the text. Black vertical dashed line is E_0, as shown in Fig. 7.3. Blue and red vertical dashed lines are the energy thresholds for the IV and CI transitions, respectively. Temperature is 300 K and the Fermi level is fixed such that there are 4.9 electrons in each QD for the CR system and 6.1 for the EO. While the CR shows a clear difference between E_{IV} and E_0, the optimized system also seems to present at most a small ratchet. While the offset between E_{IV} and E_0 in (a) is a true ratchet, the offset in panel (b) is due to electron filling of the CB states, as shown in Fig. 7.7. Black solid lines show scaled photon flux of a 6000 K black body, for reference.

converge E_{IV} within 3 meV and E_{CI} within 2 meV.

We must rule out this shift occurring due to the doping of the QDs, which fills the lowest IB states and blueshifts the IV absorption edge solely by Pauli exclusion. To rule out this mundane effect, Figure 7.7 shows how the absorption edge E_{IV} shifts with doping. We see that in the CR system, E_{IV} remains blue shifted from E_0 as the doping becomes small, ruling out Pauli exclusion effects. We conclude that we have a true RB system, driven by the spatial separation of the electron and hole states. By contrast, in the EO system, in the limit of an empty IB, E_{IV} reaches E_0 and in fact is slightly below E_0 due to the linewidth broadening Δ, showing that there is no spatial ratchet. Figure 7.7 was obtained with Δ=20 meV, which is on the optimistic side of the broadening range. Figure 7.8 shows that the CR system continues to have a ratchet all the way up to 200 meV, although it is more prominent for smaller Δ. Because E_{IV} is determined by the system's absorptance, as would be easy to measure experimentally, decreasing the number of QD layers blueshifts E_{IV}, increasing the ratchet energy $E_{\mathsf{IV}} - E_0$. The ratchet may, therefore, be more readily observable in systems with fewer layers.

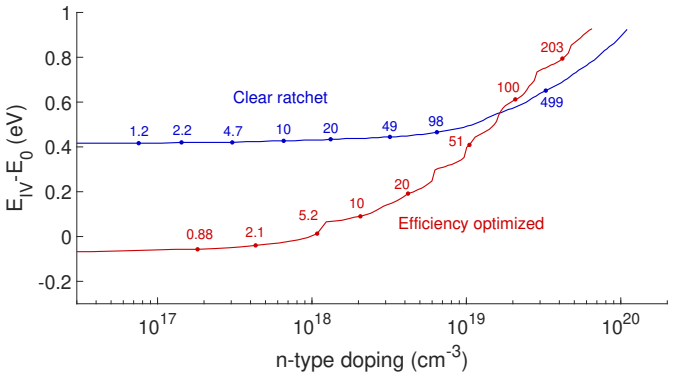

Figure 7.7: IV transition energy threshold E_{IV} relative to E_0 for the CR (blue) and EO (red) systems. Temperature is 300 K and the numbers along curves indicate the mean number of electrons per QD at selected dopings. For the CR system, E_{IV} is above E_0 as IB doping is reduced to zero. This blueshift of E_{IV} relative to E_0 is due to the spatially separated electron and hole states. In the case of the EO system (red), E_{IV} settles slightly below E_0, which indicates that there is no ratchet. E_{IV} goes below E_0 because of our definition of the absorption edge and linewidth broadening of the absorption.

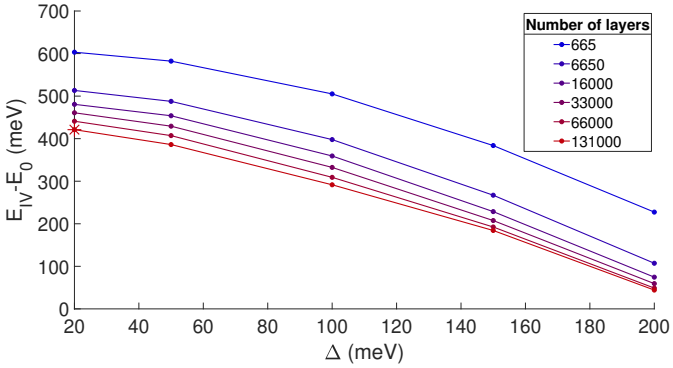

Figure 7.8: IV transition energy threshold E_{IV} relative to E_0 as function of linewidth broadening Δ for the CR system. Different curves are for varying number of layers of QDs. Star marker indicates the default parameters of Δ=20 meV and N_{L}=131000 used unless otherwise specified. EO system has no spatial ratchet, as determined from Fig. 7.7 and is therefore not shown. Temperature is 300 K and the Fermi level is such that there are 4.9 electrons electrons per QD.

7.4 Efficiencies

To calculate the limiting power conversion efficiency of the system, we use detailed balance calculations as previously described [26, 108]. The photon fluxes absorbed by or emitted from transitions between bands X and Y from the sun, solar cell and ambient are given by a modified Planck spectrum [27]

$$\phi_{XY}(\mu_{XY},T)=\frac{2\pi}{h^3c^2}\int_0^\infty \mathrm{d}E\,\frac{a_{XY}\left(E\right)E^2}{\mathrm{e}^{(E-\mu_{XY})/kT}-1} \tag{7.10}$$

where μ_{XY} is the quasi-Fermi level splitting between bands X and Y, k is the Boltzmann constant, T the temperature, and a_{XY} is the absorptance between bands X and Y. We consider photons with energy larger than the CV bandgap of 3.53 eV to be exclusively absorbed by the CV transition, before they reach the IB region of the device. For energies at which both IV and CI processes can absorb,

$$a_{XY}=a_{\mathsf{tot}}\frac{\alpha_{XY}}{\alpha_{\mathsf{CI}}+\alpha_{\mathsf{IV}}}, \tag{7.11}$$

where a_{tot} is calculated from Eq. 7.9 with $\alpha=\alpha_{\mathsf{CI}}+\alpha_{\mathsf{IV}}$. Under the usual detailed balance assumptions of only radiative recombination, infinite carrier mobility, that each absorbed photon produces one electron-hole pair, and no current from the QD bound states, the extracted current is

$$J=q\left(\dot{N}_{\mathsf{CV}}+\dot{N}_{\mathsf{CI}}\right), \tag{7.12}$$

where

$$\dot{N}_{\mathsf{CI}}=Cf_s\phi_{\mathsf{CI}}\left(0,T_{\mathsf{s}}\right)+\left(1-Cf_s\right)\phi_{\mathsf{CI}}\left(0,T_{\mathsf{a}}\right)-\phi_{\mathsf{CI}}\left(\mu_{\mathsf{CI}},T_{\mathsf{a}}\right)$$

$$\dot{N}_{\mathsf{CV}}=Cf_s\phi_{\mathsf{CV}}\left(0,T_{\mathsf{s}}\right)+\left(1-Cf_s\right)\phi_{\mathsf{CV}}\left(0,T_{\mathsf{a}}\right)-\phi_{\mathsf{CV}}\left(\mu_{\mathsf{CV}},T_{\mathsf{a}}\right)$$

where C is the concentration factor, $T_{\mathsf{a}}=300$ K is the ambient temperature, $T_{\mathsf{s}}=6000$ K is the solar temperature, and $f_s=2.16\times10^{-5}$ is the angular size of the sun. We take $C=1$ for a 1-sun concentration.

We consider two cases of absorptances, with the first being the ideal perfectly nonoverlapping absorptions [5], where

$$a_{\mathsf{CI}}\left(E\right)=\Pi_{E_{\mathsf{CI}}}^{E_{\mathsf{IV}}}\left(E\right) \tag{7.13}$$

$$a_{\mathsf{IV}}\left(E\right)=\Pi_{E_{\mathsf{IV}}}^{E_{\mathsf{CV}}}\left(E\right) \tag{7.14}$$

$$a_{\mathsf{CV}}\left(E\right)=\Pi_{E_{\mathsf{CV}}}^{\infty}\left(E\right). \tag{7.15}$$

Here, $\Pi_{E_{\mathsf{min}}}^{E_{\mathsf{max}}}\left(E\right)$ is 1 between E_{min} and E_{max} and 0 otherwise. Figure 7.9 shows the detailed balance efficiency with perfectly nonoverlapping absorptions for a GaN host material under a 1-sun 6000-K black-body spectrum, where we

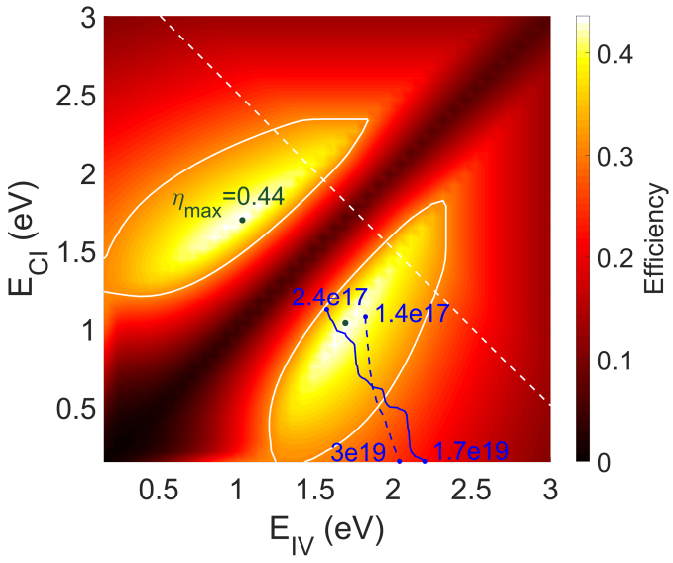

Figure 7.9: RBSC detailed balance efficiency for a GaN host material under a 1-sun black-body spectrum. White contour is the Shockley-Queisser limit. Overlaid on the color plot are two trajectories showing the attainable energy thresholds for the CR (dashed) and EO (solid) systems, as the doping of the QDs varies. Annotations at line extremities indicate n-type doping in cm^{-3} to achieve those energy thresholds. White dashed line represents the IBSC, where $E_{\mathsf{IV}} + E_{\mathsf{CI}} = E_{\mathsf{CV}}$. The optimal efficiency occurs where $E_{\mathrm{IV}} + E_{\mathrm{CI}} < E_{\mathrm{CV}}$, giving the device more current while reducing its voltage.

find a limiting efficiency of 44%, as previously reported [108]. The efficiency loss from the 48.5% global maximum is due to GaN having too large a bandgap, which could be reduced by considering an InGaN host material. The white dashed line represents IBSCs. In the lower left region, where $E_{\mathsf{IV}} + E_{\mathsf{CI}} < E_{\mathsf{CV}}$, the device gains more current at a cost of some voltage, leading to an efficiency increase compared to the IBSC.

A working QD IBSC solar cell depends on having partially filled IB states, which is controlled by doping or photofilling. The results from Fig. 7.9 are for perfect non-overlapping absorptions, but we have added the trajectories showing the energy thresholds of the CR (dashed) and EO (solid) systems as doping changes filling in the IB. In both cases, the trajectories reach the high efficiency-potential region. While this curve makes the CR appear to give highest efficiency at low doping, doping or photofilling to give carriers in the IB is required to make the CI absorption possible in reality. We now consider a more realistic model for the absorptances, including the effects of filling the IB.

For the second absorptance case, we use $a(E)$ obtained from the QD $\mathbf{k}\cdot\mathbf{p}$ model, shown in Fig. 7.6. To obtain reasonable results, we must find a way to limit $a(E)$ at low E. For materials whose absorptance continues to low energy, as can occur in the CI process due to excitation of thermally excited electrons in the QD states, Eq. 7.10 erroneously gives an infinite emitted photon flux if the voltage exceeds any energy where $a(E)$ is finite. For finite-thickness materials, general cell analysis allows treatment of infinitesimal absorptances in finite-thickness materials, where a population inversion exists, but little stimulated emission is produced in practice [109]. Recent work on absorption in hot carrier solar cells [110] and in the presence of Urbach tails [111] (evanescing band edges due to disorder) in detailed balance calculations resolved this low-energy absorption problem by treating Pauli exclusion.

They found a simple analytic expression to capture the important physics, making $a(E)$ dependent on the quasi-Fermi-level separation between bands. Those works considered only two-band systems, in which the quasi-Fermi levels of each band move away from midgap as the quasi-Fermi level splitting increases. Such behavior does not occur in both subgap transitions in an IB system, such as we consider. The photofilling or photodepletion of the IB depends crucially on the relative strength of the CI and IV processes and cannot be separately expressed in terms of only μ_{CI} or μ_{IV} [112]. The equivalent analysis for the IB case has not yet been completed. Instead of using either the more complicated general cell analysis or an inconsistent photofilling theory, we use the standard detailed balance method with $a(E)$ clipped to zero for all E below the point where $a(E)$=0.01. With this method, using the absorptions from the $\mathbf{k}\cdot\mathbf{p}$ model, we show in Fig. 7.10 that the CR system attains a 36% maximum efficiency, which is well above the Shockley-Queisser limit. We note that if we ignore the internal inconsistency of the method of [110] as applied to an IB system, we find that the CR system attains a maximum efficiency of 34%, which is similar to the 36% with our hard cutoffs.

We can achieve higher efficiency by optimizing over the QD geometry and indium fraction, as highlighted in the workflow shown in Fig. 7.2. A single cycle of the optimization process (electronic structure, absorption and detailed balance calculations) takes about 97 minutes. We performed an optimization with the Fermi level fixed such that 6 electrons occupy the IB states at 0 K. The Fermi level was fixed to reduce the optimization space and to keep the corresponding doping level at a realistic value. The barrier thicknesses in the z and in-plane directions were fixed at 100 Å. Given the fixed barrier, the superlattice unit cell size varies along with the dot radius and height. Fig. 7.10 shows that we can achieve an efficiency of 42%, close to the detailed balance limit for systems with a GaN host material. The optimization was converged within a 0.1% efficiency tolerance, using 5149 plane waves. Sensitivity analysis shows an absolute 1% efficiency loss with a 2 Å reduction or 1 Å increase in the radius, an 18 Å decrease or 15 Å increase in height, or a 3% reduction or 1% increase in indium fraction. The corresponding n-type doping level of the system is 1×10^{18} cm^{-3}.

Although the EO system has higher detailed balance efficiency than the CR, it does not have a ratchet. The detailed balance approach only depends on the absorption profiles of the system and has no dependence of the carrier lifetimes one would have in an actual device with nonradiative processes. The optimization produced a system with stronger subgap absorptions, aided by the spatial overlap of the electron and hole states.

The above efficiency analyses included 131000 dot layers to enable sufficient optical depth for the CI process in the CR system and an optimistic Δ=20 meV. Figure 7.11 shows how the efficiencies change with the number of QD layers and Δ. We find that the CR system is more sensitive to the number of layers, due to its weaker absorption cross sections, as seen in Fig. 7.5, and in particular the slow rise of $a_{\mathsf{IV}}(E)$; the voltage of the ratchet system is limited by E_{IV} but it needs many layers to attain significant absorption in the energy range near E_{IV}. In the case of the EO system, we can decrease the number of layers down to 33000-66000 and only lose 1-2% absolute in efficiency. It would also be possible to construct a system somewhere between the two, having a smaller ratchet, but also

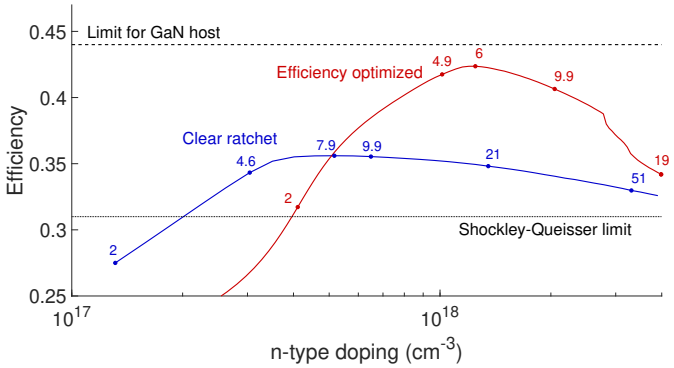

Figure 7.10: Detailed balance efficiency as function of doping for the CR (blue) and EO (red) systems with 131000 layers of dots. The rise from low doping is due to the increase of CI absorption up to the maximum, where the IV and CI processes are current matched. At larger doping, the CI process overproduces current compared to the IV process, decreasing the efficiency. Numbers along curves indicate the mean number of electrons per dot at 300 K. Dashed line is the detailed balance efficiency limit for a RBSC with a GaN host material and perfect nonoverlapping absorptions under a 1-sun 6000-K black-body spectrum. Dotted line is the Shockley-Queisser limit.

requiring fewer QD layers to achieve high efficiency. The effects of Δ are stronger on the EO system (which was only optimized for Δ=20 meV), with a significantly reduced efficiency at Δ=200 meV. The CR efficiency depends less strongly on Δ and even increases for larger Δ at some points.

Not explored in the single-particle calculations of this work are the effects of the electric field produced by the spatially separated charges after photoexcitation. This additional electric field should lead to a decrease in the overall potential that separates the states. We also do not consider the effects of either the built-in or external potentials. In this work, we consider an infinite lattice for the electronic structure calculation, making it difficult to explicitly include these potentials, as they would break the periodicity. However, in a standard p-i-n structure and 131000 layers of dots, the built-in potential would contribute only about 0.03 mV of potential change across each dot layer, which is small compared to the piezoelectric potentials seen in Fig. 7.3. In a p-n-i-p-n-type structure, with QDs in the intrinsic layer, as in [113], there is no built-in potential across the dots. The QD IB states are about 1 eV from the GaN CB band edge, a gap considerably larger than thermal energy.

7.5 Conclusions

We have presented an example of an experimentally accessible InGaN QD system that possesses a novel mechanism for a spatial ratchet. This device uses the piezoelectric potential to spatially separate the lowest electron and hole states to block recombination after the IV optical transition. Blocking this recombination pathway extends the lifetime of the carriers so that they can absorb a second photon for the CI transition.

We also present an optimized system that promises high efficiency if the device were radiatively limited, though actual QD devices generally have strong nonradiative recombination, which makes the ratchet system desirable. In practice, high efficiencies may be difficult to achieve in the InGaN QD system due needing a large number of

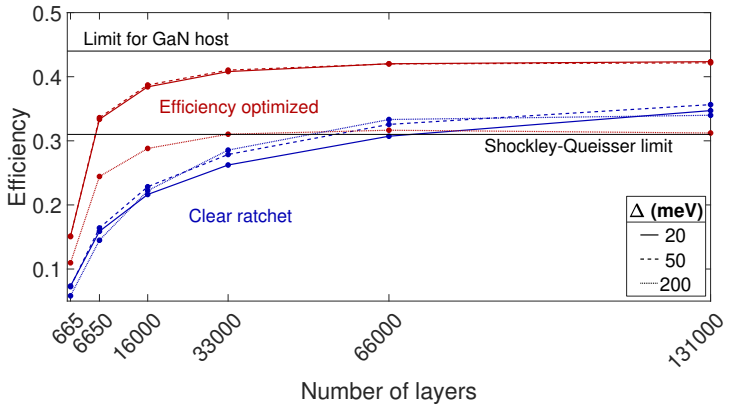

Figure 7.11: Detailed balance efficiency of the CR (blue) and EO (red) systems for varying number of QD layers and linewidth broadening Δ. Thin black lines are the Shockley-Queisser limit and the efficiency limit for a RBSC with a GaN host material and perfect nonoverlapping absorptions under a 1-sun 6000 K black-body spectrum. Temperature is 300 K and Fermi level is fixed such that the CR system contains 4.9 electrons per QD and 6.1 for the EO.

layers. However, stronger absorption could be achieved by increasing the doping and redesigning the QD geometry to match the solar spectrum as best as possible.

We have calculated the electronic structure of a 3D InGaN/GaN superlattice of cylindrical QDs and calculated the absorption cross sections for the subgap transitions. To calculate the absorption cross section for the CI transition, we have presented a method that approximates the higher energy states of the host material as bulk $\mathbf{k} \cdot \mathbf{p}$ states. Absorptances were constructed from the cross sections of systems with up to 131000 layers of QDs with a Lambertian back reflector. While strong absorption requires many layers, the ratchet still exists with only one layer and should be measurable.

Chapter 8

Conclusion

Wurtzite InGaN/GaN QDs are well studied systems and have already found success in applications such as LEDs [17] and single photon sources [18]. In the case of solar applications, wurtzite InGaN shows a lot of potential for applications within the field of IBSCs and RBSCs, promising efficiencies well above the Shockley-Queisser limit, as shown in Chapter 2. However, fabricated devices remain poorly efficient due to many issues such as recombination, trapping and weak absorption [1, 7]. To better understand some of these issues and help guide experimental work, this thesis makes methodological improvements to the efficient modeling of wurtzite QDs and applies that modeling to propose a novel way of using InGaN/GaN QD superlattices for RBSCs by taking advantage of the piezoelectric potential.

Chapter 6 contains most of the modeling advancements. In this Chapter, we use a Green's function method [42, 71] to calculate strain with nonuniform elastic constants, and we show that the nonuniform constants are important for both accurate strain fields and the resulting electronic structure in InGaN QD systems. Similarly, we adapt an existing method to calculate piezoelectric potentials from Maxwell's equations to include nonuniform dielectric constants [42] and show that this correction is also important for accurate results. We then present a method to include smoothly varying alloy profiles within the Fourier-space based strain, piezoelectric and $\mathbf{k} \cdot \mathbf{p}$ calculations. The smooth profile is obtained by convolving a sharp alloy profile with a Gaussian, and we find the electronic structure to be sensitive to the smoothing kernel, which is not surprising but indicates the need for accurate smoothing profiles in the modeling of QDs. In modeling the dots, we use a method that considers unique Fourier-space meshes for the strain and electronic structure calculations [59, 78], facilitating the study of isolated QDs in terms of both electronic structure and strain. Using this framework, we present a modified approach where we choose commensurate supercells for the strain and electronic structure calculations, which allows for more efficient coupling of strain into the Hamiltonian. Our commensurate cell method is especially useful for systems which one wants to optimize for some target application, leading to large numbers of simulations, such as was the case for the results of Chapter 7.

Chapter 7 applies the techniques developed in Chapter 6 to investigate the use of InGaN/GaN QD superlattices as ratchet band solar cells. We propose using electron and hole states, which are spatially separated by the piezoelectric potential, as a spatial ratchet to block recombination. To characterize device performance, we use Fermi's golden rule to calculate absorption from the superlattice's electronic structure using the dipole approximation [43, 66]. The $\mathbf{k}\cdot\mathbf{p}$ method is best at determining the lowest-energy bound states, and the higher-energy states are both computationally expensive to find and inherently less well resolved. Reference [85] calculates the bound-to-continuum absorption by approximating the continuum states as plane waves with a parabolic dispersion. In our work, we present an improved method where we approximate the continuum states as bulk $\mathbf{k}\cdot\mathbf{p}$ states of GaN, which better captures the high energy states of the continuum. From the calculated absorption, we show the clear presence of a spatial ratchet, which is generated by the piezoelectric potential, within InGaN/GaN QDs. By studying the optical properties of the dot, we show that this spatial ratchet has the potential of reducing recombination within the QDs. Our work therefore presents novel mechanism of producing a ratchet effect for RBSCs. The calculated absorptions are also coupled into a detailed balance model to predict power-conversion efficiencies. We present an example QD system which possesses a strong spatial ratchet which can achieve a maximum detailed-balance efficiency of 36% under a 1-sun 6000-K black-body spectrum. By optimizing dot geometry and composition, we can construct a different quantum dot array that can obtain 42% detailed balance efficiency, but that system does not have a ratchet. Unfortunately, these systems require a large number of QD layers to achieve such efficiencies, which is a well-known problem within the QD community. However, the number of layers could be reduced if one were to increase QD doping to increase the CI absorption and then tune the geometry of the dot to produce energy levels that match the solar spectrum.

For future prospects, experimental collaboration would be key in verifying the existence of the spatial ratchet within the InGaN QD system. Many groups have shown ability to grow InGaN/GaN QDs under various architectures such QDs in nanowires [17, 22, 96], QDs on the surface of nanowires [18] or as stratified 2D layers of QDs [7]. If QD devices are to be grown, then characterization will also play an important role in understanding the system's behavior while operating as a solar cell. SUNLAB at the University of Ottawa, which is a solar-energy focused group led by Karin Hinzer and with whom I have collaborated, has done a lot of work in both the modeling and characterization of solar cells, including QD-based systems [1, 114–116]. Test structures with only a single QD should show the ratchet effect, even though the device efficiency would be small.

A few different experiments could be performed to verify the existence of a spatial ratchet. A first experiment could be to verify the presence of the spatially separated electron and hole states, also known as the quantum confined Stark effect, by measuring the photoluminescence (PL) for various QD sizes and comparing to the PL of a bulk InGaN sample of similar indium fraction, similar as to what was done by Ref. [89]. One could also bias the system to cancel out the quantum confined Stark effect, leading to a stronger PL signal due to stronger wavefunction overlap. The bias necessary to achieve this could give insight on what is the potential difference across

the QD. Another experiment would be to confirm the two-photon process, which can be achieved by continuous light source for the CI process and a chopped light source for the IV, similar as to what was done for IBSCs in References [1, 10, 11]. As a last suggestion, perhaps the blocking of recombination due to the spatial ratchet could be verified by looking at electroluminescence spectrums while biasing the system. For the correct bias, the spatial ratchet could be removed, increasing wavefunction overlap, in which case we should observe an increase in radiative recombination.

There are, however, many challenges in making efficient QD-based solar cells. One such challenge is achieving strong absorption, as the absorption cross-section of QDs is generally small. In Chapter 7, I compensate the small absorption cross-section by considering many layers of QDs, which also presents experimental challenges to fabricate due to strain building up with each layer. The strain build-up problem is typically solved by introducing strain compensating layers after every few layers of QDs [117, 118], but the systems considered in Chapter 7 consist of up to 131000 layers of QDs, which is not feasible to fabricate even with strain compensating layers. However, as mentioned in the Chapter 7 introductory notes, we believe increased doping and optimization of the QD's size, and alloy should lead to similarly efficient devices with a more reasonable number of QD layers, closer as to what was found before the discovery of the units error. Another challenge is recombination and trapping inside the QDs. The InGaN/GaN QD RBSC we propose in Chapter 7 should reduce the recombination inside the QDs due to the spatial ratchet, but it does not solve trapping problem where carriers relax from the bulk CB of the host GaN and into the IB of the QD. This can be addressed by adding a shell with a large bandgap around the QDs to act as blocking layer to stop electrons from relaxing from the bulk CB and into the QD CB states [12]. Knowing that the trapping and absorption can be solved by the techniques mentioned above, verifying the spatial ratchet would truly make the InGaN/GaN QD system a promising candidate for surpassing the Shockley-Queisser limit.

In terms of accuracy, the $\mathbf{k}\cdot\mathbf{p}$ method is well known to be accurate for dots that are much larger than the crystal lattice unit cell, which is our case in this work. Our calculated strain, which is about 6-7% in the considered QDs, is also standard and remains sufficiently weak as to be well approximated by linear relations. However, nonlinearity in the strain to polarization relation has been shown to be important in the nitride-III systems [74, 75]. Excitonic effects would bring the electron and hole states closer in energy and shift the electronic gap of the QDs by 50-90 meV [39]. In theory, both the nonlinearity and excitonic effects would shift results quantitatively but could be corrected by changing the dot's size and composition. In reality, experimental devices have greater sources of error such as variations in the size and composition of the dots. The detailed balance model is rather optimistic as it assumes that there is only radiative recombination, but remains valid in the radiative limit, which can be found in high quality materials such as GaAs. We therefore think that our model is accurate in predicting a spatial ratchet, but that the parameters calculated for optimal efficiency might slightly change under these secondary effects.

To conclude, we have presented various methods that advance the modeling of wurtzite QDs and have used our model to study the use of InGaN/GaN QD superlattices for RBSCs. Further studies and optimizations are

necessary to see if absorption can be enhanced to truly make it a candidate for surpassing the Shockley-Queisser limit. However, we have shown that this RBSC architecture can produce can possess a spatial ratchet, which is generated by the piezoelectric field, to help in blocking recombination. The principle of this spatial ratchet could perhaps be applied to more highly absorbing systems in order to both reduce recombination and have sufficient absorption without too requiring too many layers of absorber material.

Appendix A

Bulk $\mathbf{k}\cdot\mathbf{p}$ parameters

Here, we write an 8-band Hamiltonian in the basis of $\hat{J}_z$ eigenfunctions, which are

$$\begin{aligned}
|u_1\rangle &= |iS,\uparrow\rangle & |u_5\rangle &= |-iS,\downarrow\rangle \\
|u_2\rangle &= |-\frac{X+iY}{\sqrt{2}},\uparrow\rangle & |u_6\rangle &= |\frac{X-iY}{\sqrt{2}},\downarrow\rangle \\
|u_3\rangle &= |\frac{X-iY}{\sqrt{2}},\uparrow\rangle & |u_7\rangle &= |-\frac{X+iY}{\sqrt{2}},\downarrow\rangle \\
|u_4\rangle &= |Z,\uparrow\rangle & |u_8\rangle &= |Z,\downarrow\rangle
\end{aligned} \tag{A.1}$$

where S, X, Y and Z are Γ-point Bloch functions with arrows indicating spin. The eigenvalues of the $\hat{J}_z$ eigenfunctions are

$$J_z = \left\{\frac{1}{2}, \quad \frac{3}{2}, \quad -\frac{1}{2}, \quad \frac{1}{2}, \quad -\frac{1}{2}, \quad -\frac{3}{2}, \quad \frac{1}{2}, \quad -\frac{1}{2}\right\},$$

The Hamiltonian in the J_z basis can be obtained from the Hamiltonian 3.78 by the transformation $H_{J_z} = UHU^{-1}$ such that

$$U = \begin{bmatrix} A & 0 \\ 0 & A^* \end{bmatrix} \tag{A.2}$$

and

$$A = \begin{bmatrix} -i & 0 & 0 & 0 \\ 0 & -\frac{1}{\sqrt{2}} & \frac{i}{\sqrt{2}} & 0 \\ 0 & \frac{1}{\sqrt{2}} & \frac{i}{\sqrt{2}} & 0 \\ 0 & 0 & 0 & 1 \end{bmatrix}. \tag{A.3}$$

Applying this transformation gives

$$H_{J_z} = \begin{bmatrix} g(\mathbf{k}) & \gamma \\ -\gamma^* & g^*(\mathbf{k}) \end{bmatrix}, \tag{A.4}$$

where

$$g(\mathbf{k}) = g_1(\mathbf{k}) + g_2(\mathbf{k}) + g_{\mathsf{cr}} + g_{\mathsf{so}} + g_{\mathsf{st}}$$

$$g_1(\mathbf{k}) = \begin{bmatrix} E'_{\mathsf{C}} & -\frac{P_2}{\sqrt{2}}k_+ & \frac{P_2}{\sqrt{2}}k_- & P_1 k_z \\ -\frac{P_2}{\sqrt{2}}k_- & E'_{\mathsf{V}} & 0 & 0 \\ \frac{P_2}{\sqrt{2}}k_+ & 0 & E'_{\mathsf{V}} & 0 \\ P_1 k_z & 0 & 0 & E'_{\mathsf{V}} \end{bmatrix} \tag{A.5}$$

$$g_2(\mathbf{k}) = \begin{bmatrix} A'_2\left(k_x^2+k_y^2\right)+A'_1k_z^2 & 0 & 0 & 0 \\ 0 & \left(\frac{L'_1+M_1}{2}\right)\left(k_x^2+k_y^2\right)+M_2k_z^2 & -\frac{1}{2}N'_1k_-^2 & -\frac{1}{\sqrt{2}}N'_2k_-k_z \\ 0 & -\frac{1}{2}N'_1k_+^2 & \left(\frac{L'_1+M_1}{2}\right)\left(k_x^2+k_y^2\right)+M_2k_z^2 & \frac{1}{\sqrt{2}}N'_2k_+k_z \\ 0 & -\frac{1}{\sqrt{2}}N'_2k_+k_z & \frac{1}{\sqrt{2}}N'_2k_-k_z & M_3\left(k_x^2+k_y^2\right)+L'_2k_z^2 \end{bmatrix}$$

$$g_{\mathsf{st}} = \begin{bmatrix} a_2(\epsilon_{xx}+\epsilon_{yy})+a_1\epsilon_{zz} & 0 & 0 & 0 \\ 0 & \frac{1}{2}(l_1+m_1)(\epsilon_{xx}+\epsilon_{yy})+m_2\epsilon_{zz} & -\frac{1}{2}(l_1-m_1)(\epsilon_{xx}-\epsilon_{yy})+in_1\epsilon_{xy} & -\frac{n_2(\epsilon_{xz}-i\epsilon_{yz})}{\sqrt{2}} \\ 0 & -\frac{1}{2}(l_1-m_1)(\epsilon_{xx}-\epsilon_{yy})-in_1\epsilon_{xy} & \frac{1}{2}(l_1+m_1)(\epsilon_{xx}+\epsilon_{yy})+m_2\epsilon_{zz} & \frac{n_2(\epsilon_{xz}+i\epsilon_{yz})}{\sqrt{2}} \\ 0 & -\frac{n_2(\epsilon_{xz}+i\epsilon_{yz})}{\sqrt{2}} & \frac{n_2(\epsilon_{xz}-i\epsilon_{yz})}{\sqrt{2}} & m_3(\epsilon_{xx}+\epsilon_{yy})+l_2\epsilon_{zz} \end{bmatrix} \tag{A.6}$$

$$g_{\mathsf{cr}} = \Delta_{\mathsf{cr}} \begin{bmatrix} 0 & 0 & 0 & 0 \\ 0 & 1 & 0 & 0 \\ 0 & 0 & 1 & 0 \\ 0 & 0 & 0 & 0 \end{bmatrix} \tag{A.7}$$

$$g_{\mathsf{so}} = \frac{\Delta_{\mathsf{so}}}{3} \begin{bmatrix} 0 & 0 & 0 & 0 \\ 0 & 1 & 0 & 0 \\ 0 & 0 & -1 & 0 \\ 0 & 0 & 0 & 0 \end{bmatrix} \tag{A.8}$$

$$\gamma = \frac{\sqrt{2}\Delta_{\mathsf{so}}}{3}\begin{bmatrix} 0 & 0 & 0 & 0 \\ 0 & 0 & 0 & 0 \\ 0 & 0 & 0 & 1 \\ 0 & 0 & -1 & 0 \end{bmatrix}. \tag{A.9}$$

Here, Δ_{cr} and Δ_{so} are the crystal field splitting and spin-orbit coupling, respectively. The band edges are $E'_{\mathsf{C}} = E_{\mathsf{V}} + E_{\mathsf{CV}} + \Delta_{\mathsf{cr}} + \frac{\Delta_{\mathsf{so}}}{3} + \varphi$ and $E'_{\mathsf{V}} = E_{\mathsf{V}} + \varphi$, where φ is any additional scalar potential such as the piezoelectric potential. g_{st} is the contribution to the Hamiltonian due to strain ϵ_{ij}. The $\mathbf{k}\cdot\mathbf{p}$ parameters A'_i are related to the Kane parameters P_i as

$$\begin{aligned} A'_1 &= \frac{\hbar^2}{2m_{\mathsf{e}}^{\parallel}} - \frac{P_1^2}{E_{\mathsf{CV}}} \\ A'_2 &= \frac{\hbar^2}{2m_{\mathsf{e}}^{\perp}} - \frac{P_2^2}{E_{\mathsf{CV}}} \end{aligned} \tag{A.10}$$

where

$$\begin{aligned} P_1^2 &= \frac{\hbar^2}{2m_0}\left(\frac{m_0}{m_{\mathsf{e}}^{\parallel}} - 1\right)\frac{3E_{\mathsf{CV}}\left(\Delta_{\mathsf{so}} + E_{\mathsf{CV}}\right) + \Delta_{\mathsf{cr}}\left(2\Delta_{\mathsf{so}} + 3E_{\mathsf{CV}}\right)}{2\Delta_{\mathsf{so}} + 3E_{\mathsf{CV}}} \\ P_2^2 &= \frac{\hbar^2}{2m_0}\left(\frac{m_0}{m_{\mathsf{e}}^{\perp}} - 1\right)\frac{E_{\mathsf{CV}}\left[3E_{\mathsf{CV}}\left(\Delta_{\mathsf{so}} + E_{\mathsf{CV}}\right)\right] + \Delta_{\mathsf{cr}}\left(2\Delta_{\mathsf{so}} + 3E_{\mathsf{CV}}\right)}{\Delta_{\mathsf{cr}}\Delta_{\mathsf{so}} + 3\Delta_{\mathsf{cr}}E_{\mathsf{CV}} + 2\Delta_{\mathsf{so}}E_{\mathsf{CV}} + 3E_{\mathsf{CV}}^2}. \end{aligned} \tag{A.11}$$

Here, $m_{\mathsf{e}}^{\parallel}$ and $m_{\mathsf{e}}^{\perp}$ are the electron effective masses along the z-axis and in the xy-plane, respectively. The Luttinger-like parameters L'_i, M_i and N'_i are related to the A_i parameters by

$$\begin{aligned} L'_1 &= \frac{\hbar^2}{2m_0}\left(A_2 + A_4 + A_5\right) + \frac{P_2^2}{E_{\mathsf{CV}}} \\ L'_2 &= \frac{\hbar^2}{2m_0}A_1 + \frac{P_1^2}{E_{\mathsf{CV}}} \\ M_1 &= \frac{\hbar^2}{2m_0}\left(A_2 + A_4 - A_5\right) \\ M_2 &= \frac{\hbar^2}{2m_0}\left(A_1 + A_3\right) \\ M_3 &= \frac{\hbar^2}{2m_0}A_2 \\ N'_1 &= \frac{\hbar^2}{2m_0}2A_5 + \frac{P_2^2}{E_{\mathsf{CV}}} \\ N'_2 &= \frac{\hbar^2}{2m_0}\sqrt{2}A_6 + \frac{P_1P_2}{E_{\mathsf{CV}}} \end{aligned} \tag{A.12}$$

Note there is an error in the relations for L'_1, L'_2 and N'_1 in Ref. [39], which we have corrected in agreement with Appendix B of Ref. [119]. The parameters A_i, P_i and E_{CV} used in our numerical study of InGaN systems are given in Table A.1.

Similarly to the $\mathbf{k}\cdot\mathbf{p}$ parameters L_i', M_i and N_i', the strain parameters are

$$\begin{aligned} l_1 &= D_2 + D_4 + D_5 \\ l_2 &= D_1 \\ m_1 &= D_2 + D_4 - D_5 \\ m_2 &= D_1 + D_3 \\ m_2 &= D_1 + D_3 \\ m_3 &= D_2 \\ n_1 &= 2D_5 \\ n_2 &= \sqrt{2}D_6 \end{aligned} \tag{A.13}$$

where the deformation potentials D_i are listed in Table A.1.

Table A.1: Material parameters used to model the InGaN system. Parameters were taken from Ref. [39]. Note that there is a sign error in e_{15} in [39]. This widespread sign error is discussed in greater detail in the erratum [75] to [78], which implements an 8-band $\mathbf{k}\cdot\mathbf{p}$ model using a plane wave basis to describe III-N QDs. This correct sign was also confirmed using ab initio DFT in [79].

Parameters	GaN	InN
a (Å)	3.189	3.545
c (Å)	5.185	5.703
C_{11} (GPa)	390	223
C_{12} (GPa)	145	115
C_{13} (GPa)	106	92
C_{33} (GPa)	398	224
C_{44} (GPa)	105	48
e_{15} ($\mathsf{C/m^2}$)	-0.326	-0.264
e_{31} ($\mathsf{C/m^2}$)	-0.527	-0.484
e_{33} ($\mathsf{C/m^2}$)	0.895	1.06
P_{sp} ($\mathsf{C/m^2}$)	-0.034	-0.042
ε_{r}	9.8	13.8
E_{CV} (eV)	3.51	0.78
E_{V} (eV)	0	0.5
Δ_{cr} (eV)	0.010	0.040
Δ_{so} (eV)	0.017	0.005
$m_{\parallel}/m_0$	0.20	0.07
$m_{\perp}/m_0$	0.20	0.07
A_1	-7.21	-8.21
A_2	-0.44	-0.68
A_3	6.68	7.57
A_4	-3.46	-5.23
A_5	-3.40	-5.11
A_6	-4.90	-5.96
a_1 (eV)	-4.9	-3.5
a_2 (eV)	-11.3	-3.5
D_1 (eV)	-3.7	-3.7
D_2 (eV)	4.5	4.5
D_3 (eV)	8.2	8.2
D_4 (eV)	-4.1	-4.1
D_5 (eV)	-4.0	-4.0
D_6 (eV)	-5.5	-5.5

Appendix B

Slowly varying envelope approximation

Here we show a crucial result for slowly varying envelopes, which is commonly used in constructing a QD $\mathbf{k}\cdot\mathbf{p}$ Hamiltonian. The proof shown here is adapted from [120].

In the slowly varying envelope approximation, we construct the wavefunctions using Bloch functions and envelope functions that are slowly varying with respect to the crystal lattice unit cell. We therefore encounter integrals of the form

$$I = \int_V \mathrm{d}^3\mathbf{r}\, \alpha(\mathbf{r})\, \beta(\mathbf{r}), \tag{B.1}$$

where $\alpha(\mathbf{r})$ is a function that is periodic with the crystal lattice (e.g. Bloch function) and $\beta(\mathbf{r})$ a function that is slowly varying inside a unit cell of the crystal lattice, e.g. an envelope function. In a periodic system such as a QD superlattice, V can be the volume of the superlattice unit cell. In a system which is not periodic, such as an impurity or a single QD in bulk, $V \to \infty$. Since the function $\alpha(\mathbf{r})$ has the same periodicity as the crystal lattice, it can then be expanded as

$$\alpha(\mathbf{r}) = \sum_{\mathbf{k}} \alpha_{\mathbf{k}} e^{i\mathbf{k}\cdot\mathbf{r}}, \tag{B.2}$$

where $\mathbf{k}$ are the reciprocal lattice wave vectors of the crystal lattice, and the expansion coefficients $\alpha_{\mathbf{k}}$ are given by

$$\alpha_{\mathbf{k}} = \frac{1}{V}\int_V \mathrm{d}^3\mathbf{r}\, \alpha(\mathbf{r})\, e^{-i\mathbf{k}\cdot\mathbf{r}}. \tag{B.3}$$

Inserting Eq. B.2 into Eq. B.1 gives

$$I = \sum_{\mathbf{k}} \alpha_{\mathbf{k}} \int_V \mathrm{d}^3\mathbf{r}\, \beta(\mathbf{r})\, e^{i\mathbf{k}\cdot\mathbf{r}} \tag{B.4}$$

We can decompose the volume integral into the sub-volumes of each crystal lattice unit cell of volume $V_{\mathbf{R}}$ by writing

$$I = \sum_{\mathbf{k}} \alpha_{\mathbf{k}} \sum_{\mathbf{R}} \int_{V_{\mathbf{R}}} \mathsf{d}^3\mathbf{r}\, e^{i\mathbf{k}\cdot(\mathbf{r}+\mathbf{R})} \beta\left(\mathbf{r}+\mathbf{R}\right), \tag{B.5}$$

where $\mathbf{R}$ are linear combinations of the crystal lattice basis vectors. Using the fact that $e^{i\mathbf{k}\cdot\mathbf{R}} = 1$ and that $\beta\left(\mathbf{r}\right)$ is slowly varying, allowing us to approximate $\beta\left(\mathbf{r}+\mathbf{R}\right) \approx \beta\left(\mathbf{R}\right)$, we obtain

$$I = \sum_{\mathbf{k}} \alpha_{\mathbf{k}} \sum_{\mathbf{R}} \beta\left(\mathbf{R}\right) \int_{V_{\mathbf{R}}} \mathsf{d}^3\mathbf{r}\, e^{i\mathbf{k}\cdot\mathbf{r}}. \tag{B.6}$$

The volume integral is only nonzero for $\mathbf{k} = 0$, which leads to

$$\begin{aligned} I &= \alpha_0 \sum_{\mathbf{R}} \beta\left(\mathbf{R}\right) V_{\mathbf{R}} \\ &\approx \alpha_0 \int_{V} \mathsf{d}^3\mathbf{r}\, \beta\left(\mathbf{r}\right). \end{aligned} \tag{B.7}$$

Using Eq. B.3 for $\mathbf{k} = 0$ gives

$$I = \frac{1}{V} \int_{V} \mathsf{d}^3\mathbf{r}\, \alpha\left(\mathbf{r}\right) \int_{V} \mathsf{d}^3\mathbf{r}\, \beta\left(\mathbf{r}\right). \tag{B.8}$$

We therefore find that, due to the large difference in the spatial variation of the functions, the integration over the functions can be separated into individual functions. This result is fundamental to the slowly varying envelope functions used in $\mathbf{k}\cdot\mathbf{p}$ applied to QD systems.

Appendix C

Envelope functions for quantum dot systems

When considering QD system, $\mathbf{k}\cdot\mathbf{p}$ is usually applied using a slowly varying envelope approximation. Within this approximation, the standard approach to constructing a QD $\mathbf{k}\cdot\mathbf{p}$ Hamiltonian is to consider a bulk Hamiltonian, give the material dependent parameters a spatial dependence, and substitute wave vectors with derivatives. In this section, we outline a justification of this approach, which is also used in Section 4.1. This derivation adapts a similar derivation done by [120] for the case of heterojunctions.

The key idea is to consider that the envelope functions are slowly varying with respect to the crystal lattice unit cell. Let us consider a QD superlattice, as drawn in Fig. 4.1 such that the superlattice unit cell has a volume V and the dot V_{d}. The derivation also holds for a single dot by taking $V \to \infty$. In the slowly varying envelope function approximation, we make two key assumptions. The first is that, for both dot and host regions, the wavefunction can be written as an expansion of Bloch functions $u_i(\mathbf{r})$ and envelope function $F_i(\mathbf{r})$, giving

$$\psi(\mathbf{r}) = \begin{cases} \sum_{i=1}^{N_{\mathsf{b}}} F_i^{\mathsf{d}}(\mathbf{r})\, u_i^{\mathsf{d}}(\mathbf{r}) & \mathbf{r} \in V_{\mathsf{d}} \\ \sum_{i=1}^{N_{\mathsf{b}}} F_i^{\mathsf{h}}(\mathbf{r})\, u_i^{\mathsf{h}}(\mathbf{r}) & \mathbf{r} \notin V_{\mathsf{d}}, \end{cases} \tag{C.1}$$

where N_{b} is the number of bands used in the $\mathbf{k}\cdot\mathbf{p}$ model. The superscript "d" indicates for dot, and "h" for host. The second assumption is that the Bloch functions from both regions are the identical

$$u_i(\mathbf{r}) \equiv u_i^{\mathsf{d}}(\mathbf{r}) = u_i^{\mathsf{h}}(\mathbf{r}), \tag{C.2}$$

in which case, we can write

$$\psi(\mathbf{r}) = \sum_{i=1}^{N_\mathsf{b}} F_i(\mathbf{r})\, u_i(\mathbf{r}), \tag{C.3}$$

such that

$$F_i(\mathbf{r}) = \begin{cases} F_i^\mathsf{d}(\mathbf{r}) & \mathbf{r} \in V_\mathsf{d} \\ F_i^\mathsf{h}(\mathbf{r}) & \mathbf{r} \notin V_\mathsf{d}. \end{cases} \tag{C.4}$$

Assuming a single electron in an infinite lattice of ions, the Hamiltonian for the QD system can be written

$$H = \frac{p^2}{2m} + V(\mathbf{r}), \tag{C.5}$$

where

$$\mathbf{p} = -i\hbar\boldsymbol{\nabla} \tag{C.6}$$

is the momentum operator and $V(\mathbf{r})$ the potential energy such that

$$V(\mathbf{r}) = \begin{cases} V^\mathsf{d}(\mathbf{r}) & \mathbf{r} \in V_\mathsf{d} \\ V^\mathsf{h}(\mathbf{r}) & \mathbf{r} \notin V_\mathsf{d}. \end{cases} \tag{C.7}$$

Note that given the presence of the dots, the potential energy is no longer periodic with the crystal lattice. Applying the Hamiltonian on $u_i(\mathbf{r})$ gives

$$H u_i(\mathbf{r}) = \varepsilon_i(r)\, u_i(\mathbf{r}), \tag{C.8}$$

where

$$\varepsilon_i(\mathbf{r}) = \begin{cases} \varepsilon_i^\mathsf{d}(\mathbf{r}) & \mathbf{r} \in V_\mathsf{d} \\ \varepsilon_i^\mathsf{h}(\mathbf{r}) & \mathbf{r} \notin V_\mathsf{d} \end{cases} \tag{C.9}$$

are the band edge energies associated to the $\mathbf{k} = 0$ Bloch states. Schrödinger's time independent equation for the system is

$$H\psi(\mathbf{r}) = E\psi(\mathbf{r}). \tag{C.10}$$

Inserting Eqs. C.3, C.5, C.6 and rewriting gives

$$\sum_{j=1}^{N_\mathsf{b}} \left\{ [\varepsilon_j(\mathbf{r}) - E]\, u_j(\mathbf{r})\, F_j(\mathbf{r}) - \frac{\hbar^2}{m}(\boldsymbol{\nabla} u_j)\cdot(\boldsymbol{\nabla} F_j) - \frac{\hbar^2}{2m} u_j(\mathbf{r})\, \nabla^2 F_j \right\} = 0. \tag{C.11}$$

Dropping the spatial dependence for brevity, we multiply from the left with $u_i^* F_i^*$ and integrate over the volume of

the superlattice unit cell V to obtain

$$\sum_{j=1}^{N_\mathrm{b}}\left[\int_V \mathrm{d}^3\mathbf{r}\,\left(\varepsilon_j - E\right)u_i^* u_j F_i^* F_j - \frac{\hbar^2}{m}\int_V \mathrm{d}^3\mathbf{r}\,\left(u_i^*\boldsymbol{\nabla}u_j\right)\cdot\left(F_i^*\boldsymbol{\nabla}F_j\right) - \frac{\hbar^2}{2m}\int_V \mathrm{d}^3\mathbf{r}\,u_i^* u_j F_i^*\nabla^2 F_j\right] = 0. \tag{C.12}$$

These are all integrals of products of functions that vary according to the crystal structure and functions that vary on the scale of the QD system. We can therefore use the following integral identity

$$\int_V \mathrm{d}^3\mathbf{r}\,\alpha\left(\mathbf{r}\right)\beta\left(\mathbf{r}\right) \approx \frac{1}{V}\int_V \mathrm{d}^3\mathbf{r}\,\alpha\left(\mathbf{r}\right)\int_V \mathrm{d}^3\mathbf{r}\,\beta\left(\mathbf{r}\right) \tag{C.13}$$

where $\alpha\left(\mathbf{r}\right)$ can be any function that varies on the scale of the crystal lattice and $\beta\left(\mathbf{r}\right)$ is any function that is slowly varying with respect to the crystal lattice unit cell (See Appendix B for proof). Applying this result to the integrals in Eq. C.12 gives

$$\begin{aligned}\sum_{j=1}^{N_\mathrm{b}}\Bigg[\frac{1}{V}\int_V \mathrm{d}^3\mathbf{r}\,u_i^* u_j \int_V \mathrm{d}^3\mathbf{r}\,\left(\varepsilon_j - E\right)F_i^* F_j - \frac{\hbar^2}{m}\left(\frac{1}{V}\int_V \mathrm{d}^3\mathbf{r}\,u_i^*\boldsymbol{\nabla}u_j\right)\cdot\left(\int_V \mathrm{d}^3\mathbf{r}\,F_i^*\boldsymbol{\nabla}F_j\right)\\ -\frac{\hbar^2}{2m}\frac{1}{V}\int_V \mathrm{d}^3\mathbf{r}\,u_i^* u_j \int_V \mathrm{d}^3\mathbf{r}\,F_i^*\nabla^2 F_j\Bigg] = 0\end{aligned} \tag{C.14}$$

By using the orthogonality of the Bloch functions and defining

$$\mathbf{p}_{ij} = \langle u_i|\mathbf{p}|u_j\rangle\,, \tag{C.15}$$

we obtain

$$\int_V \mathrm{d}^3\mathbf{r}\,F_i^*\sum_{j=1}^{N_\mathrm{b}}\left[\delta_{ij}\left(\varepsilon_j - E\right) - \frac{\hbar^2}{m}\mathbf{p}_{ij}\cdot\left(\boldsymbol{\nabla}\right) - \delta_{ij}\frac{\hbar^2}{2m}\nabla^2\right]F_j = 0 \tag{C.16}$$

Equation C.16 is essentially an eigenvalue problem for the envelope functions $F_i\left(\mathbf{r}\right)$ and is equivalent to

$$\langle F_i|\delta_{ij}\left(\varepsilon_i - E\right) - \frac{\hbar^2}{m}\mathbf{p}_{ij}\cdot\left(\boldsymbol{\nabla}\right) - \delta_{ij}\frac{\hbar^2}{2m}\nabla^2|F_j\rangle = 0, \tag{C.17}$$

which is again equivalent to

$$H_{ij}F_j\left(\mathbf{r}\right) = EF_j\left(\mathbf{r}\right), \tag{C.18}$$

where

$$H_{ij} = \delta_{ij}\varepsilon_j\left(\mathbf{r}\right) - \frac{\hbar^2}{m}\mathbf{p}_{ij}\cdot\left(\boldsymbol{\nabla}\right) - \delta_{ij}\frac{\hbar^2}{2m}\nabla^2 \tag{C.19}$$

The Hamiltonian H_{ij} is precisely equivalent to taking a $\mathbf{k}\cdot\mathbf{p}$ Hamiltonian and

1. giving the band edge energies a spatial dependence

2. doing the substitution $\mathbf{k} \to -i\boldsymbol{\nabla}$.

Note that in this calculation, we have assumed identical Bloch functions for the dot and host regions, leading to uniform matrix elements $\mathbf{p}_{ij}$. However, the Bloch functions do differ between materials. This proof could be generalized to have differing Bloch functions, giving $\mathbf{p}_{ij}$ a spatial dependence as well. Additional physics (e.g. spin-orbit coupling, strain, etc..) can also be introduced such that recipe remains the same, which is to give material-dependent parameters a spatial dependence, as is done for the band edge energies, and replace all wave vectors by operators [120]. This is the approach taken in Chapter 4 in order to construct a Hamiltonian for the QD superlattice.

When considering an abrupt junction, especially with small quantum dots, envelope functions can have variations that are too rapid for the application of Eq. C.13, but smoothed alloy distributions, as considered in Chapter 6, makes this approximation more valid. In the end, the envelope function $\mathbf{k} \cdot \mathbf{p}$ method is an approximation that needs to be checked against other theories or experiments, and it has been quite successful in practice for III/V semiconductor systems.

Appendix D

Fourier and Convolution Conventions

We define the Fourier forward and inverse transforms of a function $g(\mathbf{r})$ as

$$\mathscr{F}\{g(\mathbf{r})\}(\mathbf{q}) \equiv \tilde{g}(\mathbf{q}) = \frac{1}{(2\pi)^3} \int_{-\infty}^{\infty} \mathsf{d}^3\mathbf{r}\, g(\mathbf{r})\, \mathsf{e}^{-i\mathbf{q}\cdot\mathbf{r}}, \tag{D.1}$$

$$\mathscr{F}^{-1}\{\tilde{g}(\mathbf{q})\}(\mathbf{r}) = g(\mathbf{r}) = \int_{-\infty}^{\infty} \mathsf{d}^3\mathbf{q}\, \tilde{g}(\mathbf{q})\, \mathsf{e}^{i\mathbf{q}\cdot\mathbf{r}}. \tag{D.2}$$

A convolution is denoted by

$$(f * g)(\mathbf{r}) = \int_{-\infty}^{\infty} f(\mathbf{r}')\, g(\mathbf{r}-\mathbf{r}')\, \mathsf{d}\mathbf{r}'. \tag{D.3}$$

The convolution theorem states

$$\left(\tilde{f} * \tilde{g}\right)(\mathbf{q}) = \mathscr{F}\{f(\mathbf{r})\, g(\mathbf{r})\}(\mathbf{q}). \tag{D.4}$$

For a system that is periodic in real space with a unit cell Ω of volume V, we define

$$\tilde{g}(\mathbf{q}) = \frac{1}{(2\pi)^3} \int_{\Omega} \mathsf{d}^3\mathbf{r}\, g(\mathbf{r})\, \mathsf{e}^{-i\mathbf{q}\cdot\mathbf{r}} \tag{D.5}$$

$$g(\mathbf{r}) = \frac{(2\pi)^3}{V} \sum_{\mathbf{q}\in\Omega^{-1}} \tilde{g}(\mathbf{q})\, \mathsf{e}^{i\mathbf{q}\cdot\mathbf{r}} \tag{D.6}$$

where Ω^{-1} is the reciprocal space to the unit cell Ω. Defining the Fourier space convolution as

$$\left(\tilde{f} * \tilde{g}\right)(\mathbf{q}) = \sum_{\mathbf{q}'\in\Omega^{-1}} \tilde{f}(\mathbf{q}')\, \tilde{g}(\mathbf{q}-\mathbf{q}'), \tag{D.7}$$

the convolution theorem is

$$\left(\tilde{f} * \tilde{g}\right)(\mathbf{q}) = \frac{V}{(2\pi)^3} \mathscr{F}\left\{f(\mathbf{r})\, g(\mathbf{r})\right\}(\mathbf{q}). \tag{D.8}$$

Since we consider different superlattice unit cells for the electronic and strain properties, $\left(\tilde{f} * \tilde{g}\right)_{\mathsf{e}}$ indicates a convolution on the electronic space Ω_{e}^{-1} and $\left(\tilde{f} * \tilde{g}\right)_{\mathsf{s}}$ on the strain space Ω_{s}^{-1}.

The reciprocal space Ω^{-1} contains a discrete infinity of wave vectors on which to evaluate $\tilde{f}$ and $\tilde{g}$. The convolution in Eq. D.7 then sums over the infinite set of wave vectors, with $\tilde{f}$ and $\tilde{g}$ being functions that decay at large wave vectors. For the calculations in this manuscript, we choose a finite number of wave vectors. By choosing this mesh to contain wave vectors sufficiently large to capture the decay of $\tilde{f}$ and $\tilde{g}$, we can calculate the linear convolution in Eq. D.7 to good approximation by padding the $\tilde{f}$ and $\tilde{g}$ arrays with zeros and performing a circular convolution, defined below.

We denote the finite Fourier space mesh by $\mathbf{q}_{i_1 i_2 i_3}$ with $-m_j \leq i_j \leq m_j$ such that $N_j = 2m_j + 1$ is the dimension of the mesh in each direction. For convenience, we use the mapping $p_j = i_j + m_j + 1$, which runs from 1 to N_j. Evaluating a function $\tilde{f}$ on the mesh $\mathbf{q}_{p_1 p_2 p_3}$ gives the array $\tilde{f}_{p_1 p_2 p_3}$. The Fourier space array $\tilde{f}_{p_1 p_2 p_3}$ and its real-space counterpart $f_{v_1 v_2 v_3}$ are then related through the discrete Fourier transform and its inverse,

$$\tilde{f}_{p_1 p_2 p_3} = \mathscr{F}\{f\}_{p_1 p_2 p_3} = \frac{1}{(2\pi)^3} \sum_{v_1, v_2, v_3 = 1}^{N_1, N_2, N_3} f_{v_1 v_2 v_3} e^{-i2\pi(p_1 v_1/N_1 + p_2 v_2/N_2 + p_3 v_3/N_3)}, \tag{D.9}$$

$$f_{v_1 v_2 v_3} = \mathscr{F}^{-1}\left\{\tilde{f}\right\}_{v_1 v_2 v_3} = \frac{(2\pi)^3}{N} \sum_{p_1, p_2, p_3 = 1}^{N_1, N_2, N_3} \tilde{f}_{p_1 p_2 p_3} e^{i2\pi(p_1 v_1/N_1 + p_2 v_2/N_2 + p_3 v_3/N_3)}, \tag{D.10}$$

where $N = N_1 N_2 N_3$. The circular convolution is defined as

$$\left(\tilde{f} \bullet \tilde{g}\right)_{p_1 p_2 p_3} = \sum_{p_1', p_2', p_3' = 1}^{N_1, N_2, N_3} \tilde{f}_{p_1' p_2' p_3'} \tilde{g}_{(p_1 - p_1'), (p_2 - p_2'), (p_3 - p_3')}, \tag{D.11}$$

where $\tilde{g}_{(p_1+N_1),(p_2+N_2),(p_3+N_3)} = \tilde{g}_{p_1 p_2 p_3}$. The convolution theorem is then

$$\left(\tilde{f} \bullet \tilde{g}\right)_{p_1 p_2 p_3} = \frac{N}{(2\pi)^3} \mathscr{F}\{fg\}_{p_1 p_2 p_3}. \tag{D.12}$$

To perform a linear convolution, we pad the arrays with zeros, which increases the dimensions of the mesh to $N_j^{\mathsf{p}} = 2N_j - 1$ and yields the padded array $\tilde{f}^{\mathsf{p}}_{p_1 p_2 p_3}$ containing $N^{\mathsf{p}} = N_1^{\mathsf{p}} N_2^{\mathsf{p}} N_3^{\mathsf{p}}$ elements. The linear convolution of the original functions is contained in the circular convolution of the padded function

$$\left(\tilde{f} * \tilde{g}\right)_{p_1 p_2 p_3} = \left(\tilde{f}^{\mathsf{p}} \bullet \tilde{g}^{\mathsf{p}}\right)_{p_1 p_2 p_3} \tag{D.13}$$

This result is independent of the basis used to generate the mesh and is valid in the case of hexagonal meshes.

Appendix E

Strain for a single quantum dot

Here, we calculate the strain produced by a single wurtzite QD embedded in a bulk host material. This calculation, which is adapted from [42], assumes a continuous medium with uniform elastic constants. As discussed and motivated in Section 5.1, the general approach is to use Green's functions to construct the displacement field that is due to the QD. From the displacement field, we are able to obtain strain.

The Green's function for the displacement field $G_{ln}(\mathbf{r})$, for uniform elastic constants λ_{iklm}, is defined by

$$\lambda_{iklm}\frac{\partial^2 G_{ln}}{\partial x_k \partial x_m} = -\delta(\mathbf{r})\,\delta_{in}, \tag{E.1}$$

where the right hand side of Eq. E.1 represent a point force at position $\mathbf{r}$ in the n^{th} direction. The resulting displacement $\mathbf{u}(\mathbf{r})$ due to the QD can obtained by convolving the Green's function with the forces over the surface of the quantum dot

$$u_i(\mathbf{r}) = u_i^{(0)}(\mathbf{r}) + \int_{S_{\mathsf{d}}} G_{in}\left(\mathbf{r}-\mathbf{r}'\right)\,\mathrm{d}F_n\left(\mathbf{r}'\right), \tag{E.2}$$

where $u_i^{(0)}$ is the initial displacement before relaxation of the lattice, $\mathrm{d}F_n$ is the infinitesimal force in the n direction and S_{d} is the QD's surface. The initial displacement can be described using a characteristic function $\chi_{\mathsf{d}}(\mathbf{r})$, which is 1 inside the dot and 0 outside, by writing

$$u_i^{(0)}(\mathbf{r}) = u_i^{\mathsf{T}}\chi_{\mathsf{d}}(\mathbf{r}). \tag{E.3}$$

Force and stress are related through

$$\mathrm{d}F_n = \sigma_{nk}^{\mathsf{T}}\,\mathrm{d}S_k' \tag{E.4}$$

and the stress to strain by

$$\sigma_{nk}^{\mathsf{T}} = \lambda_{nkpr}\epsilon_{pr}^{\mathsf{T}}, \tag{E.5}$$

where

$$\epsilon_{pr}^{\mathsf{T}} = \begin{bmatrix} \varepsilon_{\mathsf{a}} & 0 & 0 \\ 0 & \varepsilon_{\mathsf{a}} & 0 \\ 0 & 0 & \varepsilon_{\mathsf{c}} \end{bmatrix} = \varepsilon_{\mathsf{a}}\delta_{pr} + \varepsilon_{\mathsf{ca}}\delta_{p3}\delta_{r3}. \tag{E.6}$$

Here, $\epsilon_{pr}^{\mathsf{T}}$ is the initial strain inside the dot with $\varepsilon_{\mathsf{c}} = (c_{\mathsf{h}} - c_{\mathsf{d}})/c_{\mathsf{d}}$, $\varepsilon_{\mathsf{a}} = (a_{\mathsf{h}} - a_{\mathsf{d}})/a_{\mathsf{d}}$ and $\varepsilon_{\mathsf{ca}} = \varepsilon_{\mathsf{c}} - \varepsilon_{\mathsf{a}}$, such that a is the in-plane lattice constant and c is the lattice constant along the c-axis. The subscript "d" and "h" indicate dot and host material. Using Eqs. E.3, E.4, E.5, we write Eq. E.2 as

$$u_i(\mathbf{r}) = u_i^{\mathsf{T}}\chi_{\mathsf{d}}(\mathbf{r}) + \int_{S_{\mathsf{d}}} G_{in}\left(\mathbf{r} - \mathbf{r}'\right)\lambda_{nkpr}\epsilon_{pr}^{\mathsf{T}}\,\mathsf{d}S_k' \tag{E.7}$$

Using Gauss's theorem for a rank n tensor,

$$\int_V \frac{\partial T_{i_1 i_2 \cdots i_q \cdots i_n}}{\partial x'_{i_q}}\mathsf{d}V' = \int_S T_{i_1 i_2 \cdots i_q \cdots i_n} n_{i_q}\mathsf{d}S' \tag{E.8}$$

and identifying $T_{ik} \equiv G_{in}\left(\mathbf{r} - \mathbf{r}'\right)\lambda_{nkpr}\epsilon_{pr}^{\mathsf{T}}$ and $\mathsf{d}S_k' \equiv n_k \mathsf{d}S'$, where n_k is the surface normal, we can replace the surface integral by a volume integral to obtain

$$u_i(\mathbf{r}) = u_i^{\mathsf{T}}(\mathbf{r})\,\chi_{\mathsf{d}}(\mathbf{r}) + \int_{V_{\mathsf{d}}} \frac{\partial G_{in}\left(\mathbf{r} - \mathbf{r}'\right)}{\partial x_k}\lambda_{nkpr}\epsilon_{pr}^{\mathsf{T}}\mathsf{d}V'. \tag{E.9}$$

Elements of the strain tensor $e_{ij}(\mathbf{r})$ can be obtained from the displacement field $\mathbf{u}(\mathbf{r})$ using the defining fundamental relation

$$\epsilon_{ij}(\mathbf{r}) = \frac{1}{2}\left(\frac{\partial u_i}{\partial x_j} + \frac{\partial u_j}{\partial x_i}\right). \tag{E.10}$$

Inserting Eq. E.9 into Eq. E.10 gives

$$\epsilon_{ij}(\mathbf{r}) = \epsilon_{ij}^{\mathsf{T}}\chi_{\mathsf{d}}(\mathbf{r}) + \frac{1}{2}\int_{V_{\mathsf{d}}}\left[\frac{\partial^2 G_{in}\left(\mathbf{r} - \mathbf{r}'\right)}{\partial x_j \partial x_k} + \frac{\partial^2 G_{jn}\left(\mathbf{r} - \mathbf{r}'\right)}{\partial x_i \partial x_k}\right]\lambda_{nkpr}\epsilon_{pr}^{\mathsf{T}}\mathsf{d}V' \tag{E.11}$$

The integration is over the volume of the quantum dot, but can be expanded to all of space by using a characteristic function $\chi_{\mathsf{d}}(\mathbf{r})$, which is 1 inside the dot and zero outside. Equation E.11 is then written

$$\epsilon_{ij}(\mathbf{r}) = \epsilon_{ij}^{\mathsf{T}}\chi_{\mathsf{d}}(\mathbf{r}) + \frac{1}{2}\int_{-\infty}^{\infty}\left[\frac{\partial^2 G_{in}\left(\mathbf{r} - \mathbf{r}'\right)}{\partial x_j \partial x_k} + \frac{\partial^2 G_{jn}\left(\mathbf{r} - \mathbf{r}'\right)}{\partial x_i \partial x_k}\right]\chi_{\mathsf{d}}(\mathbf{r}')\lambda_{nkpr}\epsilon_{pr}^{\mathsf{T}}\mathsf{d}V'. \tag{E.12}$$

We now take the Fourier transform to obtain

$$\tilde{\epsilon}_{ij}(\mathbf{q}) = \epsilon^{\mathsf{T}}_{ij}\tilde{\chi}_{\mathsf{d}}(\mathbf{q}) + \frac{1}{2}\mathcal{F}\left\{\left[\frac{\partial^2 G_{in}}{\partial x_j \partial x_k} + \frac{\partial^2 G_{jn}}{\partial x_i \partial x_k}\right] * \chi_{\mathsf{d}}\right\}\lambda_{nkpr}\epsilon^{\mathsf{T}}_{pr}. \tag{E.13}$$

Here, "$\mathcal{F}$" denotes a Fourier transform and "$*$" denotes a convolution, both being defined in Appendix D. By using the convolution theorem $\mathcal{F}\{f * g\} = (2\pi)^3 \mathcal{F}\{f\}\mathcal{F}\{g\}$, we get

$$\tilde{\epsilon}_{ij}(\mathbf{q}) = \epsilon^{\mathsf{T}}_{ij}\tilde{\chi}_{\mathsf{d}}(\mathbf{q}) + \frac{(2\pi)^3}{2}\mathcal{F}\left\{\frac{\partial^2 G_{in}}{\partial x_j \partial x_k} + \frac{\partial^2 G_{jn}}{\partial x_i \partial x_k}\right\}\tilde{\chi}_{\mathsf{d}}(\mathbf{q})\,\lambda_{nkpr}\epsilon^{\mathsf{T}}_{pr}. \tag{E.14}$$

We can get rid of the derivatives by using the property

$$\mathcal{F}\left\{\frac{\partial g}{\partial x_i}\right\} = iq_i\mathcal{F}\{g\} \tag{E.15}$$

to obtain

$$\tilde{\epsilon}_{ij}(\mathbf{q}) = \epsilon^{\mathsf{T}}_{ij}\tilde{\chi}_{\mathsf{d}}(\mathbf{q}) - \frac{(2\pi)^3}{2}\left[q_j\tilde{G}_{in}(\mathbf{q}) + q_i\tilde{G}_{jn}(\mathbf{q})\right]q_k\tilde{\chi}_{\mathsf{d}}(\mathbf{q})\,\lambda_{nkpr}\epsilon^{\mathsf{T}}_{pr}. \tag{E.16}$$

To get to a useful expression, we must now further inspect the Green's functions $\tilde{G}_{ij}(\mathbf{q})$ and the elastic constants λ_{nkpr}, starting with the latter. We start by calculating the object $\lambda_{nkpr}\epsilon^{\mathsf{T}}_{pr}$, which appears in Eq. E.16. In hexagonal crystals, there are five nonzero and independent elastic constants, which are $\lambda_{1111} = C_{11}$, $\lambda_{1122} = C_{12}$, $\lambda_{1133} = C_{13}$, $\lambda_{3333} = C_{33}$ and $\lambda_{2323} = C_{44}$ [42, 121]. We also have $\lambda_{1212} = \frac{1}{2}(C_{11} - C_{12})$, which is not independent. The elastic constant can then be written

$$\begin{aligned}\lambda_{nkpr} = {} & \alpha\delta_{nk}\delta_{pr} + \beta(\delta_{np}\delta_{kr} + \delta_{nr}\delta_{kp}) \\ & + \gamma\delta_{n3}\delta_{k3}\delta_{p3}\delta_{r3} + \kappa(\delta_{n3}\delta_{k3}\delta_{pr} + \delta_{nk}\delta_{p3}\delta_{r3}) \\ & + \rho(\delta_{nr}\delta_{k3}\delta_{p3} + \delta_{n3}\delta_{r3}\delta_{kp} + \delta_{np}\delta_{k3}\delta_{r3} + \delta_{n3}\delta_{p3}\delta_{kr})\end{aligned} \tag{E.17}$$

where

$$\begin{aligned}\alpha &= C_{12} \\ \beta &= \frac{1}{2}(C_{11} - C_{12}) \\ \gamma &= C_{33} - 2C_{13} - 4C_{44} + C_{11} \\ \kappa &= C_{13} - C_{12} \\ \rho &= C_{44} + \frac{C_{12} - C_{11}}{2}.\end{aligned} \tag{E.18}$$

Multiplying Eq. E.17 with $\epsilon^{\mathsf{T}}_{pr}$, which is defined by Eq. E.6, and summing over p and r gives

$$\lambda_{nkpr}\epsilon^{\mathsf{T}}_{pr} = R\delta_{nk} + S\delta_{n3}\delta_{k3}, \tag{E.19}$$

where

$$\begin{aligned} R &= (3\alpha + 2\beta + \kappa)\,\varepsilon_a + (\alpha + \kappa)\,\varepsilon_{ca} \\ S &= (\gamma + 3\kappa + 4\rho)\,\varepsilon_a + (2\beta + \gamma + \kappa + 4\rho)\,\varepsilon_{ca}. \end{aligned} \tag{E.20}$$

Inserting Eq. E.19 into Eq. E.16 gives

$$\begin{aligned} \tilde{\epsilon}_{ij}(\mathbf{q}) = (\varepsilon_a\delta_{ij} + \varepsilon_{ca}\delta_{i3}\delta_{j3})\,\tilde{\chi}_{\mathtt{d}}(\mathbf{q}) - \frac{(2\pi)^3}{2}\Big\{R\left[q_jq_k\tilde{G}_{ik}(\mathbf{q}) + q_iq_k\tilde{G}_{jk}(\mathbf{q})\right] \\ +S\left[q_iq_3\tilde{G}_{j3}(\mathbf{q}) + q_jq_3\tilde{G}_{i3}(\mathbf{q})\right]\Big\}\tilde{\chi}_{\mathtt{d}}(\mathbf{q}). \end{aligned} \tag{E.21}$$

Having dealt with the $\lambda_{nkpr}\epsilon^{\mathsf{T}}_{pr}$ factor, we now turn to the Green's functions and calculate the objects $\left(q\tilde{G}\right)_n \equiv q_l\tilde{G}_{nl}$ and $q_3\tilde{G}_{i3}$, both of which appear in Eq. E.21. We start by taking the Fourier transform of Eq. E.1 and use Eq. E.15 to get

$$\lambda_{iklm}q_kq_m\tilde{G}_{ln} = \frac{\delta_{in}}{(2\pi)^3}. \tag{E.22}$$

Inserting Eq. E.17 into Eq. E.22 gives

$$\begin{aligned} \left[\beta q^2 + \rho q_3^2\right]\tilde{G}_{in} + \left[\left(\rho q^2 + \gamma q_3^2\right)\delta_{i3} + (\kappa + \rho)\,q_iq_3\right]\tilde{G}_{3n} \\ +\left[(\alpha + \beta)\,q_i + (\kappa + \rho)\,\delta_{i3}q_3\right]\left(q\tilde{G}\right)_n = \frac{\delta_{in}}{(2\pi)^3}. \end{aligned} \tag{E.23}$$

We now need two equations to solve for $\tilde{G}_{3n}$ and $\left(q\tilde{G}\right)_n$. To obtain the first equation, we write Eq. E.23 for $i = 3$ and multiply by q_3 to obtain

$$Pq_3\tilde{G}_{3n} + I\left(q\tilde{G}\right)_n = \frac{\delta_{3n}q_3}{(2\pi)^3}, \tag{E.24}$$

where

$$\begin{aligned} P &\equiv C_{44}q^2 + (C_{33} - C_{13} - 2C_{44})\,q_3^2 \\ I &\equiv (C_{13} + C_{44})\,q_3^2. \end{aligned} \tag{E.25}$$

To obtain the second equation, we multiply Eq. E.23 by q_i and sum over i, giving

$$Qq_3\tilde{G}_{3n} + F\left(q\tilde{G}\right)_n = \frac{q_n}{(2\pi)^3}, \tag{E.26}$$

where

$$\begin{aligned} Q &\equiv \left(C_{33} - 2C_{13} - 4C_{44} + C_{11}\right) q_3^2 + \left(C_{13} + 2C_{44} - C_{11}\right) q^2 \\ F &\equiv \left(C_{13} + 2C_{44} - C_{11}\right) q_3^2 + C_{11} q^2. \end{aligned} \tag{E.27}$$

From Eqs. E.24 and E.26, we can solve for $q_3\tilde{G}_{3n}$ and $\left(q\tilde{G}\right)_n$ to obtain

$$q_3\tilde{G}_{3n} = \frac{q_n}{Q\left(2\pi\right)^3} - \frac{F}{Q}\left(q\tilde{G}\right)_n \tag{E.28}$$

$$\left(q\tilde{G}\right)_n = \frac{1}{\left(2\pi\right)^3}\frac{1}{FP - IQ}\left(Pq_n - Q\delta_{3n}q_3\right) \tag{E.29}$$

Having calculated $q_3\tilde{G}_{3n}$ and $\left(q\tilde{G}\right)_n$, we insert Eqs. E.28 and E.29 into Eq. E.21 to obtain our final result, which is

$$\tilde{\epsilon}_{ij}\left(\mathbf{q}\right) = \tilde{\chi}\left(\mathbf{q}\right)\left\{\varepsilon_{\mathsf{a}}\delta_{ij} + \varepsilon_{\mathsf{ca}}\delta_{i3}\delta_{j3} + \frac{RP\left(\mathbf{q}\right) - SI\left(\mathbf{q}\right)}{I\left(\mathbf{q}\right)Q\left(\mathbf{q}\right) - F\left(\mathbf{q}\right)P\left(\mathbf{q}\right)}q_iq_j + \frac{SF\left(\mathbf{q}\right) - RQ\left(\mathbf{q}\right)}{I\left(\mathbf{q}\right)Q\left(\mathbf{q}\right) - F\left(\mathbf{q}\right)P\left(\mathbf{q}\right)}q_3\frac{q_i\delta_{j3} + q_j\delta_{i3}}{2}\right\}. \tag{E.30}$$

Equation E.30 is therefore the Fourier transform of strain for a single wurtzite QD in bulk, having assumed uniform elastic constants λ_{iklm}. In this expression, the characteristic function contains the information about the dot geometry, while information on the crystal structure is contained in the brackets.

Note that from Eqs. E.22, E.28 and E.29, we can also obtain the Fourier-space Green's function for the displacement field:

$$\tilde{G}_{in} = \frac{1}{\left(2\pi\right)^3}\frac{1}{\beta q^2 + \rho q_3^2}\left\{\delta_{in} - \left[\left(\rho q^2 + \gamma q_3^2\right)\delta_{i3} + \left(\kappa + \rho\right)q_iq_3\right]\frac{F\delta_{3n} - I}{FP - IQ}q_n - \left[\left(\alpha + \beta\right)q_i + \left(\kappa + \rho\right)\delta_{i3}q_3\right]\frac{P - Q\delta_{3n}}{FP - IQ}q_n\right\}. \tag{E.31}$$

Appendix F

Characteristic functions

The characteristic function of a single dot is unity inside the dot and zero outside,

$$\chi_{\mathsf{d}}(\mathbf{r}) = \begin{cases} 1 & \mathbf{r} \in \Omega_{\mathsf{d}} \\ 0 & \text{otherwise} \end{cases} \tag{F.1}$$

where Ω_{d} is the space inside the dot. For a cylindrical dot centered on the origin with radius R and height h along the z-axis, the Fourier transform of χ_{d} is

$$\tilde{\chi}_{\mathsf{d}}(\mathbf{q}) = \frac{1}{(2\pi)^3} \frac{4\pi R}{q_3\sqrt{q_x^2+q_y^2}} \sin\left(\frac{h}{2}q_3\right) J_1\left(R\sqrt{q_x^2+q_y^2}\right). \tag{F.2}$$

The characteristic function of the electronic cell, the hexagonal prism shown in Fig. 6.2, is defined as

$$\chi_{\mathsf{e}}(\mathbf{r}) = \begin{cases} 1 & \mathbf{r} \in \Omega_{\mathsf{e}} \\ 0 & \text{otherwise} \end{cases} \tag{F.3}$$

and its Fourier transform is

$$\tilde{\chi}_{\mathsf{e}}(\mathbf{q}) = \frac{1}{(2\pi)^3} L_3 \mathrm{sinc}\left(q_3\frac{L_3}{2}\right) \frac{q_1\cos\left(\frac{L_{12}q_1}{2}\right) + q_2\cos\left(\frac{L_{12}q_1}{2}\right) - (q_1+q_2)\cos\left(L_{12}\frac{q_1+q_2}{2}\right)}{\sqrt{3}q_1q_2(q_1+q_2)}. \tag{F.4}$$

Appendix G

QD $\mathbf{k}\cdot\mathbf{p}$ Hamiltonian

For the QD superlattice system, the $\mathbf{k}\cdot\mathbf{p}$ Hamiltonian matrix elements of Eq. 6.26 in the symmetry adapted basis are given in terms of the parameters $f^{\mathsf{d}}_{\alpha'\alpha}$ and $f^{\mathsf{h}}_{\alpha'\alpha}$ that make up the bulk $\mathbf{k}\cdot\mathbf{p}$ Hamiltonian matrix elements $H_{\alpha'\alpha}$, presented in Sec. 6.3. We take the convention where superscript "(0)" indicates a bulk Hamiltonian matrix element containing no wave vector, "(i)" indicates a single wave vector k_i and "(i,j)" two wave vectors k_i and k_j. By defining $\phi = \frac{2\pi}{6}$ and

$$S^{ll'm_f}_{\alpha',\alpha} = e^{i\phi\left\{l\left[m_f - J_z(\alpha)\right] - l'\left[m_f - J_z(\alpha')\right]\right\}}, \tag{G.1}$$

$$S^{l'm_f}_{\alpha'} = e^{-il'\phi\left[m_f - J_z(\alpha')\right]}, \tag{G.2}$$

the QD Hamiltonian matrix elements are

$$\mathcal{H}^{(0)}_{m_f\alpha'\alpha}(\mathbf{q}',\mathbf{q}) = \frac{1}{6}\sum_{l'=0}^{5}\sum_{l=0}^{5} S^{ll'm_f}_{\alpha',\alpha}\, h_{\alpha'\alpha}\left(\overleftrightarrow{\mathbf{R}}_{l'}\mathbf{q}', \overleftrightarrow{\mathbf{R}}_{l}\mathbf{q}\right), \tag{G.3}$$

$$\mathcal{H}^{(i)}_{m_f\alpha'\alpha}(\mathbf{q}',\mathbf{q}) = \frac{1}{6}\sum_{l'=0}^{5}\sum_{l=0}^{5} S^{ll'm_f}_{\alpha',\alpha}\frac{\left(\overleftrightarrow{\mathbf{R}}_{l'}\mathbf{q}'\right)_i + \left(\overleftrightarrow{\mathbf{R}}_{l}\mathbf{q}\right)_i}{2} h_{\alpha'\alpha}\left(\overleftrightarrow{\mathbf{R}}_{l'}\mathbf{q}', \overleftrightarrow{\mathbf{R}}_{l}\mathbf{q}\right), \tag{G.4}$$

$$\mathcal{H}^{(i,j)}_{m_f\alpha'\alpha}(\mathbf{q}',\mathbf{q}) = \frac{1}{6}\sum_{l'=0}^{5}\sum_{l=0}^{5} S^{ll'm_f}_{\alpha',\alpha}\frac{\left(\overleftrightarrow{\mathbf{R}}_{l}\mathbf{q}\right)_j\left(\overleftrightarrow{\mathbf{R}}_{l'}\mathbf{q}'\right)_i + \left(\overleftrightarrow{\mathbf{R}}_{l}\mathbf{q}\right)_i\left(\overleftrightarrow{\mathbf{R}}_{l'}\mathbf{q}'\right)_j}{2} h_{\alpha'\alpha}\left(\overleftrightarrow{\mathbf{R}}_{l'}\mathbf{q}', \overleftrightarrow{\mathbf{R}}_{l}\mathbf{q}\right), \tag{G.5}$$

$$\mathcal{H}^{(0)}_{m_f\alpha'\alpha}(\mathbf{q}',\mathbf{q}_z) = \frac{1}{\sqrt{6}}\sum_{l'=0}^{5} S^{l'm_f}_{\alpha'}\, h_{\alpha'\alpha}\left(\overleftrightarrow{\mathbf{R}}_{l'}\mathbf{q}', \mathbf{q}_z\right), \tag{G.6}$$

$$\mathcal{H}^{(i)}_{m_f\alpha'\alpha}(\mathbf{q}',\mathbf{q}_z) = \frac{1}{\sqrt{6}}\sum_{l'=0}^{5} S^{l'm_f}_{\alpha'}\frac{\left(\overleftrightarrow{\mathbf{R}}_{l'}\mathbf{q}'\right)_i + (\mathbf{q}_z)_i}{2} h_{\alpha'\alpha}\left(\overleftrightarrow{\mathbf{R}}_{l'}\mathbf{q}', \mathbf{q}_z\right), \tag{G.7}$$

$$\mathcal{H}^{(i,j)}_{m_f\alpha'\alpha}\left(\mathbf{q}',\mathbf{q}_z\right)=\frac{1}{\sqrt{6}}\sum_{l'=0}^{5}S^{l'm_f}_{\alpha'}\frac{\left(\mathbf{q}_z\right)_j\left(\overleftrightarrow{\mathbf{R}}_{l'}\mathbf{q}'\right)_i+\left(\mathbf{q}_z\right)_i\left(\overleftrightarrow{\mathbf{R}}_{l'}\mathbf{q}'\right)_j}{2}h_{\alpha'\alpha}\left(\overleftrightarrow{\mathbf{R}}_{l'}\mathbf{q}',\mathbf{q}_z\right), \tag{G.8}$$

$$\mathcal{H}^{(0)}_{m_f\alpha'\alpha}\left(\mathbf{q}'_z,\mathbf{q}_z\right)=h_{\alpha'\alpha}\left(\mathbf{q}'_z,\mathbf{q}_z\right), \tag{G.9}$$

$$\mathcal{H}^{(i)}_{m_f\alpha'\alpha}\left(\mathbf{q}'_z,\mathbf{q}_z\right)=\frac{\left(\mathbf{q}'_z\right)_i+\left(\mathbf{q}_z\right)_i}{2}h_{\alpha'\alpha}\left(\mathbf{q}'_z,\mathbf{q}_z\right), \tag{G.10}$$

$$\mathcal{H}^{(i,j)}_{m_f\alpha'\alpha}\left(\mathbf{q}'_z,\mathbf{q}_z\right)=\frac{\left(\mathbf{q}_z\right)_j\left(\mathbf{q}'_z\right)_i+\left(\mathbf{q}_z\right)_i\left(\mathbf{q}'_z\right)_j}{2}h_{\alpha'\alpha}\left(\mathbf{q}'_z,\mathbf{q}_z\right), \tag{G.11}$$

where

$$h_{\alpha'\alpha}\left(\overleftrightarrow{\mathbf{R}}_{l'}\mathbf{q}',\overleftrightarrow{\mathbf{R}}_{l}\mathbf{q}\right)=f^{\mathsf{h}}_{\alpha'\alpha}\delta_{l,l'}\delta_{q,q'}+\frac{\left(2\pi\right)^3\left(f^{\mathsf{d}}_{\alpha'\alpha}-f^{\mathsf{h}}_{\alpha'\alpha}\right)}{V_{\mathsf{e}}}\tilde{\chi}_{\mathsf{d}}\left(\overleftrightarrow{\mathbf{R}}_{l'}\mathbf{q}'-\overleftrightarrow{\mathbf{R}}_{l}\mathbf{q}\right). \tag{G.12}$$

The contributions of the piezoelectric potential to the Hamiltonian are

$$\mathcal{H}^{\mathsf{pz}}_{m_f\alpha'\alpha}\left(\mathbf{q}',\mathbf{q}\right)=-\delta_{\alpha',\alpha}\frac{\left(2\pi\right)^3 e_{\mathsf{c}}}{6V_{\mathsf{e}}}\sum_{l'=0}^{5}\sum_{l=0}^{5}e^{i\phi\left(l-l'\right)\left[m_f-J_z(\alpha)\right]}\tilde{\varphi}^{\mathsf{a}}\left(\overleftrightarrow{\mathbf{R}}_{l'}\mathbf{q}'-\overleftrightarrow{\mathbf{R}}_{l}\mathbf{q}\right), \tag{G.13}$$

$$\mathcal{H}^{\mathsf{pz}}_{m_f\alpha'\alpha}\left(\mathbf{q}',\mathbf{q}_z\right)=-\delta_{\alpha',\alpha}\frac{\left(2\pi\right)^3 e_{\mathsf{c}}}{V_{\mathsf{e}}\sqrt{6}}\sum_{l'=0}^{5}e^{-il'\phi\left[m_f-J_z(\alpha')\right]}\tilde{\varphi}^{\mathsf{a}}\left(\overleftrightarrow{\mathbf{R}}_{l'}\mathbf{q}'-\mathbf{q}_z\right), \tag{G.14}$$

$$\mathcal{H}^{\mathsf{pz}}_{m_f\alpha'\alpha}\left(\mathbf{q}'_z,\mathbf{q}_z\right)=-\delta_{\alpha',\alpha}\frac{\left(2\pi\right)^3 e_{\mathsf{c}}}{V_{\mathsf{e}}}\tilde{\varphi}^{\mathsf{a}}\left(\mathbf{q}'_z-\mathbf{q}_z\right), \tag{G.15}$$

where $\tilde{\varphi}^{\mathsf{a}}$ is described in Secs. 6.2.3 and 6.3.2 and e_{c} is the electric charge.

Bibliography

[1] R. Cheriton, S. M. Sadaf, L. Robichaud, J. J. Krich, Z. Mi, and K. Hinzer, Communications Materials **1**, 63 (2020).

[2] J. Nelson, *The Physics of Solar Cells* (Imperial College Press, 2003).

[3] K. Yoshikawa, H. Kawasaki, W. Yoshida, T. Irie, K. Konishi, K. Nakano, T. Uto, D. Adachi, M. Kanematsu, H. Uzu, and K. Yamamoto, Nature Energy **2**, 17032 (2017).

[4] J. F. Geisz, R. M. France, K. L. Schulte, M. A. Steiner, A. G. Norman, H. L. Guthrey, M. R. Young, T. Song, and T. Moriarty, Nature Energy **5**, 326 (2020).

[5] A. Luque and A. Martí, Phys. Rev. Lett. **78**, 5014 (1997).

[6] N. E. Gorji, H. Movla, F. Sohrabi, A. Hosseinpour, M. Rezaei, and H. Babaei, Physica E: Low-dimensional Systems and Nanostructures **42**, 2353 (2010).

[7] L. Sang, M. Liao, Q. Liang, M. Takeguchi, B. Dierre, B. Shen, T. Sekiguchi, Y. Koide, and M. Sumiya, Advanced Materials **26**, 1414 (2014).

[8] J. Hwang, K. Lee, A. Teran, S. Forrest, J. D. Phillips, A. J. Martin, and J. Millunchick, Phys. Rev. Applied **1**, 051003 (2014).

[9] I. Ramiro, J. Villa, J. Hwang, A. J. Martin, J. Millunchick, J. Phillips, and A. Martí, Phys. Rev. Lett. **125**, 247703 (2020).

[10] A. Martí, E. Antolín, C. R. Stanley, C. D. Farmer, N. López, P. Díaz, E. Cánovas, P. G. Linares, and A. Luque, Phys. Rev. Lett. **97**, 247701 (2006).

[11] N. Ahsan, N. Miyashita, M. Monirul Islam, K. Man Yu, W. Walukiewicz, and Y. Okada, Applied Physics Letters **100**, 172111 (2012).

[12] G. Wei and S. R. Forrest, Nano Lett. **7**, 218 (2007).

[13] M. Yoshida, N. J. Ekins-Daukes, D. J. Farrell, and C. C. Phillips, Applied Physics Letters **100**, 263902 (2012).

[14] A. Vaquero-Stainer, M. Yoshida, N. P. Hylton, A. Pusch, O. Curtin, M. Frogley, T. Wilson, E. Clarke, K. Kennedy, N. J. Ekins-Daukes, O. Hess, and C. C. Phillips, Communications Physics **1**, 7 (2018).

[15] S. Asahi, H. Teranishi, K. Kusaki, T. Kaizu, and T. Kita, Nature Communications **8**, 14962 (2017).

[16] T. Sogabe, C.-Y. Hung, R. Tamaki, S. Tomić, K. Yamaguchi, N. Ekins-Daukes, and Y. Okada, Communications Physics **4**, 38 (2021).

[17] H. P. T. Nguyen, S. Zhang, K. Cui, X. Han, S. Fathololoumi, M. Couillard, G. A. Botton, and Z. Mi, Nano Lett. **11**, 1919 (2011).

[18] T. J. Puchtler, T. Wang, C. X. Ren, F. Tang, R. A. Oliver, R. A. Taylor, and T. Zhu, Nano Lett. **16**, 7779 (2016).

[19] M. G. Kibria, H. P. Nguyen, K. Cui, S. Zhao, D. Liu, H. Guo, M. L. Trudeau, S. Paradis, A. R. Hakima, and Z. Mi, ACS Nano **7**, 7886 (2013).

[20] B. Damilano, N. Grandjean, S. Dalmasso, and J. Massies, Applied Physics Letters **75**, 3751 (1999).

[21] C. Adelmann, J. Simon, G. Feuillet, N. T. Pelekanos, B. Daudin, and G. Fishman, Applied Physics Letters **76**, 1570 (2000).

[22] I.-K. Park, M.-K. Kwon, J.-O. Kim, S.-B. Seo, J.-Y. Kim, J.-H. Lim, S.-J. Park, and Y.-S. Kim, Applied Physics Letters **91**, 133105 (2007).

[23] M. T. Borgström, G. Immink, B. Ketelaars, R. Algra, and E. P. Bakkers, Nature Nanotechnology **2**, 541 (2007).

[24] J. A. Czaban, D. A. Thompson, and R. R. LaPierre, Nano Lett. **9**, 148 (2009).

[25] W. Shockley and H. J. Queisser, Journal of Applied Physics **32**, 510 (1961).

[26] E. Z. Zhang and J. J. Krich, Journal of Applied Physics **127**, 213105 (2020).

[27] P. Wurfel, Journal of Physics C: Solid State Physics **15**, 3967 (1982).

[28] A. Krishna and J. J. Krich, Journal of Optics **18**, 074010 (2016).

[29] L. C. Hirst and N. J. Ekins-Daukes, Progress in Photovoltaics: Research and Applications **19**, 286 (2011).

[30] M. Willatzen and L. C. Lew Yan Voon, *k p Method Electron. Prop. Semicond.* (Springer Berlin Heidelberg, Berlin, Heidelberg, 2009) pp. 1–445.

[31] P. Y. Yu and M. Cardona, *Fundamentals of Semiconductors: Physics and Materials Properties* (Springer Berlin Heidelberg, Berlin, Heidelberg, 2010).

[32] E. Kane, Journal of Physics and Chemistry of Solids **1**, 82 (1956).

[33] J. M. Luttinger and W. Kohn, Phys. Rev. **97**, 869 (1955).

[34] M. Cardona and F. H. Pollak, Phys. Rev. **142**, 530 (1966).

[35] S. L. Chuang and C. S. Chang, Phys. Rev. B **54**, 2491 (1996).

[36] Y. C. Yeo, T. C. Chong, and M. F. Li, Journal of Applied Physics **83**, 1429 (1998).

[37] F. Mireles and S. E. Ulloa, Phys. Rev. B **60**, 13659 (1999).

[38] V. A. Fonoberov and A. A. Balandin, Journal of Applied Physics **94**, 7178 (2003).

[39] M. Winkelnkemper, A. Schliwa, and D. Bimberg, Phys. Rev. B **74**, 155322 (2006).

[40] O. Marquardt, D. Mourad, S. Schulz, T. Hickel, G. Czycholl, and J. Neugebauer, Phys. Rev. B **78**, 235302 (2008).

[41] N. Vukmirović, D. Indjin, V. D. Jovanović, Z. Ikonić, and P. Harrison, Phys. Rev. B **72**, 075356 (2005).

[42] A. D. Andreev and E. P. O'Reilly, Phys. Rev. B **62**, 15851 (2000).

[43] N. Vukmirović, Z. Ikonić, D. Indjin, and P. Harrison, J. Phys. Condens. Matter **18**, 6249 (2006).

[44] N. Cavassilas, F. Aniel, K. Boujdaria, and G. Fishman, Phys. Rev. B **64**, 115207 (2001).

[45] S. Ben Radhia, K. Boujdaria, S. Ridene, H. Bouchriha, and G. Fishman, Journal of Applied Physics **94**, 5726 (2003).

[46] S. Richard, F. Aniel, and G. Fishman, Phys. Rev. B **70**, 235204 (2004).

[47] S. Tomić, Phys. Rev. B **73**, 125348 (2006).

[48] N. Ashcroft and N. Mermin, *Solid State Physics* (Cengage Learning, 2011).

[49] G. Koster, J. Dimmock, R. Wheeler, and H. Statz, *Properties of the Thirty-two Point Groups*, M.I.T. Press research monographs (M.I.T. Press, 1963).

[50] M. Tinkham, *Group theory and quantum mechanics*, International series in pure and applied physics (McGraw-Hill, New York, 1964).

[51] C. Galeriu, *k·p Theory of semiconductor nanostructures*, Ph.D. thesis, Worcester Polytechnic Institute (2005).

[52] M. S. Dresselhaus, G. Dresselhaus, and A. Jorio, *Group theory application to the physics of condensed matter* (Springer-Verlag, Berlin, 2007).

[53] J. J. Sakurai and J. Napolitano, *Modern Quantum Mechanics*, 2nd ed. (Cambridge University Press, 2017) pp. 262–302.

[54] P.-O. Löwdin, The Journal of Chemical Physics **19**, 1396 (1951).

[55] I. Vurgaftman, J. R. Meyer, and L. R. Ram-Mohan, Journal of Applied Physics **89**, 5815 (2001).

[56] I. Vurgaftman and J. R. Meyer, Journal of Applied Physics **94**, 3675 (2003).

[57] G. Bir and G. Pikus, *Symmetry and strain-induced effects in semiconductors*, Vol. 484 (Wiley New York, 1974).

[58] S. Tomić, A. G. Sunderland, and I. J. Bush, J. Mater. Chem. **16**, 1963 (2006).

[59] N. Vukmirović and S. Tomić, J. Appl. Phys. **103**, 103718 (2008).

[60] W. Trzeciakowski, Phys. Rev. B **38**, 4322 (1988).

[61] W. Trzeciakowski, Phys. Rev. B **38**, 12493 (1988).

[62] W. Trzeciakowski, Phys. Rev. B **42**, 3196 (1990).

[63] R. van Dalen and P. N. Stavrinou, Semiconductor Science and Technology **13**, 11 (1998).

[64] T. Ando and S. Mori, Surface Science **113**, 124 (1982).

[65] R. A. Morrow and K. R. Brownstein, Phys. Rev. B **30**, 678 (1984).

[66] N. Vukmirovic, Z. Ikonic, V. Jovanovic, D. Indjin, and P. Harrison, IEEE Journal of Quantum Electronics **41**, 1361 (2005).

[67] Z. Ikonic, V. Milanovic, and M. Tadic, Journal of Physics: Condensed Matter **7**, 7045 (1995).

[68] T. Saito and Y. Arakawa, Physica E **15**, 169 (2002).

[69] M. A. der Maur, A. Pecchia, G. Penazzi, F. Sacconi, and A. D. Carlo, Journal of Computational Electronics **12**, 553 (2013).

[70] S. Schulz, M. A. Caro, C. Coughlan, and E. P. O'Reilly, Phys. Rev. B **91**, 035439 (2015).

[71] A. D. Andreev, J. R. Downes, D. A. Faux, and E. P. O'Reilly, J. Appl. Phys. **86**, 297 (1999).

[72] J. D. Eshelby and R. E. Peierls, Proceedings of the Royal Society of London. Series A. Mathematical and Physical Sciences **241**, 376 (1957).

[73] J. D. Eshelby and R. E. Peierls, Proceedings of the Royal Society of London. Series A. Mathematical and Physical Sciences **252**, 561 (1959).

[74] V. Fiorentini, F. Bernardini, and O. Ambacher, Appl. Phys. Lett. **80**, 1204 (2002).

[75] S. Tomić and N. Vukmirović, Physical Review B **86**, 159902 (2012).

[76] D. P. Williams, A. D. Andreev, E. P. O'Reilly, and D. A. Faux, Phys. Rev. B **72**, 235318 (2005).

[77] L. Robichaud and J. J. Krich, Journal of Applied Physics **129**, 224301 (2021).

[78] S. Tomić and N. Vukmirović, Phys. Rev. B **79**, 245330 (2009).

[79] J. Pal, G. Tse, V. Haxha, M. A. Migliorato, and S. Tomić, Phys. Rev. B **84**, 085211 (2011).

[80] K. M. Gambaryan, T. Boeck, A. Trampert, and O. Marquardt, ACS Applied Electronic Materials **2**, 646 (2020).

[81] R. M. Martin, *Electronic Structure: Basic Theory and Practical Methods*, 2nd ed. (Cambridge University Press, 2020).

[82] D. R. Bowler and T. Miyazaki, Reports on Progress in Physics **75**, 036503 (2012).

[83] A. V. Rodina, A. Y. Alekseev, A. L. Efros, M. Rosen, and B. K. Meyer, Phys. Rev. B **65**, 125302 (2002).

[84] B. A. Foreman, Phys. Rev. B **75**, 235331 (2007).

[85] S. Tomić, T. Sogabe, and Y. Okada, Progress in Photovoltaics: Research and Applications **23**, 546 (2014).

[86] N. S. Beattie, P. See, G. Zoppi, P. M. Ushasree, M. Duchamp, I. Farrer, D. A. Ritchie, and S. Tomić, ACS Photonics **4**, 2745 (2017).

[87] O. Marquardt, S. Boeck, C. Freysoldt, T. Hickel, and J. Neugebauer, Computer Physics Communications **181**, 765 (2010).

[88] O. Marquardt, S. Boeck, C. Freysoldt, T. Hickel, S. Schulz, J. Neugebauer, and E. P. O'Reilly, Computational Materials Science **95**, 280 (2014).

[89] J. Renard, R. Songmuang, G. Tourbot, C. Bougerol, B. Daudin, and B. Gayral, Phys. Rev. B **80**, 121305 (2009).

[90] M. J. Holmes, K. Choi, S. Kako, M. Arita, and Y. Arakawa, Nano Lett. **14**, 982 (2014).

[91] A. V. Nenashev, A. A. Koshkarev, and A. V. Dvurechenskii, Journal of Applied Physics **123**, 105104 (2018).

[92] F. Bernardini, V. Fiorentini, and D. Vanderbilt, Phys. Rev. B **56**, R10024 (1997).

[93] A. Zoroddu, F. Bernardini, P. Ruggerone, and V. Fiorentini, Phys. Rev. B **64**, 045208 (2001).

[94] S. F. Chichibu, A. C. Abare, M. S. Minsky, S. Keller, S. B. Fleischer, J. E. Bowers, E. Hu, U. K. Mishra, L. A. Coldren, S. P. DenBaars, and T. Sota, Applied Physics Letters **73**, 2006 (1998).

[95] J. P. Ibbetson, P. T. Fini, K. D. Ness, S. P. DenBaars, J. S. Speck, and U. K. Mishra, Applied Physics Letters **77**, 250 (2000).

[96] H.-m. Kim, Y.-h. Cho, H. Lee, S. I. Kim, S. R. Ryu, D. Y. Kim, T. W. Kang, and K. S. Chung, Nano Letters **4**, 1059 (2004).

[97] M. J. Jocić and N. Vukmirović, Phys. Rev. B **102**, 085121 (2020).

[98] S. Tomić, P. Howe, N. M. Harrison, and T. S. Jones, Journal of Applied Physics **99**, 093522 (2006).

[99] M. A. Caro, S. Schulz, and E. P. O'Reilly, Phys. Rev. B **88**, 214103 (2013).

[100] L. Robichaud and J. J. Krich, IEEE Journal of Photovoltaics **12**, 474 (2022).

[101] A. Pusch and N. J. Ekins-Daukes, Phys. Rev. Applied **12**, 044055 (2019).

[102] E. Yablonovitch, J. Opt. Soc. Am. **72**, 899 (1982).

[103] L. Robichaud and J. J. Krich, in *2021 IEEE 48th Photovoltaic Specialists Conference (PVSC)* (2021) forthcoming.

[104] J. Ma, X. Ji, G. Wang, X. Wei, H. Lu, X. Yi, R. Duan, J. Wang, Y. Zeng, J. Li, F. Yang, C. Wang, and G. Zou, Applied Physics Letters **101**, 131101 (2012).

[105] G.-E. Weng, W.-R. Zhao, S.-Q. Chen, H. Akiyama, Z.-C. Li, J.-P. Liu, and B.-P. Zhang, Nanoscale Research Letters **10**, 31 (2015).

[106] M. Tadić and Z. Ikonić, Phys. Rev. B **52**, 8266 (1995).

[107] G. Todorović, V. Milanović, Z. Ikonić, and D. Indjin, Solid State Communications **110**, 103 (1999).

[108] L. Robichaud and J. J. Krich, in *2019 IEEE 46th Photovoltaic Specialists Conference (PVSC)* (2019) pp. 2138–2142.

[109] M. A. Green, *Third Generation Photovoltaics: Advanced Solar Energy Conversion* (Springer Berlin Heidelberg, Berlin, Heidelberg, 2003) pp. 35–58.

[110] D.-T. Nguyen, L. Lombez, F. Gibelli, S. Boyer-Richard, A. Le Corre, O. Durand, and J.-F. Guillemoles, Nature Energy **3**, 236 (2018).

[111] J. Wong, S. T. Omelchenko, and H. A. Atwater, ACS Energy Lett. **6**, 52 (2021).

[112] R. Strandberg and T. W. Reenaas, Journal of Applied Physics **105**, 124512 (2009).

[113] A. Marti, L. Cuadra, and A. Luque, IEEE Transactions on Electron Devices **49**, 1632 (2002).

[114] J. F. Wheeldon, A. Walker, C. E. Valdivia, S. Chow, O. Theriault, R. Beal, M. Yandt, D. Masson, B. Riel, D. McMeekin, N. Puetz, S. G. Wallace, V. Aimez, R. ArÃšs, T. J. Hall, S. Fafard, and K. Hinzer, AIP Conference Proceedings **1407**, 220 (2011).

[115] A. W. Walker, O. ThÃ©riault, and K. Hinzer, Progress in Photovoltaics: Research and Applications **23**, 793 (2015).

[116] R. Cheriton, *Design and characterization of InGaN/GaN dot-in-nanowire heterostructures for high efficiency solar cells*, Ph.D. thesis, University of Ottawa (2018).

[117] S. M. Hubbard, C. G. Bailey, C. D. Cress, S. Polly, J. Clark, D. V. Forbes, R. P. Raffaelle, S. G. Bailey, and D. M. Wilt, in *2008 33rd IEEE Photovoltaic Specialists Conference* (2008) pp. 1–6.

[118] R. Oshima, A. Takata, and Y. Okada, Applied Physics Letters **93**, 083111 (2008).

[119] E. Berkowicz, D. Gershoni, G. Bahir, E. Lakin, D. Shilo, E. Zolotoyabko, A. C. Abare, S. P. Denbaars, and L. A. Coldren, Phys. Rev. B **61**, 10994 (2000).

[120] G. Bastard, *Wave mechanics applied to semiconductor heterostructures* (John Wiley and Sons Inc, United States, 1990).

[121] E. Lifshitz, A. Kosevich, and L. Pitaevskii, *Theory of Elasticity (Third Edition)*, third edition ed. (Butterworth-Heinemann, Oxford, 1986) pp. 1–37.